Simulation-Based Design and Material Modeling for ENT Implants

CHUA CHIN HENG MATTHEW
B.Eng (Hons.), NUS

A THESIS SUBMITTED

FOR THE DEGREE OF DOCTOR OF PHILOSOPHY

DEPARTMENT OF MECHANICAL ENGINEERING

NATIONAL UNIVERSITY OF SINGAPORE

2015

DECLARATION

I hereby declare that the thesis is my original work and it has been written by me in its entirety. I have duly acknowledged all the sources of information which have been used in the thesis.

This thesis has also not been submitted for any degree in any university previously.

Chua Chin Heng Matthew
20 August 2015

Acknowledgement

This thesis work is not the effort of just one person, but the contribution of a multitude of wonderful people working miracles in my life that has led to the successful completion of this Ph.D. degree.

First and foremost, I would like to express my gratitude and appreciation to the supervision and guidance of ASSOC. PROF. Chui Chee Kong. He has been my mentor and academic supervisor since my undergraduate FYP days to my Ph.D. His encouraging words and patience never fails to spur me on to greater heights. My medical collaborators DR. David Lau and DR. Constance Teo for their great help in providing their medical expertise in this research work and for being such great team players. Special thanks to ASST. PROF. Thian Eng San for letting me use his BIOMAT laboratory ever so readily.

My funky colleagues, who are always ready to share their knowledge or lend a helping hand whenever the need arise. Kudos to DR. Wu Ji Chuan (what happens in Japan, stays in Japan), DR. Wen Rong, DR. Huang Wei Hsuan, MR. Choo Jun Quan, DR. Lee Chun Siong and DR. Sahan Herath. I would like to thank DR. Yvonne Ho for being my chauffeur from home to work and back and for offering solid relationship advice when needed. My deepest appreciation to MR. Chng Chin Boon, who went through thick and thin with me during my candidature from FYP to Ph.D. and for being a steadfast senior and a big brother to me!

My parent and loved ones, who have always been there for me and support me unconditionally and allowing me to focus fully on the completion of this doctorate degree. Thank you from the bottom of my heart!

SUMMARY

This thesis explores and proposes simulation-based design methodologies and material modeling of carbon nanocomposite for ENT implants for higher quality of healthcare. The simulations are based on patient-specific models in order to tailor the designs to patients' needs. Patient-specific design refers to the process of customizing the implant to fit into the anatomical dimension and needs of the individual, as well as to mimic as closely as possible the biomechanical properties of the original tissue.

Material attenuation plays a critical role in artificial airway scaffolds as high amplitude and frequency vibrations due to snoring or coughing of the patient may damage tracheal epithelium tissues and impede function. A predictive model for the attenuation of sound waves through carbon nanocomposite was proposed due to the latter's superior damping properties. This model takes into consideration the Rayleigh scattering function, absorption, resonance and interfacial friction of the nanofibers. The model shows close agreement with experimental results for low weight percentage of carbon nanotube and nanofiber fillers of up to 1%.

Current constitutive models for the mechanical properties of carbon nanocomposites may not predict well due to differences in conditions, fabrication techniques and inconsistencies in reagents properties used across industries and laboratories. A probabilistic algorithm was introduced that utilizes initial experimental data to model and predict the mechanical properties of the material. The mean results predicted were as accurate as within 3 standard deviations from the experimental mean. This technique can be integrated into the design analysis and evaluation of implant models for medical implants.

Surgical removal of 6 cm or more of the trachea in severe carcinoma requires a replacement graft due to anastomotic tension. The high failure rates of current grafts are attributed to mechanical properties mismatch and the slow epithelium formation on the inner lumen surface. The development of a patient-specific artificial trachea made of CNT-PDMS was carried out. The finite element simulation result indicated that the patient-specific design yield a more natural overall stress distribution *in-vivo*. The biocompatibility of the carbon nanocomposite and its ability to sustain tracheal epithelial cell proliferation and differentiation was verified *in-vitro*. *In-vivo* experiments carried out in porcine models showed no adverse side effects or breathing difficulties, with complete regeneration of the epithelium within two weeks. These promising preliminary results set the foundation for longer tracheal replacements and longer *in-vivo* studies in future.

The current standard range of sizes and shape of Tracheo-Esophageal Puncture (TEP) voice prostheses causes issues like transprosthetic and periprosthetic leakages due to poor valve closure and patient fistula misfit. A novel Computer Aided Design (CAD) methodology was proposed that utilizes patient's imaging data, simulations and rapid prototyping to develop the world's first patient-specific carbon nanocomposite voice prosthesis. The patient specificity in design allows for a snug fit of the prosthesis into the fistula while the CNT-PDMS material properties were similar to that of the surrounding tissues. This reduces the formation of granulation tissue and prosthesis failure due to mismatch. Experimental studies with the TEP voice prosthesis prototype indicate better leak resistance and lower forward air flow resistance, which translate to better quality of life for the patient. Lastly, the feasibility of the methodology was verified by *in-vivo* porcine models. Future studies include implantation of the device into human subjects.

Table of Contents

LIST OF ABBREVIATIONS

LIST OF FIGURES

LIST OF TABLES

Chapter 1

INTRODUCTION

1.1 Background

There is a lack of patient-specific simulation and design of medical prosthesis in the healthcare industry. Most implants have a specific range of sizes and are modular in shape which may lead to potential health issues or patient discomfort due to misfit. Instead of a “one size fits all” approach, this thesis investigates a “one method fits all” methodology by inculcating patient-specificity in the implant design and simulation process. Patient-specific design refers to tailoring and optimization of the implant design according to the specific anatomical dimension of the affected patient’s organ and its biomechanical properties. Similarity in primary properties like geometrical shape and sizes, followed by secondary characteristics like damping, scaffold degradation, flow resistance and mechanical properties are some of the target milestones in patient-specific ENT (Ear-Nose-Throat) implant designs.

Carbon nanotubes, when added to a base material, can significantly enhance the mechanical properties and biological properties of the composite, thus leading to numerous medical applications. One such superior property of the carbon nanocomposite would be its high damping behavior due to the large surface area to volume ratio of the nano-inclusions within. Deeper study and characterization of the material behavior is required in order to optimize the implant design for ENT patients. The ENT applications being investigated in this thesis are the Tracheo-Esophageal Puncture (TEP) voice

prosthesis and the tracheal prosthesis. The TEP voice prosthesis has traditionally relied on pure silicone material while no suitable material has yet to be found for the tracheal prosthesis despite a large number of materials being experimented on. Thus, the carbon nanocomposite and its ability to have its properties tailored closely to biological tissues may provide a better solution to these areas.

Carbon nanocomposites with their enhanced damping ability (Khan 2011) may be useful in medical implant applications with high damping requirements, for example in artificial tracheal grafts. This is important because high amplitude and frequency forced vibrations due to snoring or coughing may cause damage to the regenerated epithelial soft tissues around the tracheal scaffold (Cotado 2007), which may cause eventual implant failure as it affects the anchorage between the epithelium and sub-epithelium connective tissues (Boyd 2004, Paulsen 2002). A predictive attenuation model is proposed which provides a physical explanation to the attenuation of the nanocomposite materials at the nano-scale level, while allowing the coefficients to be computed using existing material properties and weight ratio of the nanofibers. The model takes into consideration the Rayleigh scattering function, absorption, resonance and interfacial friction of the inclusions to compute the apparent attenuation value. The theoretical results were then validated with ultrasonic and different frequencies of harmonic sound waves attenuation propagating through the material.

Modeling of the mechanical properties of carbon nanocomposites based on input variables like percentage weight of Carbon Nanotubes (CNT) inclusions is important for the Computer Aided Design (CAD) of medical implants and other structural scaffolds. Current constitutive models for the mechanical properties of nanocomposites may not

predict well due to differences in conditions, fabrication techniques and inconsistencies in reagents properties used across industries and laboratories. Furthermore, the mechanical properties of the designed products are not deterministic, but exist as a probabilistic range. A predictive model based on a modified probabilistic surface response algorithm is proposed to address this issue. Tensile testing of three groups of different CNT weight fractions of carbon nanocomposite samples displays scattered stress-strain curves, with the instantaneous stresses assumed to vary according to a normal distribution at a specific strain. From the probabilistic density function of the experimental data, a two factors Central Composite Design (CCD) experimental matrix based on strain and CNT weight fraction input with their corresponding stress distribution was established. Monte Carlo simulation was carried out on this design matrix to generate a predictive probabilistic polynomial equation. The equation and method were subsequently validated with more tensile experiments and Finite Element (FE) studies. The method was subsequently demonstrated in the design of an artificial tracheal implant. It provides an effective way in CAD processes to accurately model the mechanical properties implants of various shapes and compositions based on experimental data of samples.

Surgical removal of the trachea is the current gold standard for treating severe airway carcinoma and stenosis. However, resection of 6 cm or more of the diseased trachea length requires a replacement graft due to anastomotic tension. Numerous graft materials and designs have been investigated and no suitable long term solution has been found. The mechanical properties and size mismatch and the slow rate of epithelium formation on the inner lumen surface that leads to eventual failure of such grafts. A patient-specific artificial trachea made of CNT-PDMS nanocomposite material was

proposed and investigated. Computational simulations and finite element analysis were used to study the stress behavior of the designed implant in a patient-specific tracheal model, while *in-vitro* studies were performed to evaluate the biocompatibility and suitability of the graft material for sustaining tracheal epithelial cell proliferation and differentiation. *In-vivo* studies carried out in porcine models showed no adverse side effects or breathing difficulties, with complete regeneration of the epithelium in the prosthesis lumen within 2 weeks, a milestone improvement from the reported 4 to 8 weeks in literature.

Advanced computer technology can be used in patient-specific design of TEP voice prosthesis. The current voice prostheses have a standard range of sizes and shape that do not cater for all patients. This causes issues such as transprosthetic and periprosthetic leakages due to poor valve closure and misfit of the prosthesis in the patient's fistula, respectively. A Computer Aided Design (CAD) methodology was proposed, which utilizes patient's imaging data, simulation-based evaluations and rapid prototyping to develop the world's first patient-specific carbon nanocomposite voice prosthesis. The outer skin of the device is made from Carbon Nanotube – Polydimethysiloxane (CNT-PDMS) that is similar in material properties to the trachea-esophageal wall. Furthermore, individual prostheses are geometrically customized to fit the patient's fistula for better seal. CAD and simulation of the prostheses based on patient-specific anatomical dimensions from imaging data are performed and evaluated. Flow simulations and in-vitro experiments to study the air flow resistance of the novel magnetic ball bearing valve and a range of inner diameters showed lower flow resistance compared to other types of prostheses. Finally, successful preliminary *in-vivo*

experiments were carried out in porcine models to verify the feasibility of the patient-specific CAD methodology based on the subjects' imaging data. The advantages of this methodology eliminate the need for surgical correction to seal oversized fistulas and unnecessary multiple insertions due to incorrect sizing and misfit.

A block diagram is shown in Figure 1.1 that summarizes the content covered in each chapter of the thesis and the interactions between them. An extensive literature review is first performed to understand the limitations and gaps of current research, following which, a simulation-based design framework for medical device is proposed. From literature, new methods of material characterization and modeling like probabilistic predictive modeling and attenuation modeling will be proposed and studied. Lastly, application of the design framework and proposed models on the development of patient-specific carbon nanocomposite tracheal and voice prosthesis was carried out.

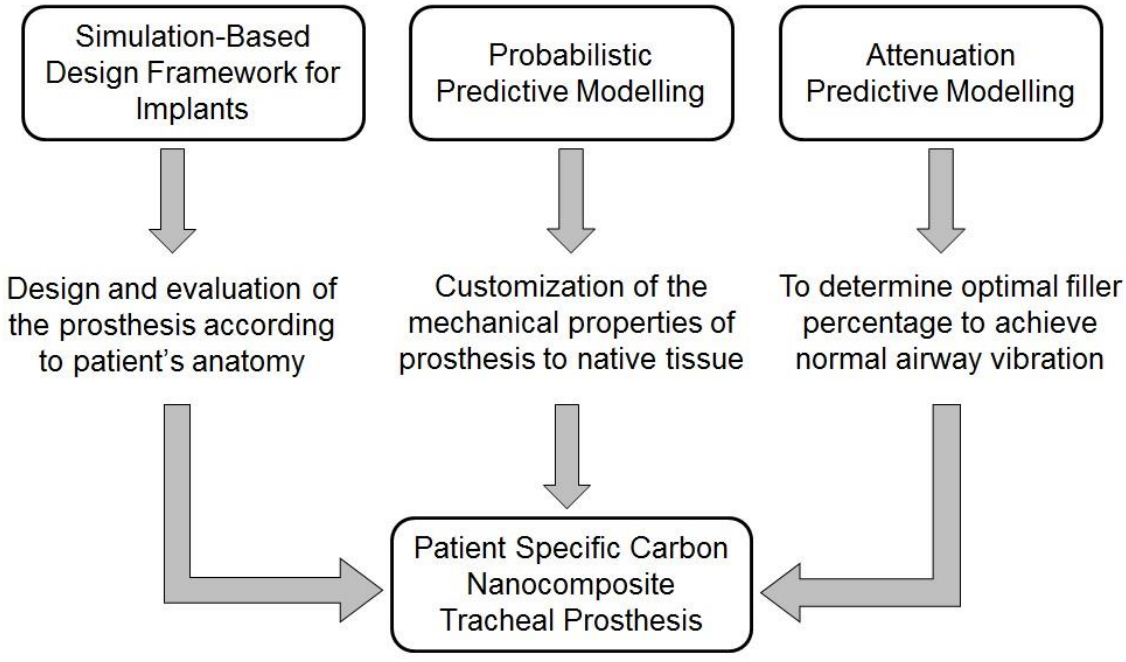

Figure 1.1: A block diagram of the chapter contents and the relationship between them.

1.2 Objective and Scope

An objective of this thesis is to improve the current ENT implants through the use of advance computer simulation processes and modeling of carbon nanocomposite materials. Current ENT prostheses are mostly modular, have widely different biomechanical properties and inert, which may lead to several problems including shorter product lifespan, limited performance and discomfort. This research aims to provide a greater understanding of the material behavior of carbon nanocomposites and the potential and advantages of using patient-specific designs in ENT implants.

The scope encompasses an extensive review of the existing literature on related topics, proposal of a new comprehensive design framework, new material modeling methods, and application of the proposed methods for the design, development and experimentation of new ENT devices. We have chosen CNT as the core material of the implants.

1.3 Thesis Organization

This thesis describes a simulation-based design framework for patient-specific implant design and fabrication. Chapter 1 gives an overview of the characterization of carbon nanocomposites and its use with patient-specific design methodology to develop ENT implants. Chapter 2 presents detailed anatomy study of ENT and covers extensive literature reviews on ENT implants, patient-specific designs, carbon nanocomposites, material modeling and tissue-material interactions. This is followed by the proposal of a simulation-based design framework for patient-specific implants. Chapter 3 introduces our work on carbon nanocomposite material characterization with the proposal of a new

attenuation predictive model, which is useful for the design of airway implants. Chapter 4 proposes a probabilistic approach to material behavior modeling for simulation-based design. Chapter 5 presents the development of a patient-specific tracheal prosthesis and the evaluation of the biological properties and performance of the CNT-PDMS nanocomposite *in-vitro* and *in-vivo*. In Chapter 6, the patient-specific CAD design methodology was applied to the design and development of the world's first patient-specific voice prosthesis. The thesis concludes in Chapter 7 with a discussion on its contributions and future work.

CHAPTER 2

LITERATURE REVIEW

This chapter presents detailed ENT anatomical information and related diseases to foster a good understanding and appreciation of the research work performed in this thesis. In addition, previous works on carbon nanocomposites, ENT-related prostheses and patient-specific methodologies were reviewed. Finally, an overview of the simulation-based design framework that is being proposed and investigated in this thesis is presented and discussed in relation to the current limitations of current works. Section 2.1 begins with an overview of ENT with detailed background on the human airway anatomy and their various functions. Section 2.2 describes existing ENT prostheses and implants specifically to trachea and voice while Sections 2.3 and 2.4 presents patient-specific design methodologies and current studies on carbon nanocomposites, respectively. Following which, Section 2.5 discusses mechanical modeling of material properties. Tissue-material interactions are then covered in Section 2.6. Section 2.7 presents and discusses the proposed simulation-based design framework for patient-specific implant. Lastly, the chapter concludes in Section 2.8.

2.1 Overview of Anatomy

Ear, Nose and Thoat (ENT) or commonly known as Otolaryngology, compasses the study of the conditions in the ear, nose (sinuses) and the throat of patients. Care was taken in this section to write it in a simplified yet detailed layman language to allow non-medically trained individuals and engineers to comprehend the various morbid anatomy

and histopathology of the human head and neck. These organs are inter-connected in the head at the back of the oral cavity and can be assessed through the mouth. As such, any one affected portion may lead to the impeded functioning of the other ENT-related organs. An example will be the blockage of sinuses due to flu virus has a good chance of affecting the hearing and speech quality in patients.

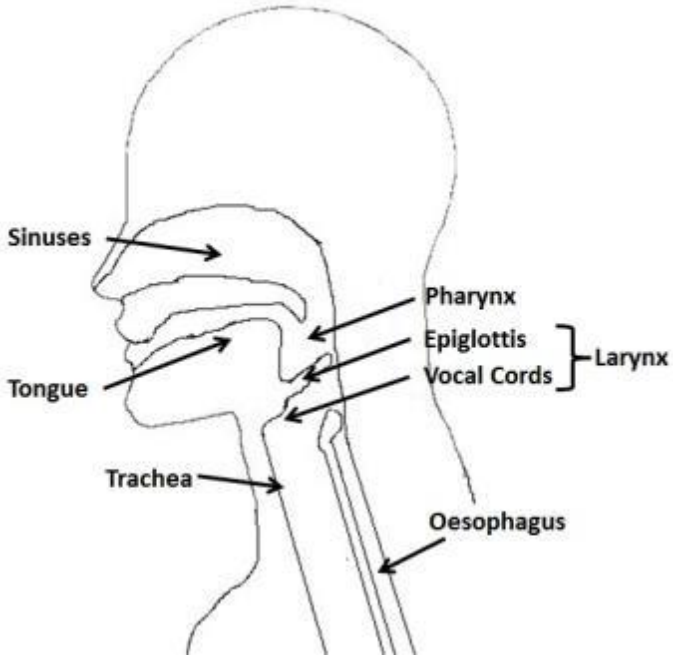

Figure 2.1: Anatomy of the Head and Neck

The mouth, larynx and trachea are important for daily activities like breathing and speech. Figure 2.1 depicts the cross sectional anatomy for a healthy individual's airway. Respiration begins when the diaphragm and the lungs expands, creating negative pressure in the airway that draws air into the sinuses through the nose and into the trachea. Air may also be inhaled via mouth, though the oral pathway lacks the fine hairs that are present in the nostrils that play a vital role to filter dust particles from the inhaled air. The air then passes through the pharynx to the larynx and then to the trachea and lungs. Food

and water enters the body normally via the mouth whereby enzymes secreted by the salivary glands and the chewing action helps to break down food. The food is then pushed further back into the pharynx by the sweeping motion of the tongue, where it is directed into the esophagus by the closing of the epiglottis over the entrance of the larynx.

2.1.1 The Pharynx

The pharynx is located at the back of the mouth, just above the larynx. Its function is to direct food down into the esophagus as well as to warm and moisten the inhaled air entering the lungs. The pharynx also consists of a soft palate that lies above the oral cavity, which is involved in vocalization. The stretching and relaxation of the soft palate muscles results in different volumetric shapes of the oral cavity that produces a variety of vowels for phonation. The vowel sounds combined with positioning of the teeth and tongue creates consonants that make audible speech.

Minor ailments of the pharynx like pharyngitis or polyps are due to the inflammation or formation of benign tumours on the pharynx. Though they may cause pain and discomfort during swallowing, they are usually non-fatal and can be easily treated through medication like steroids. Pharyngeal carcinoma usually overlaps with laryngeal carcinoma due the close proximity of both tissues. These cancers, usually the result of squamous cell carcinoma, if left untreated, may prove fatal to the patient. Treatment of pharyngeal-laryngeal carcinoma includes radiotherapy, chemotherapy or laryngectomy (the surgical removal of the pharynx and larynx) depending on the severity of the cancer. Patients who have undergone laryngectomy are called laryngectomees; and they require speech therapy or voice prostheses in order to enable them to speak again.

2.1.2 The Larynx

The larynx, commonly known as the voice box, is located just below the pharynx and at the entrance of the trachea. Its main functions involve the manipulation of pitch and volume during phonation and also the prevention of food aspiration from occurring in the trachea. The three main anatomical structures of the larynx include the thyroid cartilage, the epiglottis and the vocal chords.

The thyroid cartilage forms the visible landmark on the frontal neck of most males, also known as the Adam's apple. The thyroid cartilage is bigger and more visible in males than in females. The second structure, the epiglottis is a large spoon shaped piece of elastic cartilage that is located next to the entrances of the trachea and the esophagus. During swallowing, the pharyngeal muscles relax and widen to receive food. This causes the epiglottis to move down and cover the entrance of the trachea, preventing food and liquid from entering the windpipe and directing it into the esophagus and the digestive system. The functionality of the epiglottis is imperative in preventing dysphagia and subsequent aspiration, which can be fatal. Lastly, the vocal chords are two sheets of muscles for voice production. During phonation, the flow of air past the vocal cords causes it to vibrate and produce a pitch. The contraction and tightening of the vocal muscles, causes it to vibrate at a higher frequency and thus a higher pitch. A low pitch is produced when the muscles relaxes completely. The vocal cords are vulnerable to the formation of polyps and nodules, which arises from vocal abuse

2.1.3 The Trachea

The trachea is a long tubular structure (Figure 2.2) that is connected to and lies below the larynx. It also runs parallel to the esophagus and they are separated by the trachea-esophageal wall. During inspiration and expiration, the trachea acts as a passageway to carry air to and fro the nose or mouth and the lungs. This respiratory organ consists of three sub structures that help it perform its intended functions.

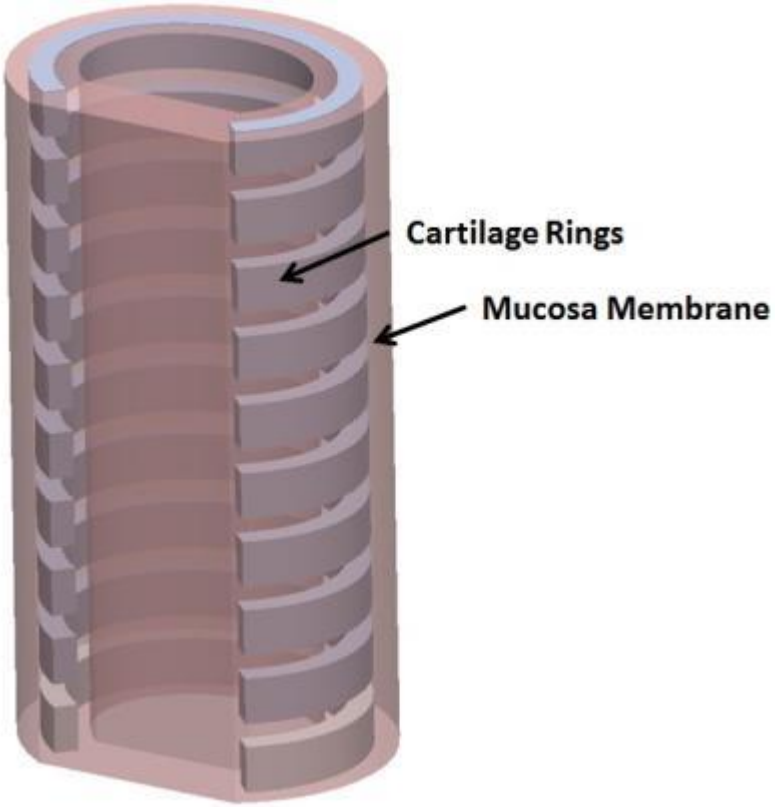

Figure 2.2: Gross anatomy of the trachea

The *Cartilaginous Rings:* the trachea is made up predominantly of the cartilaginous rings. The rings, comprising of hyaline cartilage, are C shaped and occupy an estimated two-thirds of the tracheal circumference. They are positioned parallel to each other, separated by narrow gaps in between, and are surrounded by the mucosa membrane.

Dimensions of cartilage rings are around 4mm in depth and 1mm in thickness and they vary from sixteen to twenty in a normal healthy human adult. The rings possess very good elasticity, which decreases with age due to calcification that might occur. The structural role of the cartilage rings is to provide skeletal support for the trachea by giving it its shape and to maintain airway patency at all times. During inspiration where there is negative pressure created in the airway in order to draw in air from the atmosphere, these rings resist the buckling of the trachea exerted by surrounding pressure. Their highly flexible nature also allows for the bending, stretching and rotation of the trachea in all three principal axes, which is caused by head and neck movements during daily activities of the individual. The cartilage rings are the only part of the trachea that cannot be regenerated after surgical removal currently.

The *Mucosa Membrane*: the membranous tissue lines the inner surface of the trachea and around the cartilaginous rings. It comprises of two distinct parts: the mucosa membrane and the sub-mucosa. The mucosa membrane consists of goblet cells that forms a pseudo-stratified ciliated columnar epithelium layer that produces mucus that warms, moistens, lubricate the inner air-tissue interface. The mucus also helps to trap foreign particles from the air that flows through the trachea to the lungs. The layer below the ciliated epithelium is the sub-mucosa that is composed mostly of loose tissues that host blood vessels, neurons and glands that supports the function of the mucosa membrane.

The ciliated epithelium: it is also known as pseudo-stratified epithelium and consists of a single layer of cells and cilia on the surface. The cilium is a mini finger-like projection that beats in synchronization with the other surrounding cilia. This synchronized beating effect produces a wave that transports mucus with trapped foreign

particles up to the pharynx where it is coughed out or consumed. This regulatory mechanism in the respiratory tract is important for individuals to clear the airway of obstruction from accumulated mucus production.

2.2 ENT Prostheses

Currently, the sole curative treatment for severe tracheal carcinoma is resection of the diseased portion. However, surgical removal of the airway is limited to 6cm in adults and longer resections would require a viable tracheal replacement in order to reduce anastomotic tension caused by the sutures at the distal ends. There are numerous trachea replacement grafts of various materials and designs proposed in literature, however, none provides a timely solution to this need (Doss, Dunn, Kucera, Clemson 2007, Kucera 2007).

The most renowned natural trachea implant is the “Spanish Windpipe” done by Macchiarini *et al.* (2010). The allograft was prepared by de-cellularizing the trachea tissue from a human donor and then repopulating it with the patient’s own cells, before implantation. This eliminates the need for the recipient to be on life-long immunosuppressant as the de-cellularization process removes all foreign antigens and cells on the donor tissue, leaving behind the ECM scaffold. Although the operation was highly successful, the long preparation time for the graft of a few months might not be suitable for emergency cases. Furthermore, the lack of suitable donors in addition to tracheal size compatibility, results in a limited supply pool of such grafts.

Artificial graft consists of the bulk of the tracheal graft experiments to date and is also one of the main studies of focus in this thesis. Artificial tracheal grafts are defined as

scaffolds created from synthetic materials or natural materials and are usually semi-biodegradable or non-biodegradable. Briefly, Tsukada *et al.* (2009) utilized a titanium stent covered with a copolymer sponge, they also went on to manufacture a Dacron tube reinforced with spiral stainless steel stents (Tsukada 2004). Several other studies explored the use of various materials coated with biodegradable sponge of some sort (Kawaguchi 2001, Nakamura 2009, Park 2012).

To date, there have been no suitable tracheal graft developed that is fit for commercialization. The high failure rates of these experimental prostheses can be attributed to the inability of the implanted prosthesis to host the regeneration of the ciliated epithelium within its lumen quickly (Yamashita 2007), insufficient or mismatched mechanical properties like flexibility and strength between the prosthesis and native tracheal tissues, and leakages of interstitial fluid into the lumen.

Quick epithelialization of the prosthesis lumen in less than 8 weeks is paramount in preventing the formation of granulation tissues and ensuring the success of the implant. Cilias on the epithelium aid in mucous clearance through synchronized beating motion and significantly affects the success of the implanted artificial airway. The migration of the ciliated epithelium originates from the native trachea at both the anastomoses sites (Tsukada 2004), therefore sufficient angiogenesis and vascularization are required throughout the prosthesis to supply nutrients to support the epithelium growth. It has also been established by many studies that the prosthesis should consists of non-biodegradable components to provide permanent mechanical stability to ensure airway patency since the resected cartilage rings do not regenerate, and biodegradable components like collagen to act as temporary space fillers for tissues in-growth (Shi 2005, Tsukada 2009, Yamashita

2007). As such, it is important that the non-biodegradable material that takes over the function of the cartilage rings should possess similar shape and biomechanical properties as the latter.

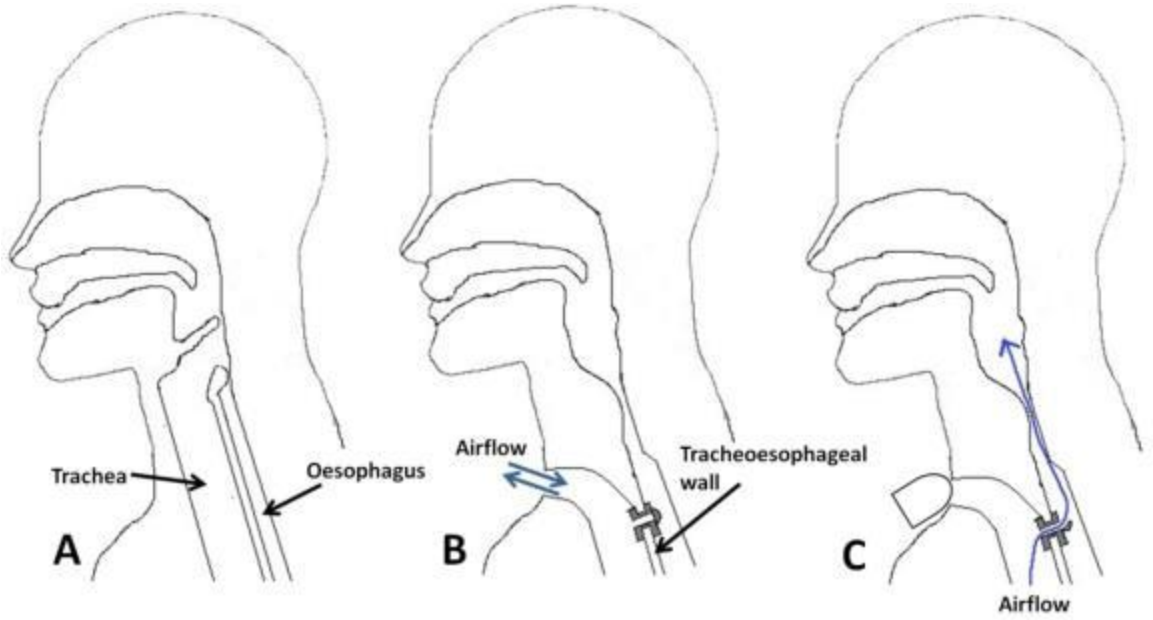

Figure 2.3: Anatomy before and after laryngectomy. (A) A healthy person, (B) a laryngectomee breathing with a regular voice prosthesis in the closed position to prevent liquid from entering the trachea from the esophagus and (C), a laryngectomee speaking by closing the stoma with a finger and forcing air through the voice prosthesis into the gullet and into the oral cavity.

There is a need for quality voice prosthesis to restore speech in patients after laryngectomy. Laryngectomy involves the surgical removal of the larynx and the separation of the trachea from the mouth, nose and esophagus (Tack 2006). A stoma is created on the neck, with the resected end of the trachea attached to the stoma to create a breathing outlet for the patient. Currently, the gold standard of speech rehabilitation for patients after larygectomy is the creation of a Trachea-Esophageal Puncture (TEP) between the trachea and esophagus and then followed by the insertion of the voice prosthesis (Lundy 2012) (Figure 2.3). The main function of TEP is to allow expiratory air to flow freely into the esophagus for voice production in the pharynx while preventing

food and liquid from leaking back into the airway (Ben Jebria1989, Hilgers 2013). Aspiration of any fluid into the airway can lead to pneumonia and other complications. Although there are many types of voice prostheses available commercially and under research, transprosthetic and periprosthetic leakages continue to be a problem (Kress, 2014, Thomson2007).

Formation of candida biofilm and inappropriate sizing shortens the lifespan of the voice prosthesis (Eerenstein 2002, Leunisse 2001). This causes inconvenience like the closure of the fistula, formation of granulation tissue and aspiration (Chone 2005). Transprosthetic leakages of food and liquid through the valve accounts for 80% of all leakages (Hilgers 2008) and often results in candida formation, which then prevents the complete closure of the valves, thus leading to even more leakages and candida formation. Candida also rapidly degrades the voice prosthesis and increase the flow resistance of air through it (Elving 2001), hence interfering with speech rehabilitation (Starmer 2011). The second problem faced by all prosthesis is the misfit of size in the fistula. Fistulas usually have irregular cross sectional areas; therefore it is hard to achieve an accurate fit since the prostheses have similar geometric shapes and fixed size ranges. A tight fit of the prosthesis will lead to the formation of granulation tissue while a loose fit results in periprosthetic leakages (Chone 2005).

Several works have been done to tackle these issues. Firstly, Leder *et al.* (2005) proposed the use of a modified flap mechanism to reduce transprosthetic leakages. However, a potential problem with all flap-valve prosthesis is the loosening of the polymeric hinge due to cyclic stress, leading to transprosthetic leakages. A prosthesis design with a deformable esophageal flange was also investigated (Van Den Hoogen

1997). Although it was effective in preventing leakages, the air flow resistance in the prosthesis was high, thus requiring patients to exert during speech. To address issues of periprosthetic leakages, Lewin *et al.* (2012) developed the use of enlarged collars to fill up additional space between the prosthesis and the tissue that results from fistula enlargement. The drawback of their method is that it causes uneven stress distribution due to the irregular shape of the fistula, potentially causing granulation and further widening.

2.3 Patient-Specific Design for Implants

Patient-specific or patient customized medical implants are lacking in the healthcare sector today. Most implants available on the market have a specific range of sizes and are modular in shape, hence it may not fit the anatomical requirements of the patient, leading to potential health issues, shorten implant lifespan or discomfort. Instead of a "one size fits all" approach, this thesis proposes a "one method fits all" methodology by inculcating patient-specificity in the implant design process. Patient-specific design refers to tailoring of the implant design according to the specific anatomical dimension of the affected patient's organ and its biomechanical properties. In patient-specific ENT implant designs, some of the ideal characteristics to attain are similarity in primary geometric properties and secondary properties like damping, flow resistance, surface topography. With advanced computer technology like CT imaging, CAD and finite element analysis, the implants can be customized to the requirements of each patient. Computational simulations can predict the *in-vivo* outcomes of prosthesis-tissue interactions through the input of geometrical and material parameters (Heissler 1998,

Hieu 2002). Hence, a tailored and better functioning prosthesis can be obtained by embedding computational design and simulation based on patient-specific models within the design framework.

Most of the patient-specific studies to date focus only on the hip and knee implants. To the author's best knowledge, there has not been any existing work done on patient-specific design methodologies for ENT implants. Harrysson *et al.* (2007) proposed a custom-designed orthopedic implant algorithm based on 3D reconstructed patient's CT imaging data input and finite element simulation. Their method was able to yield a more even stress distribution on the bone-implant interface and reduce uneven bone remodeling, hence prolonging implant lifespan. Similarly, Jun *et al.* (2010) and Dick *et al.* (2008) proposed the use of quick and effective CT-based finite element simulation to optimize the designs of orthopedic implants.

2.4 Carbon Nanocomposites

Carbon nanocomposites are desired in numerous industries such as healthcare, aerospace and defense due to their superior material properties and low weight to strength ratio (Plaseied 2006). Carbon nanocomposites, also known as carbon nanotubes reinforced composites, are defined as the doping of a base material (usually polymers or ceramics) with carbon nanotubes to enhance their physical, chemical and possibly biological properties as well. The improved mechanical, thermal and electrical properties in these materials are ideal for use in biological scaffolds (Kalappa 2008, Neitzert 2011, Thostenson 2003). The enhanced damping ability of carbon nanotubes (Khan 2011, Kireitseu 2008, Rajoria 2005) has also found its importance in medical applications with

high attenuation requirements, for example in artificial tracheal grafts. This is due to high amplitude and frequency forced vibrations caused by snoring or coughing, which damage the epithelial soft tissues (Cotado 2007, Simakov 2006) in the airway. This leads to impeded cellular regeneration by affecting the anchorage between the epithelium and sub-epithelium connective tissues (Boyd 2004, Paulsen 2002), resulting in impaired mucous clearance function and subsequent implant failure.

The superior mechanical properties of carbon nanocomposites may be attributed to the extremely high aspect ratio (surface to volume ratio) of the carbon nanotubes. A typical single walled carbon nanotube has a length of about 3-5 microns and a diameter of around 2 nanometers. As such, there is a high interfacial surface area between the nanotubes and the matrix material compared to other forms of inclusions in the micro-scale. Since the level of exposed surface area of the nanotubes directly affects the mechanical properties of the composite, it is ideal to disperse the CNT as homogeneous as possible during fabrication via acid treatment and ultrasonication mixing. This is to prevent agglomeration of CNT within the matrix which reduces its interfacial load transfer efficiency. With proper control of manufacturing conditions and good understanding of the material behavior, CNT may be manipulated within the nanocomposites to optimize the implant design.

There are existing work done on the biocompatibility and bioactive properties of CNT based composites (Chłopek 2006). Most of the experimental studies for carbon nanocomposites are focused on bone and cartilage replacements (Sahithi 2010), due to the superior elasticity and strength of the load bearing materials. Their non-biodegradability and excellent mechanical properties which make them ideal for

permanent implants to perform the structural function of the resected organ in cases where complete tissue regeneration is not possible like in airway replacements. In addition, these nanotubes reinforce the implants by reducing chances of brittle and ductile fracture under cyclic stresses because of improved interfacial strength and friction (Thostenson 2001). On the scaffold surfaces, CNT can be formulated to mimic the nano-topography of the Extra Cellular Matrix (ECM) to enhance cell recruitment, growth and activities (Harrison 2007, Tran 2009). Existing literature have indicated that CNT based substrates are proficient in accelerating the recruitment, growth and differentiation of osteoblasts and Mesenchymal stem cells, which are crucial for bone and cartilage formation, respectively (Harrison 2007, Mooney2008). Shi *et al.* (2007) has fabricated porous ultra-short SWCNT composites for bone tissue engineering and the material was proven to have superior osteoconductivity. Pure CNT coatings on bone fixation implants also improved bioactive behavior by providing a template for the deposition of hydroxyapatite layers during bone formation (Boccaccini 2007). Doping of natural materials, like chitosan and collagen, with CNT has shown increased functionality and structural stability (Lau 2008).

2.5 Material Modeling and Design

Characterization of the damping properties of carbon nanocomposites is important for ENT implants design optimization. This is because the material is subjected to constant vibratory stimulus from breathing, coughing and talking, which can affect the rate of regeneration of airway epithelium tissues growing into it. As mentioned in the previous section, the superior damping property of the carbon nanotubes is due to the high aspect ratio and interfacial friction (Bian 2003). Several works studying the damping

behavior of the CNT based composite materials have been performed to date (Dai 2007, Finegan 2003, Formica 2010, Gibson 2007). These works lack a mathematical model that can consistently predict the attenuation of CNT reinforced composites based solely on the given material properties. Mylavarapu *et al.* (2010) proposed an ultrasonic attenuation model for micro-spheres inclusions by taking into consideration the incident wave energy loss via absorption, scattering and cavity resonance of the inclusions within the matrix. A limitation of this multi-scale model is that the interactions between particles and matrix interfaces are neglected, which contributes significantly to the loss factor of energy transfer (Savvas 2012). Additionally, the model and experiments only focused on spherical type inclusions in the micron-scale, where else, CNT with its tubular nano-scale dimensions and higher aspect ratio may not be accurately represented by this model. Lin *et al.* (2010) proposed a model that utilizes a harmonic linearization method and Describing Function method to compute the interfacial friction damping of CNT-resin nanofibres composites to derive the damping loss through them. However, their model assumes that all CNT are perfectly aligned along the axial direction and perfectly dispersed, which is rarely the case in reality. Joel *et al.* (2009) proposed a method to determine the attenuation coefficient through multi-wall CNT composites using Kramers-Kronig relations equation. One identified shortcoming is that the model was derived based on acquired experimental data and it is unable to generate the predicted attenuation value based solely on the material's physical properties and inclusions weight fraction.

The modeling of the stress-strain properties in nanocomposites is critical in dynamic load bearing applications such as implants in knee, hip and tracheal prostheses (Chua 2013, Lee 2011, Liu 2007). It is difficult to deterministically quantify the design

outcome *in-vivo* due to variation in fabrication and material conditions, therefore many implant design processes, mainly in orthopedics, have employed probabilistic modeling approaches ranging from wear models to finite element simulations for evaluation and optimization (Kayabasi 2008, Layman 2010, Laz 2010, Pal 2008).

There are currently numerous works and techniques explored in the mathematical modeling of mechanical properties of nanocomposites, such as the Halpin-Tsai mean field approach (Affdl & Kardos 1976, Shanmuganathan 2010), the Halpin Kardos model (Halpin & Kardos 1972), mechanical percolation model (Favier 1997) and modified series model (Kanagaraj 2007). These constitutive models predict the mechanical properties of the nanocomposites based on input variables like inclusion aspect ratio, fiber weight fraction, Young's modulus of fibers and matrixes and many more. However, it remains challenging to accurately obtain accurate results from these models due to uncertainties introduced into the variables like differences in fabrication techniques (Ma 2010), handling inconsistencies and differences in quality of different brands of reagents used.

2.6 Tissue-Material Interaction Modeling

Mathematical modeling of tissue-material interactions have been intensively researched on and integrated into biodegradable scaffold design processes. An example of such an interaction covered in this thesis is the effect of a biodegradable scaffold on the ingrowth of tissues. The purpose of such simulation study is to ensure that the rate of tissue growth and scaffold degradation are matched as closely as possible in order to maintain the overall structural integrity (O'Dea 2012, Sengers 2007).

Most works modeling scaffold degradation and tissue growth are deterministic in nature and focuses only on the overall volume change of scaffold and cells with time, while neglecting the stochastic nature of the components in the system (Alemani 2012). Simulation of the stochastic degradation behavior of the scaffold *in-vivo* while maintaining close consistency with the experimentally established kinetics law is paramount to the deeper understanding of the transient changes of the scaffold-tissue hybrid structure. A major drawback of current simulation works is due to the computationally intensive multiple partial differential functions, which do not produce timely solutions for scaffold design needs. Furthermore, such complex biological computational methods are often hard to comprehend and rarely utilized in reality.

Traditionally, the stochastic degradation of scaffolds has often been modeled using Gopferich's probability density function model (Göpferich 2002):

$$p(t, \lambda) = \lambda e^{-\lambda t}, \tag{2.1}$$

where λ is the degradation rate constant, which is based on Erlang's first order distribution and dependent on material type. However, the computed time dependent mass changes of the scaffold using Gopferich's probabilistic model deviates from that of the experimentally established pseudo-first order degradation kinetics (Ng 2012). This severely limits the applicability of the model in actual scaffold designs as it is mathematically inaccurate. Garzón-Alvarado *et al.* (2012) introduced a model of porous scaffold degradation using RD (reaction-diffusion) systems that runs on the degradation algorithm developed by T. Adachi *et al.* (2006). Similarly, it is not known if their simulation results are consistent with the pseudo-first order reaction kinetics and is computationally intensive and expensive. Chen *et al.* (2011) attempted to improve

Gopferich's classical stochastic hydrolysis model by adding the effects of both fundamental hydrolysis and the accelerating effect of auto-catalysis. Chao *et al. (*2009) utilized a multiple-particle random walk model to simulate and predict scaffold degradation. However, their model was not experimentally verified and is mostly hypothetical in nature.

The stochasticity and non-uniformity of cell proliferation and migration have traditionally been represented using Cellular Automata (CA) random walk algorithm model (Dewdney 2008). Other CA methodologies include Garijo *et al.* (2012) who utilized a CA model to simulate cell migration, proliferation and differentiation on a 2D circular lattice and M. Markus *et al.* (1999) who modeled the anisotropic growth of tissues using a quasi-stochastic discrete CA model. However, these works were confined to 2D and are not applied in 3D regeneration scenarios which have more useful applications.

The merging of cellular in-growth and scaffold degradation models has been studied extensively for the optimization of implants design. This is especially useful for the development of the artificial trachea prosthesis, whereby a substantial portion of the scaffold consists of biodegradable collagen sponge and simulation is required to ascertain and evaluate the design outcome. O'Dea *et al.* (2012) investigated the relationship between tissue growth and scaffold in a bioreactor using deterministic approaches and partial differential equations (PDE). However, their results only showed the overall mass and volume changes of the cells and scaffold but did not take into consideration the probabilistic aspect of such systems. Chung *et al.* (2010) proposed a hybrid cellular automaton algorithm to model cell growth in tissue engineering constructs *in-vitro,* but

their growth model was limited as it lacked the impact of the scaffold geometry and spatial steric hindrance on cell movement and division. Sanz-Herrera *et al.* (2010) proposed a multi-scale computational model utilizing a strain energy density based rule for bone scaffold degradation and a Fickean cell invasion model for tissue in-growth. A drawback of their combined models is the unsuitability for non-load bearing scaffolds situations whereby hydrolysis is largely dependent on the porosity of the material. In the work done by Lenthe *et al.* (2007), direct micro-architectural CT imaging was used to construct and observe the tissue growth into scaffold *in-silico,* to assess the scaffold degradation kinetics and tissue response. However, their experimental simulation lacked universally consistent computational models that can predict outcomes in hypothetical conditions different from their stipulated specific conditions.

2.7 Overview of Proposed Framework

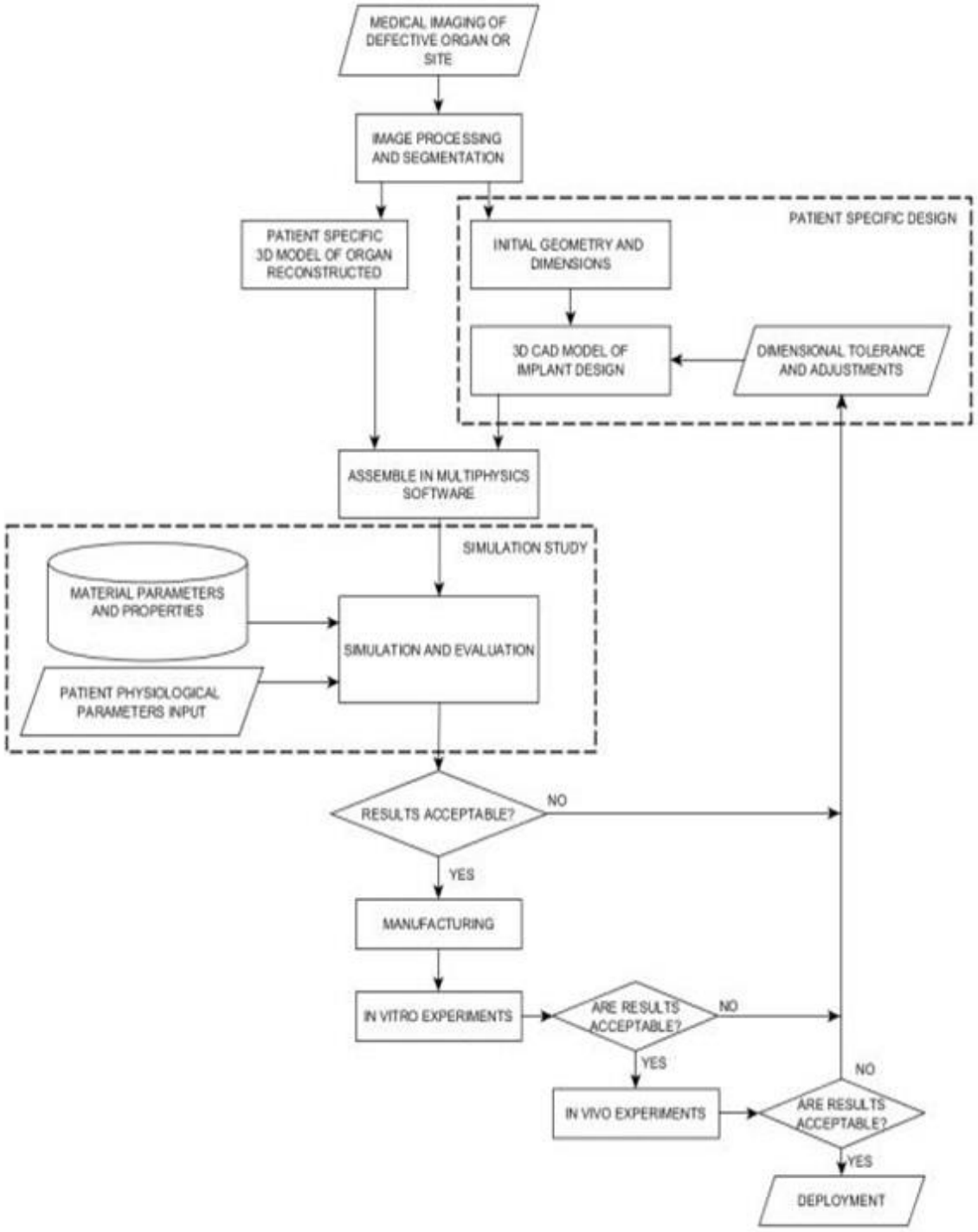

Figure 2.4: Simulation-based design algorithm for medical implants. The proposed material attenuation model and probabilistic predictive algorithm in Chapter 3 and 4, respectively, are applied during simulation and evaluation of the CAD design.

Computer aided design and simulation have been the focus of many medical device developmental processes. It has also been reported by FDA that the design and development of new medical devices and implants should involve computational simulation as part of the validation criteria. The benefits brought about through the use of such technology are tremendous. Amongst which, are time and cost savings by cutting down on lag time between design iterations and from reducing material wastage. Simulations also help to reduce the number of *in-vitro* and *in-vivo* experiments needed and thus scaling down on the man-hours required as well as reducing the number of animals sacrificed. The additional element of patient-specific design to the process helps to increase the effectiveness of the device by tailoring it to the anatomical requirements of the individual. However, simulation-based patient-specific design processes are not widely used in medical device development currently and are mostly just confined to orthopedics implants. There is a lack of studies conducted on patient-specificity in soft tissue organ scaffold designs, like the trachea, which this thesis hopes to explore.

The proposed patient-specific simulation-based design algorithm for general implant types is depicted in Figure 2.4. Ideally, the process should begin with the acquisition of the volumetric imaging data of the organ or site of interest. This can be achieved through state of the art clinical MRI or CT imaging devices in hospitals and laboratories. The volumetric imaging data is an important ingredient for the reconstruction of the 3D model of the patient's physiological environment to be remedied and also for the design of the patient-specific implant model. Image processing and segmentation with computational software like MATLAB would be required for reconstruction and design. The following sections then discusses in detail the patient-

specific design, simulation studies and experimental validations in chronological order with respect to the proposed algorithm.

2.7.1 Patient-Specific Design

Patient-specific design forms a critical component of the implant design process. It involves the tailoring of the implant geometry and dimensions to the specific anatomical needs of the patient. It is hypothesized that this would bring about a better and closer fit of the implant and better performance *in-vivo*, which may be in terms of stress distribution, load bearing and dynamic motion, over current modular implants. Volumetric imaging data is first processed and constructed to acquire the 3D shape and size of the organ or site, which is then imported into CAD software like Solidworks or AutoCAD to design the implant. The advantage brought about by this method is that it allows an accurate representation of the irregularities of the geometry of the defect site on the implant model quickly and conveniently. Another benefit brought about by the use of 3D modeling of these implants is that it allows for computational simulation studies to evaluate its design and quick alterations can be implemented to the designs accordingly. This is vital in elastic implants whereby a certain degree of compression or tension is required for it to perform its task optimally. Tolerances may also need to be factored in to account for manufacturing dimensional discrepancies like part shrinkage from rapid prototyping and molding.

2.7.2 Simulation and Experimental Validation

Computational simulation is an integral part of the design process for the evaluation and improvement of the design. This iterative and optimization process leads to better quality of implant designs while reducing the time and finances required to

conduct a large number of experiments. Depending on the nature of the implant, simulation may range from flow in voice prostheses, stress strain concentrations in load bearing implants or even corrosion rate in biodegradable scaffolds. The idea of computational simulation in patient-specific design algorithm is also to study the tissue-implant interactions based on the acquired patient imaging data. After volumetric reconstruction of the patient's site of interest and the 3D model of the designed implant, these are imported into a multi-physics simulation program, like COMSOL. Material behavioral data and parameters are then acquired from the online library sources or journal articles and then assigned to both organ and inorganic components. Patient physiological inputs like stress, motion, flow rate or pH, just to name a few, can then be used to evaluate the outcome of the tissue-implant assembly. Based on the results, adjustments are then made to the implant design and simulation is performed on an iterative basis until optimized.

Although the integration of simulation-based design can help to significantly reduce the number of experiments performed, the latter is still vital in the validation of *in-silico* results. Experimental works may be classified under *in-vitro* and *in-vivo*, depending on whether it is carried out outside or inside the body, respectively. Careful planning and execution of *in-vitro* experiments reduces the number of *in-vivo* experiments needed and thus possibly cutting down on the loss of lives. *In-vivo* experiments are first performed in animals before they are carried out in humans during the last leg of the product development cycle.

2.8 Conclusion

The multi-faceted approach to the development of medical implants makes it a challenging field. In the design aspect, there is currently a need for patient-specific design flow process needs to be developed and optimized for soft tissue medical implants. The nature of soft tissue compared to hard tissues, like bones, make it more difficult to characterize for design parameters due to high elasticity and deformability. Besides material modeling, the tissue-material interactions need to be carefully evaluated to reduce risks of rejection or mismatch. The advantages of having such models allows for efficient simulation-based design and optimization, which can reduce costs and time required. Lastly, the choice of carbon-based nanocomposites as the implant material may offer superior mechanical properties and biological properties for wound healing and tissue regeneration. However, more cytotoxicity studies need to be conducted to evaluate the long term effects of such materials in the body.

Chapter 3

ATTENUATION PREDICTIVE MODEL FOR CARBON NANOCOMPOSITES

Chua M, Chui CK (2015). New Attenuation Predictive Model for Carbon Based Nanocomposites. *Transactions in Nanotechnology, IEEE*. doi: 10.1109/TNANO.2015.2396536

This chapter contains work from the above cited article which is accepted in 2014. A predictive model for the attenuation of sound waves through the composite that takes into consideration the Rayleigh scattering function, absorption, resonance and interfacial friction of the embedded fibers is proposed and investigated. These factors are dependent on the size, thickness, density, porosity, Young Modulus and volume fraction of the nanofibers or nanotubes. Carbon Nano Fibers Reinforced PDMS (CNFRP) and Single Walled Carbon Nano Tubes Reinforced Poly-di-methyl-siloxane (SWCNTRP) composites were investigated. Ultrasonic testing and measurement of sound wave attenuations through the material were done to validate the proposed model and results are shown to be consistent. Section 3.1 provides an overview on attenuation and modeling in composites while Section 3.2 presents our new attenuation model. Section 3.3 contains details of the experimental work performed to validate the simulation results. The final section in this chapter discusses the results of the proposed model.

3.1 Attenuation

Carbon nanofibers reinforced composites have found many applications in industries such as healthcare, aerospace and defence due to their enhanced material properties and low weight (Khare 2005, Plaseied 2006). Carbon based nanocomposites used in medical implants can enhance the mechanical, thermal and electrical properties of the scaffold (Kalappa 2008, Khan 2013, Neitzert 2011, Thostenson 2003), many characterization studies have been performed on these materials (Jin 2006, Ngo 2007, Zhengchun 2009). Another advantage of the use of carbon nanofibers in composites is their enhanced damping ability (Khan 2011, Kireitseu 2008, Rajoria 2005). This is important in applications with high damping requirements, for example in artificial tracheal grafts (Chua 2013). High amplitude and frequency forced vibrations due to snoring or coughing may cause damage to epithelial soft tissues (Cotado 2007, Simakov 2006) in the trachea, which may retard regeneration by affecting the anchorage between the epithelium and sub-epithelium connective tissues (Boyd 2004, Paulsen 2002).

Several modeling and characterization of the damping properties of the nanofibers composite materials have been investigated (Dai 2007, Finegan 2003, Formica 2010, Gibson 2007, Mylavarapu 2010). It has also been established that much of the damping in the composites are caused by the interfacial friction between the fibers and matrix (Bian 2003, Huang 2010, Lin 2010, Savvas 2012, Zhou 2004). Related works done by Mylavarapu *et al.* (2010), utilizes a model that predicts the energy loss via absorption, scattering and resonance of the inclusions in the matrix. A limitation of this model is that the interactions between particles and matrix interfaces are neglected, which contribute significantly to the loss factor of vibrations (Savvas 2012); in addition, the model and

experiments only focused on spherical type inclusions. Lin *et al.* (2010) proposed a model that utilizes a harmonic linearization method and Describing Function method to compute the interfacial friction damping of CNT-resin nanofibers composites to derive the damping loss through them. Joel *et al.* (2009) proposed a method to determine the attenuation coefficient through multi-wall CNT composites using Kramers-Kronig relations. A limitation of the latter's work is that the model is derived based on experimental readings and it is unable to generate the predictive attenuation value based solely on the material's mechanical properties and fibers weight fraction. The proposed model in this chapter provides a physical explanation to the attenuation of the nanocomposite materials at the nano-scale level, while allowing the coefficients to be computed using existing material properties and weight ratio of fibers. The results are validated with two different experiments: ultrasonic testing and attenuation measurements of harmonic sound waves of different frequencies propagating through the material.

3.2 Methods and Materials

3.2.1 Attenuation Predictive Model

The development of our new attenuation predictive model is based on the presence, size and dimensions of the inclusions (SWCNT and CNF) in the polymeric matrix and how it affects the attenuation of the incident wave. It has been shown in Mylavarapu *et al.* (2010) that the Rayleigh scattering function for elastic spherical inclusions, adsorption of energy by hollow air spaces in spherical inclusions and resonance of each inclusion contributes to the attenuation of the material. The proposed model incorporates and modifies these factors for SWCNT and CNF inclusions and also

considers interfacial friction between the inclusions and matrix, which is an important contributing factor to attenuation (Lin 2010, Savvas 2012). According to studies conducted, an assumption was made that inclusion-inclusion interactions can be neglected (Berryman 1980) and hence each inclusion can be treated independently for all volume fraction and that the combined overall effect of the inclusions is the arithmetic addition of each individual ones.

Material properties of Single Walled CNT (Cheap Tubes Inc, USA) and CNF (Sigma Aldrich, Singapore) that were used in this study are documented in the table below (Table 3.1). The values of densities, lengths, outer and inner diameters of both SWCNT/CNF were provided by the suppliers.

TABLE 3.1
Material properties of single walled CNT and CNF

Material Properties	Single walled CNT	CNF
Density (g/cm^3)	2.1	1.5
Length (μm)	5-30	50-100
Outer Diameter (nm)	1-2	125-150
Inner Diameter (nm)	0.8-1.6	50-70
Poisson's Ratio (Krishnan 1998, Treacy 1996)	0.3	0.3
Young's Modulus (TPa) (Srivastava 2003, Wei 2004)	1	0.03

The incident sound or ultrasonic wave is assumed to be applied uniformly across the surface perpendicular to the direction of travel with a pressure of amplitude P_o. A shift in applied direction or uneven pressure will affect attenuation readings due to changes in path of wave propagation. The model also assumes that the planar energy wave propagates through the material without change in directions. This would make the model more applicable for thinner samples due to lesser degree of wave refraction while

travelling. A fraction of the energy of the incident wave will be dissipated due to the absorption by SWCNT and CNF in the matrix and the matrix medium itself. The equation of the incident wave intensity, I_o, is given in Equation (3.1) below:

$$I_o = \frac{P_o^2}{\rho V_l}, \tag{3.1}$$

where ρ is the density of the material and V_l is the longitudinal wave speed.

Studies conducted by Ying *et al.* (1956), showed that the Rayleigh scattering expression in isotropic elastic solid medium with isotropic elastic spherical inclusions of volume V can be written as:

$$\gamma_{scatter} = V^2 K_p^4 g_e \,, \tag{3.2}$$

$$g_e = \frac{3(K_1-K_2)^2}{(3K_2^2+4G_1^2)} + \frac{1}{3}\left[1 + 2\left(\frac{K_1}{G_1}+\frac{4}{3}\right)^{1.5}\right]\left(\frac{\rho_2-\rho_1}{\rho_1}\right)^2 + \left[2 + 3\left(\frac{K_1}{G_1}+\frac{4}{3}\right)^{2.5}\right]\frac{40(G_1-G_2)^2}{(6K_1G_2+9K_1G_1+12G_1G_2+8G_1^2)}\,, \tag{3.3}$$

$$G = \frac{E}{2(1+\nu)}\,, \tag{3.4}$$

$$K = \frac{E}{3(1-2\nu)}\,, \tag{3.5}$$

where K_1 and K_2 refer to the bulk moduli of the medium and inclusions, respectively; G_1 and G_2 refers to the rigidity moduli of the medium and inclusions, respectively; and K_p is the wave number. Williams *et al.* (1983) states that if the incident wavelength is very long compared to the longest dimension of the inclusion and if the condition $a.K_p<1$ is met (where a is the longest dimension of the inclusion and K_p is the wave number), the exact shape of the inclusion has little effect on the attenuation. The attenuation is thus solely dependent on the volume of the particle. Hence, V is calculated as the overall volume of each CNT and CNF, inclusive of its hollow core.

Although there is a range of SWCNT and CNF size variations in the composite, the effective wave behavior will be dominated by the average documented dimensions as shown in Table 3.1. Therefore, the total energy lost due to scattering $P_{scattering}$ is the arithmetic sum of each individual particulate effect:

$$P_{scattering} = I_o \sum_{i=1}^{n} \gamma_i = \frac{P_o^2}{\rho V_l} \sum_{i=1}^{n} \gamma_i. \quad (3.6)$$

Besides energy lost due to the scattering effect of the inclusions in the matrix, energy is also lost through absorption by the voids within the CNT and CNF. The energy lost by a single void, may be expressed by:

$$P_{single\ void} = I_o \gamma_{a,i}, \quad (3.7)$$

where

$$\gamma_{a,i} = \frac{4\pi r_i^2 l}{\lambda}. \quad (3.8)$$

$\gamma_{a,i}$ is the absorption cross section of a single cylindrical void within the hollow CNF/CNT, which is directly proportional to the volume of the hollow cavity and inversely proportional to the wavelength of the incoming longitudinal wave (Ishimaru 1977, Mechel 2002), λ is the wavelength of the incoming wave, l is the average length of the CNT/CNF and r_i is the inner radii of the CNT/CNF (in the case of the single-walled CNT, r_i may be approximated to the outer radii). Therefore, total energy loss due to void absorption is:

$$P_{voids} = \frac{P_o^2}{\rho V_l} \sum_{i=1}^{n} \gamma_{a,i}, \quad (3.9)$$

It was discussed above that interfacial friction between the inclusions and matrix contributes to the attenuation rate of the wave passing through the material. Based on the interfacial model by Lin *et al.* (2010), a modified frictional model for single-walled CNT

and CNF is proposed in this chapter (Figure 3.1). Loss of energy occurs from the slips between the outer surface of the inclusion and the matrix during vibration. From the vibration analysis aspect, a single cell element can be modeled as a mass-spring system with two springs representing the stiffness of the matrix and the outer layer of the inclusion. In this model, k_m and k_f are the stiffness of the matrix and CNT/CNF while m_m and m_f are the masses of the matrix and CNT/CNF, respectively. The force f_f denotes the interfacial friction limits between the CNT/CNF and matrix at which slips between the two surfaces occur. The expressions are as follows:

$$k_f = \frac{E_f A}{l}, \tag{3.10}$$

$$k_m = \frac{\pi E_m r_o^2}{l V_f}, \tag{3.11}$$

$$f_f = 2\pi r_o l \tau_c, \tag{3.12}$$

$$f_f = (k_m + k_f)x. \tag{3.13}$$

Equation (3.12) applies only when the condition of the interfacial force limit between the inclusions and matrix is reached, hence slipping occurs. Equation (3.13) is valid and applicable when $f_f < 2\pi r_o l \tau_c$ or when the interfacial friction is less than the limit and no slippage occurs. Slipping occurs when the input force exceeds the interfacial force limit, which can be calculated by multiplying the area of interfacial contact, $2\pi r_o l$, with the critical interfacial shear stress, τ_c. For values of forces below the limit, it is assumed that there is no slip condition and the force is linearly proportional to the displacement, x.

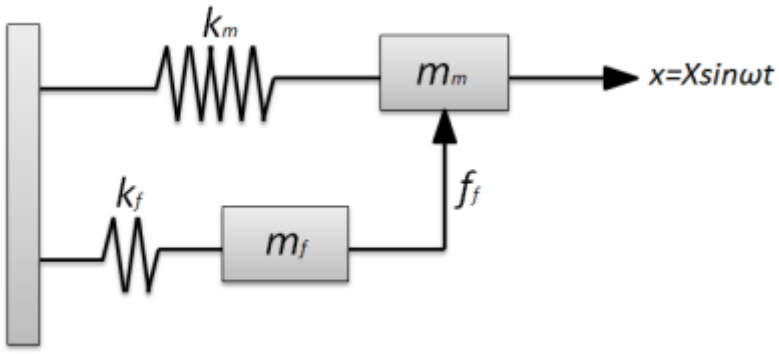

Figure 3.1: Proposed interfacial friction model where k_m=stiffness of matrix, k_f = stiffness of CNT/CNF, m_m=mass of matrix, m_f=mass of CNT/CNF and f_f=interfacial friction limits.

If δ is the critical vibration amplitude displacement for slipping to occur, it can be assumed that no slip would occur if the input amplitude displacement, X_o, is small ($X_o < \delta$). In this case, the cell behaves like an elastic linear spring with a spring constant of k_m+k_f. However, if the input amplitude is more than the critical displacement, slipping would occur in the model and the energy loss can be calculated and solved using a hysteresis loop as shown in Figure 3.2. The general explanation for the formation of the hysteresis loop and the energy dissipation during a vibration cycle is discussed. When x increases by less than the critical displacement for slipping, the force-displacement relationship will follow the path **OP** according to Equation (3.13). When x reaches δ and more, slipping occurs and the graph follows the path **PQ**, characterized by Equation (3.12). Upon reaching the maximum amplitude X_o, the displacement reverses and follows QR with no slip and then RS with slipping between interfaces. Finally, it follows **ST** and **TP** back to **P** and forms a complete vibration cycle. The cycle then repeats itself depending on the frequency of the input vibration.

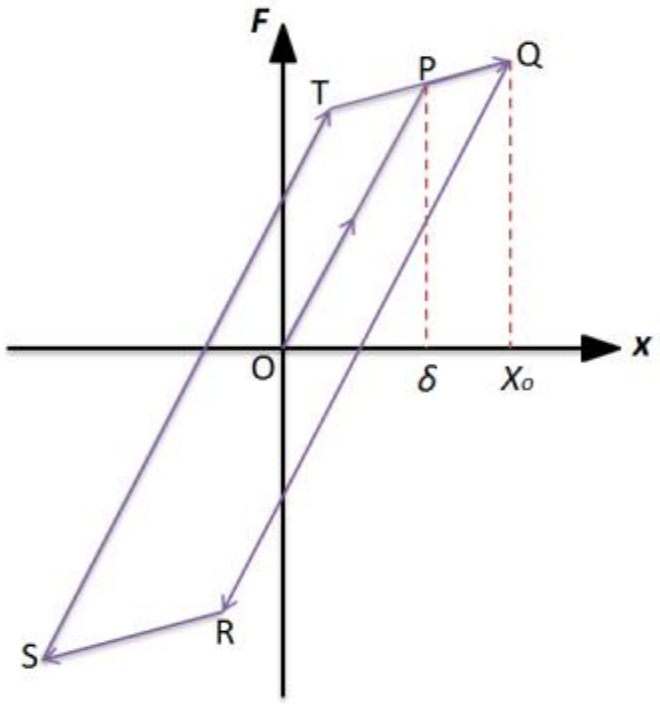

Figure 3.2: Force-displacement relationship for the case when $X_o > \delta$.

From the hysteresis loop derived on force-displacement graph, the damping loss factor due to interfacial friction of the fibers-matrix can be determined. Due to the nonlinearity of the system model, a suitable linearization algorithm is needed to obtain the damping loss factor. Describing Function method has been commonly used for linearization (Gelb 1968). It allows for an accurate and equivalent linear modeling of non-linear characteristics. The Describing Method substitutes a system's nonlinearity with a linear gain that is able to yield similar responses of the original nonlinearity. Between **OP**, there is no slip, hence the effective stiffness is k_m+k_f, while at **PQ**, slipping at the interface occurs, resulting in the effective stiffness being k_m. The x-coordinate for Point **T** is $2\delta-X_o$ and the y-coordinate of **P** is first determined as $(k_f+k_m)\delta$. Next, the y-coordinate of **T** is calculated as the y-coordinate of **P** subtracted by the multiplication of stiffness of **PQ** with the horizontal scalar of **TP**. The final coordinates of point **T** are

obtained as (2δ-X_o, $2k_m\delta + k_f\delta - k_mX_o$). Following which, the value of θ_1 can be computed as:

$$X_o sin\theta_1 = 2\delta - X_o \rightarrow \theta_1 = sin^{-1}\frac{2\delta - X_o}{X_o}. \quad (3.14)$$

After determining θ_1, the Describing Function coefficient a_1 and b_1 can be utilized to calculate the loss factor due to interfacial friction. The Describing Function of the force-displacement relationship graph of the basic cell element allows for the calculation of the loss factor, which is the ratio of the energy output, b_1, to the energy input, a_1, of the hysteresis loop. The coefficient b_1 is the imaginary part of the transfer function of the equivalent linearized system corresponding to the input amplitude, X_o, while a_1 is the real part of the transfer function. Both coefficients are calculated as follows:

$$a_1 = \frac{1}{\pi}\left[\int_{\theta_1}^{2\pi} f(X_o\, sin\,\theta\,, X_o\omega\, cos\,\theta)\, sin\,\theta\, d\theta\right]$$

$$= \frac{2}{\pi}\left[\int_{\theta_1}^{\pi/2} f(X_o\, sin\,\theta\,, X_o\omega\, cos\,\theta)\, sin\,\theta\, d\theta + \int_{\pi/2}^{\pi+\theta_1} f(X_o\, sin\,\theta\,, X_o\omega\, cos\,\theta)\, sin\,\theta\, d\theta\right], \quad (3.15)$$

$$b_1 = \frac{1}{\pi}\left[\int_{0}^{2\pi} f(X_o\, sin\,\theta\,, X_o\omega\, cos\,\theta)\, cos\,\theta\, d\theta\right]$$

$$= \frac{2}{\pi}\left[\int_{\theta_1}^{\pi/2} f(X_o\, sin\,\theta\,, X_o\omega\, cos\,\theta)\, cos\,\theta\, d\theta + \int_{\pi/2}^{\pi+\theta_1} f(X_o\, sin\,\theta\,, X_o\omega\, cos\,\theta)\, cos\,\theta\, d\theta\right]. \quad (3.16)$$

Therefore, to solve the integrals and obtain a_1 and b_1, the equations for **TQ** and **QR** of the hysteresis loop can be determined as follows:

TQ: $F = k_m x + k_f \delta$, (3.17)

QR: $F = (k_m + k_f)x + k_f \delta - k_f X_o$. (3.18)

Using Equations (3.17) and (3.18), the values of a_1 and b_1 can be integrated as shown:

$$a_1 = \frac{2}{\pi}\left[\int_{\theta_1}^{\pi/2} f(X_o \sin\theta, X_o\omega\cos\theta)\sin\theta\, d\theta + \int_{\pi/2}^{\pi+\theta_1} f(X_o \sin\theta, X_o\omega\cos\theta)\sin\theta\, d\theta\right]$$

$$= \frac{2}{\pi}\left[\int_{\theta_1}^{\pi/2}\left[k_m X_o \sin\theta + k_f\delta\right]\sin\theta\, d\theta + \int_{\pi/2}^{\pi+\theta_1}\left[\left(k_m + k_f\right)X_o \sin\theta + k_f\delta - k_f X_o\right]\sin\theta\, d\theta\right]$$

$$= \frac{2}{\pi}\left[k_m X_o\left(\frac{\pi}{4} - \frac{\theta_1}{2} + \frac{1}{4}\sin 2\theta_1\right) + k_f\delta\cos\theta_1\right] + \frac{2}{\pi}\left[(k_m + k_f)X_o\left(\frac{\pi}{4} - \frac{\theta_1}{2} + \frac{1}{4}\sin 2\theta_1\right) + (k_f\delta - k_f X_o)\cos\theta_1\right], \quad (3.19)$$

$$b_1 = \frac{2}{\pi}\left[\int_{\theta_1}^{\pi/2} f(X_o \sin\theta, X_o\omega\cos\theta)\cos\theta\, d\theta + \int_{\pi/2}^{\pi+\theta_1} f(X_o \sin\theta, X_o\omega\cos\theta)\cos\theta\, d\theta\right]$$

$$= \frac{2}{\pi}\left[\int_{\theta_1}^{\pi/2}\left[k_m X_o \sin\theta + k_f\delta\right]\cos\theta\, d\theta + \int_{\pi/2}^{\pi+\theta_1}\left[\left(k_m + k_f\right)X_o \sin\theta + k_f\delta - k_f X_o\right]\cos\theta\, d\theta\right]$$

$$= \frac{2}{\pi}\left[k_m X_o\left(\frac{1}{2} - \frac{1}{2}\sin^2\theta_1\right) + k_f\delta(1 - \sin\theta_1)\right] + \frac{2}{\pi}\left[(k_m + k_f)X_o\left(\frac{1}{2}\sin^2\theta_1 - \frac{1}{2}\right) + (k_f\delta - k_f X_o)(-\sin\theta_1 - 1)\right]. \quad (3.20)$$

The loss factor due to interfacial friction of a single CNT/CNF can thus be determined as the ratio of the output over the input energy:

$$\gamma_{friction,i} = \frac{b_1}{a_1}. \quad (3.21)$$

Total energy loss due to interfacial friction in the nanocomposite is:

$$P_{friction} = \frac{P_o^2}{\rho V_l}\sum_{i=1}^{n} \gamma_{friction,i}. \quad (3.22)$$

According to Kinra *et al.* (1983) a portion of the energy from the wave is absorbed due to the resonance of the solid inclusion. The resonance cross section of a single inclusion is proportional to the volume of the CNF and inversely proportional to the wavelength, as shown in Equation (3.23):

$$\gamma_{resonance,i} = \frac{4\pi(r_o^2 - r_i^2)l}{\lambda}, \tag{3.23}$$

where r_o and r_i are the average outer and inner diameter of the CNF, respectively and l is the average length of the CNF. For single-walled CNT, the wall thickness is considered to be negligible and thus resonance loss may be omitted from its attenuation calculations. Total energy loss due to resonance is then defined as:

$$P_{resonance} = \frac{P_o^2}{\rho V_l} \sum_{i=1}^{n} \gamma_{resonance,i} . \tag{3.24}$$

The energy wave input and output into the nanocomposite material may be denoted in Equations (3.25) and (3.26), respectively, with A being the planar area of the sample that is perpendicular to the direction of wave travel, β being the attenuation coefficient and L is the sample length:

$$P_{in} = \frac{P_o^2}{\rho V_l} A , \tag{3.25}$$

$$P_{out} = \frac{\left(P_o e^{-2\beta L}\right)^2}{\rho V_l} A . \tag{3.26}$$

By using the laws of conservation of energy, the output energy can be equated to the input energy subtracted by the energy loss due to scattering, void absorption, interfacial friction and resonance of the inclusions:

$$P_{in} - P_{scattering} - P_{voids} - P_{friction} - P_{resonance} = P_{out} , \tag{3.27}$$

$$\frac{P_o^2}{\rho V_l}A - \frac{P_o^2}{\rho V_l}n\gamma_i - \frac{P_o^2}{\rho V_l}n\gamma_{a,i} - \frac{P_o^2}{\rho V_l}n\gamma_{friction,i} - \frac{P_o^2}{\rho V_l}n\gamma_{resonance,i} = \frac{P_o^2 e^{-4\beta L}}{\rho V_l}A\ .$$

(3.28)

By rearranging the terms and eliminating common variables, the equation may be reduced to:

$$A\left(1 - e^{-4\beta L}\right) = n(\gamma_i + \gamma_{a,i} + \gamma_{friction,i} + \gamma_{resonance,i}), \quad (3.29)$$

$$\beta = -\frac{1}{4L}ln\left[1 - \frac{n}{A}\left(\gamma_i + \gamma_{a,i} + \gamma_{friction,i} + \gamma_{resonance,i}\right)\right]. \quad (3.30)$$

where *n* is the number of inclusions that is covered by the sample cross section area or the area of the energy wave, whichever is lower. The derived attenuation Equation (3.30) may be applicable for both thin single-walled CNT as well as hollow CNF embedded in a polymeric matrix. However, the attenuation due to the polymeric matrix needs to be factored into the equation to obtain the overall attenuation of the overall nanocomposite:

$$\beta_{compoaite} = \beta + \beta_{matrix}\ . \quad (3.31)$$

The model results can be validated with experimental results obtained by subjecting samples of nanocomposite of varying fiber fractions to ultrasonic testing and audible frequencies sound waves, and measuring the attenuation loss.

3.2.2 Experiments

Computational simulation was first performed with the proposed attenuation model. The $\beta_{composite}$, which is the overall attenuation of the nanocomposite material, can be computed using Equations (3.2), (3.8), (3.21), (3.23), (3.30) and (3.31). Material properties and geometries from Table 3.1 were used in the predictive simulation and 500 simulations per weight fraction of each composite type were performed. Since there is a range of values for the length, inner and outer diameter of each inclusion in the

composite, every simulation utilized random values within the stated range of the three dimensions for computation. After which, the results from all 500 simulation runs were summed together and averaged out. From the simulation results, the attenuation rate through a specific carbon-based nanocomposite material is hypothesized. Attenuation experiments were conducted to validate the proposed theoretical model, one involving ultrasonic waves and the other involving harmonic sound waves. Fabrication procedures of the carbon-based nanocomposites are discussed below.

Samples of varying mass fractions of SWCNT and CNF in PDMS (Sylgard® 184 Silicone Elastomer Kit, Dow Corning, Singapore) were fabricated in a cylindrical form with dimensions of 25mm diameter and 10mm thick. The mass fractions of each CNT and CNF based composites were 0.2%, 0.4%, 0.6%, 0.8% and 1% w/w and 5 replicates were made of each weight fraction, giving a total of 50 cylindrical samples. Briefly, PDMS base and cross-linker ratio of 10:1 was mixed thoroughly and the varying amount of CNF/CNT were added to separate mixtures. The mixture was subsequently dispersed under high shear mixing using an ultrasonication probe for 1 hour to ensure homogeneity of the slurries and to prevent the CNT/CNF from coagulating. The mixtures were then poured into cylindrical aluminum molds and degased in a vacuum oven for 1 hour to remove any air bubbles, before being cured at 100℃ for 2 hours. The final products obtained are shown in Figure 3.3.

Figure 3.3: Cylindrical samples of CNF/CNT-PDMS nanocomposites with varying mass fraction of fibers after curing.

The experiment can be divided into two parts. In Part One of the experiment, the apparent attenuation coefficient of each composite, $\beta_{composite}$, was measured using RF waveform obtained from ultrasonic testing. The ultrasonic measurement device used was the Epoch LTC: Rugged Handheld Flaw Detector (Olympus, Singapore). Briefly, the experimental setup consists of a sample of the composite submerged under water with a 2.25MHz transducer of 0.375in placed on top of it to ensure optimal conductivity (Figure 3.4). The ASTM Standard E664-93 (Bian 2003) was used for computing the apparent attenuation in the nanocomposites and is related by:

$$Apparent\ Attenuation, \beta(\frac{dB}{mm}) = \frac{20\times log_{10}(A_m/A_n)}{2\times(n-m)\times T} \quad (3.32)$$

where A_m and A_n indicate the amplitudes of the m^{th} and n^{th} back wall reflections, respectively, and T is the thickness of the sample. The sensitivity of the attenuation measurement was around 5%.

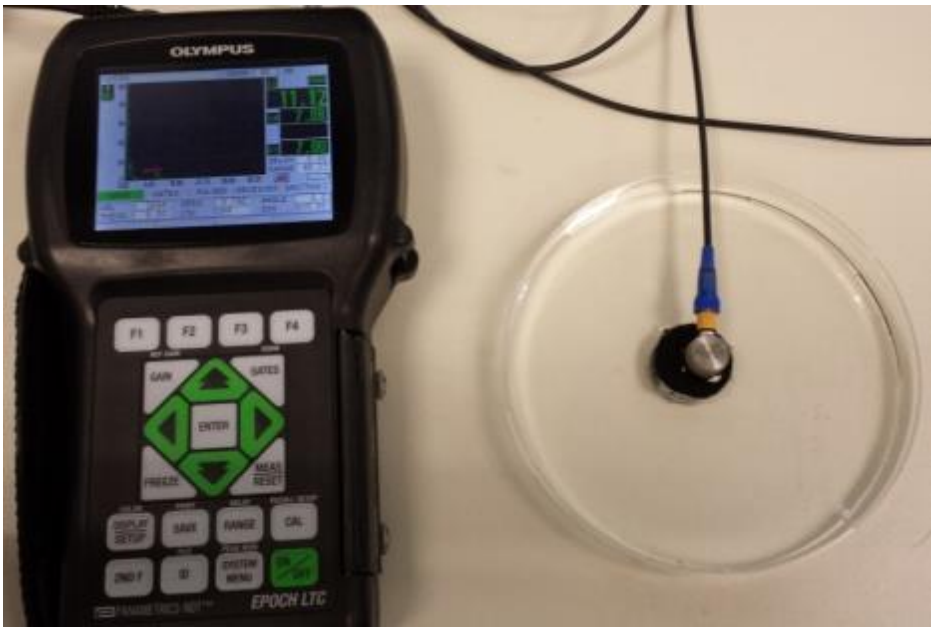

Figure 3.4: 2.25MHz transducer placed on top of submerged composite sample. RF waveforms readings can be collected from the Epoch LTC Handheld Flaw Detector device.

Part Two of the experiment involves the measurement of harmonic sound wave attenuation through the samples. Figure 3.5 depicts the experimental setup that was held

in an anechoic room. Each nanocomposite sample was placed in a double walled vacuum cylindrical container that was lined with an inner layer of sound absorbing material that was 15mm thick around the circumference and 80mm thick from the base of the container. The open end of the container was placed facing a loudspeaker that was positioned 1m away. Two condensers microphones were used to record the sound waves through the material. One was placed at the free open surface of the sample while the other was positioned at the interface between the sound absorbing material and the sample. Care was taken to ensure that the axes of the microphones were parallel to the axis of the loudspeaker. Similar microphones were used so that their pressure sensitivities were equal. The loudspeaker was connected to a computer with tone generator software installed. The frequency and amplitude of the harmonic sound waves generated by the speaker could be varied and controlled. To compute the attenuation through the material, the sound pressure measured by the microphone at the free surface was divided by the sound pressure from the inner microphone. Although diffraction of waves around the microphone may affect sensitivity at high frequencies, the experimental frequencies used were always much less than 10 kHz and direction of wave propagation was perpendicular to the axis of the microphone, thus the effect is negligible (Tarnow 1998).

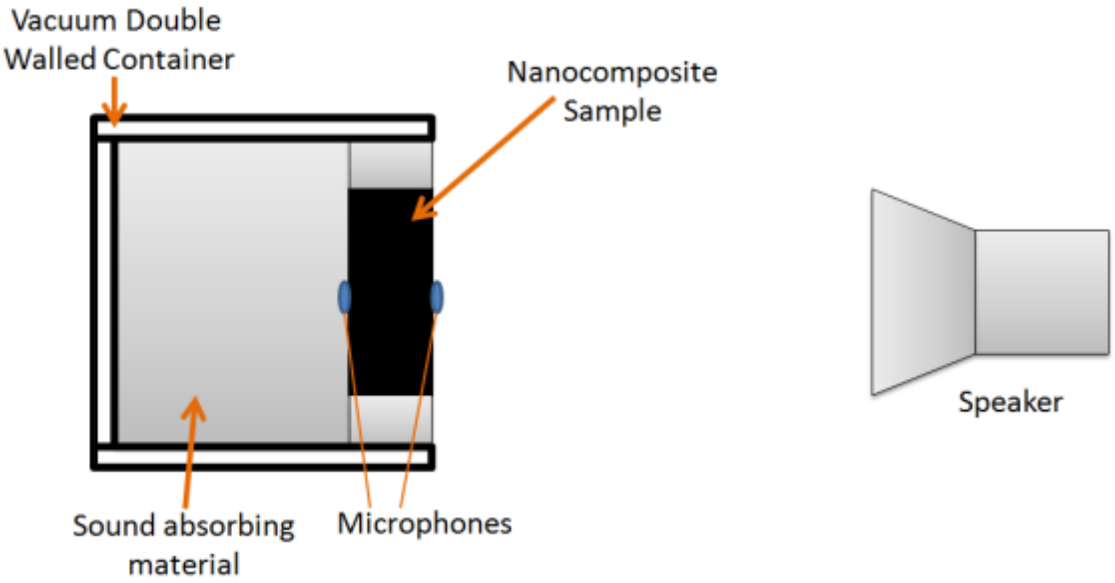

Figure 3.5: The sound attenuation measurement setup that was placed in an anechoic room. The sound input to the microphone was collected and used to compute the attenuation through the material.

3.3 Results

The results from the two experiments are presented in this section. In the first experiment involving ultrasonic attenuation measurements, the RF waveforms that is produced by the flaw detector (Figure 3.6) shows clearly the front wall, followed by the first and second back wall reflections in the sample. The gain in the equipment is set such that the first back wall reflection is always at 80% amplitude, in order to ensure that the signal does not saturate and at the same time yield quality images. The measured ultrasonic attenuation through the varying weight fractions of CNT/CNF composite samples were tabulated and plotted out (Figure 3.7 and 3.8).

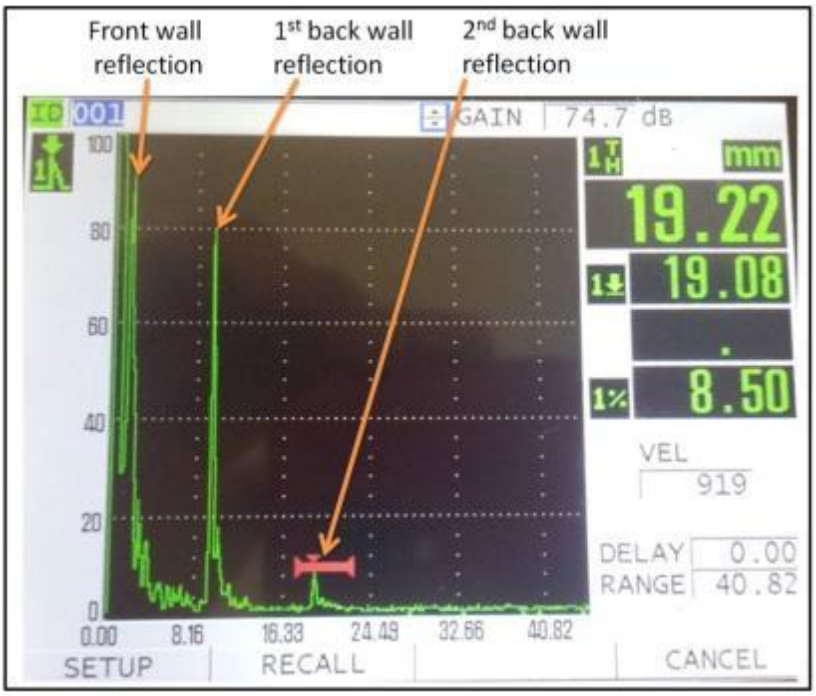

Figure 3.6: Amplitude versus distance plot of the nanocomposite sample shown in the flaw detector.

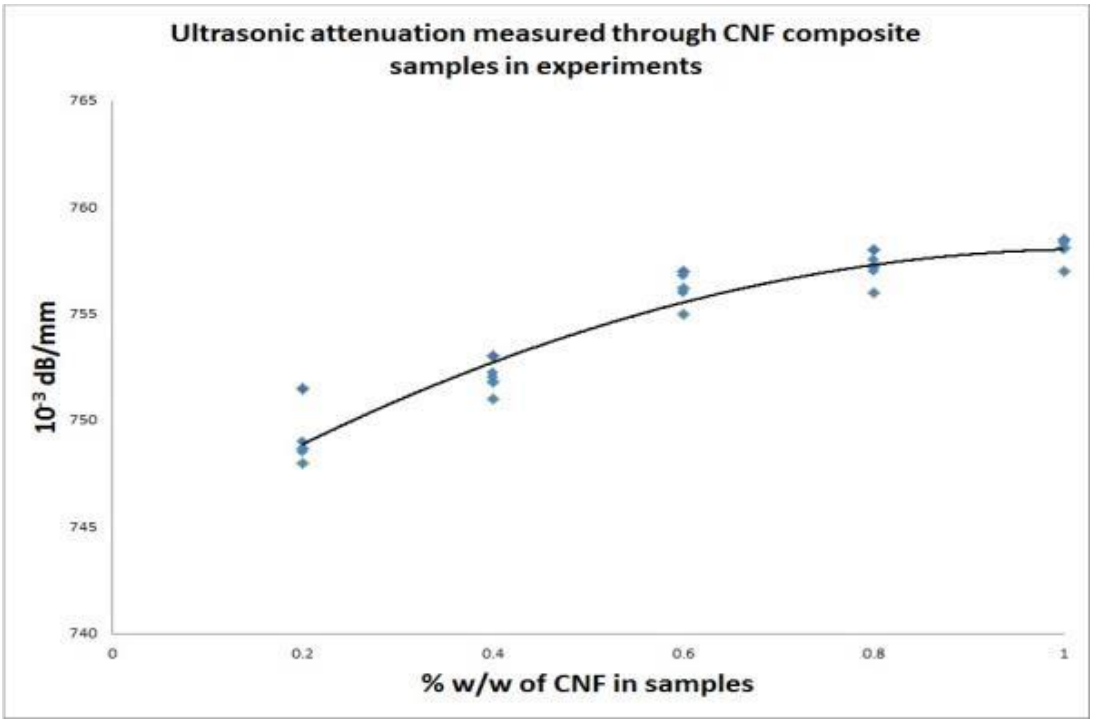

Figure 3.7: Ultrasonic attenuation measured in CNF-based composite samples of varying mass fractions of CNF.

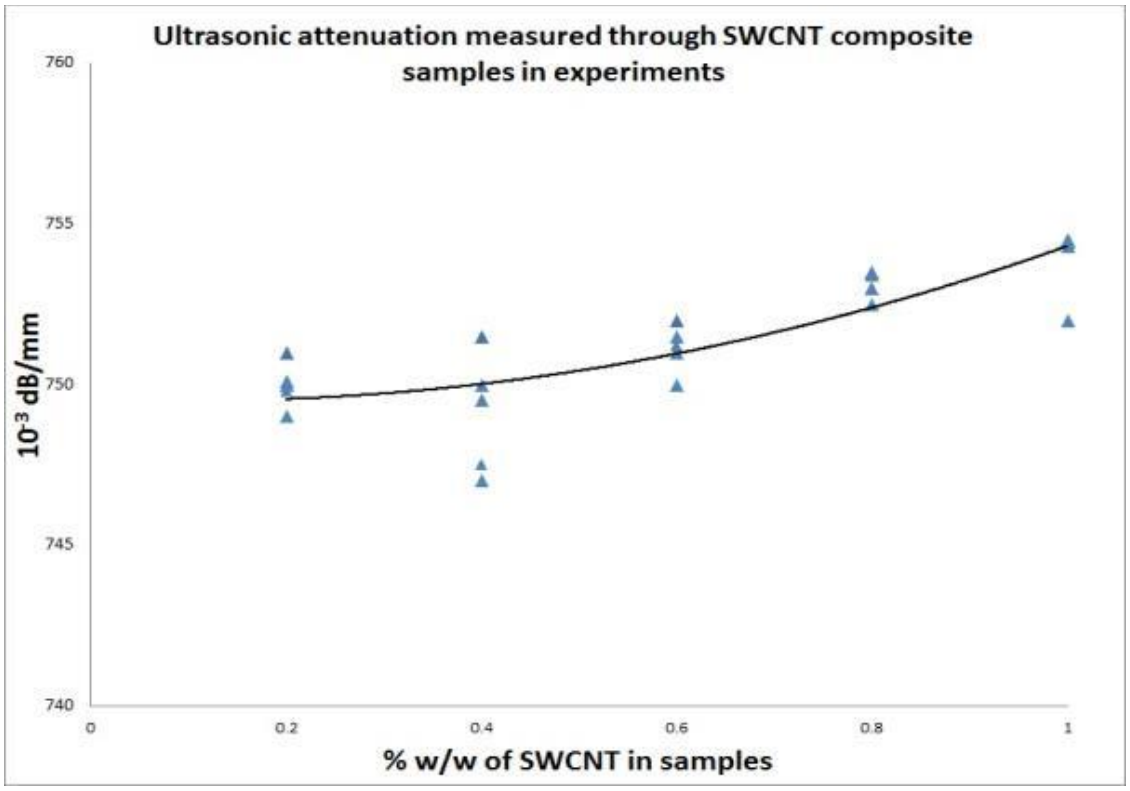

Figure 3.8: Ultrasonic attenuation in SWCNT-based composite samples of varying mass fractions of SWCNT.

For the second experiment, the experimentally measured harmonic sound waves attenuation through the samples at 200Hz and 1000Hz were tabulated and plotted for the varying weight percentage of carbon nano-inclusion in the composite samples (Figure 3.9 and 3.10).

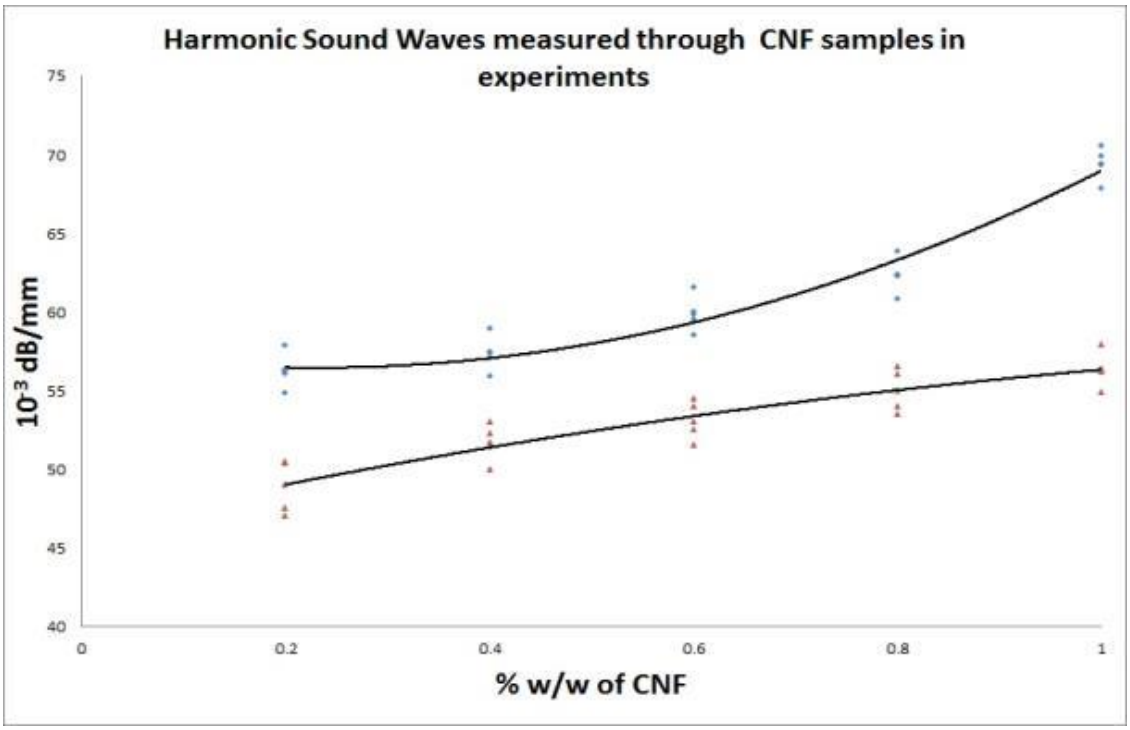

Figure 3.9: Sound attenuation measured in CNF samples of varying weight fractions at 200Hz (bottom) and 1000Hz (top).

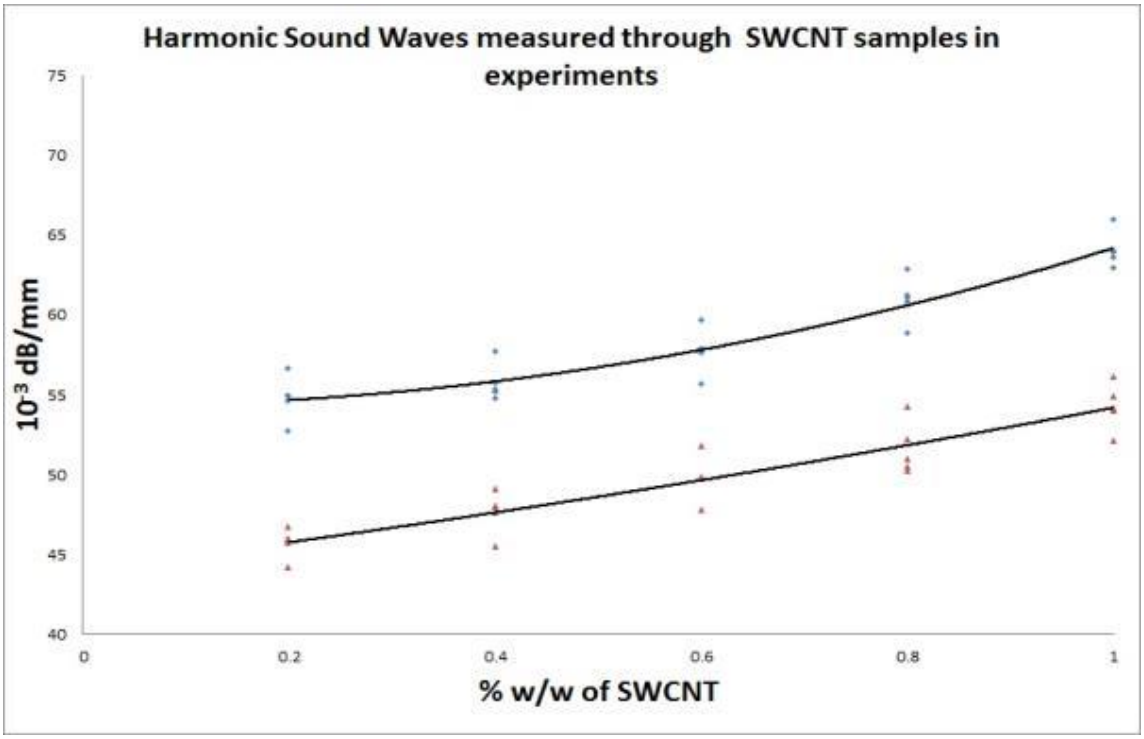

Figure 3.10: Sound attenuation measured in SWCNT samples of varying weight fractions at 200Hz (bottom) and 1000Hz (top).

3.4 Discussions

Figures 3.11 and 3.12 show the model and experimental results between the ultrasonic wave attenuation obtained from the model and experiment in CNF and CNT specimens, respectively. The error bars were computed based on the maximum and minimum values of the five replicated samples of each mass fraction of SWCNT and CNF composites. The apparent attenuations were obtained using ultrasonic waveforms of approximately 2.25MHz. Higher frequencies of 5MHz and above were not possible due to the limited and insignificant back wall echoes caused by the high attenuation rate of the nanocomposites. In Figures 3.13 and 3.14, harmonic sound wave attenuations from the proposed model and through experimental measurements are presented for each CNF and SWCNT samples. 200Hz and 1000Hz sound waves were used to demonstrate the increase in attenuation rate through the nanocomposites with increasing input wave frequencies. The rate of attenuation is also observed to be slightly lesser in SWCNT samples, compared to that of CNF samples for each mass fraction.

From both studies, a clear correlation between the experimental and theoretical model results is established for both CNF and SWCNT nanocomposite samples. However, slight variations between the experimental and model values were observed as well. In Figures 3.11 and 3.12, the predicted attenuation values deviate from the experimental results up to a magnitude of 5×10^{-3}dB/mm and are overall more than the mean experimental results. This can be attributed to the model's assumption that the planar area of the ultrasonic and harmonic sound waves travels through the sample without diverging and reflecting off the circumferential walls of the sample, which may result in interference. It is noticed that the discrepancies between experimental and theoretical results are much more

pronounced in high frequency ultrasonic waves (Figures 3.11 and 3.12) than in lower frequency harmonic waves (Figure 3.13 and 3.14), suggesting that the validity of the model decreases with increasing frequency of the propagating wave utilized. Another consideration for the discrepancies in results would be the purity of the SWCNT and CNF ($\geq$95% pure). The presence of other impurities in the sample might affect the accuracy of the experimental values. The limitations and future works on this study can be found in Chapter 7 of this thesis.

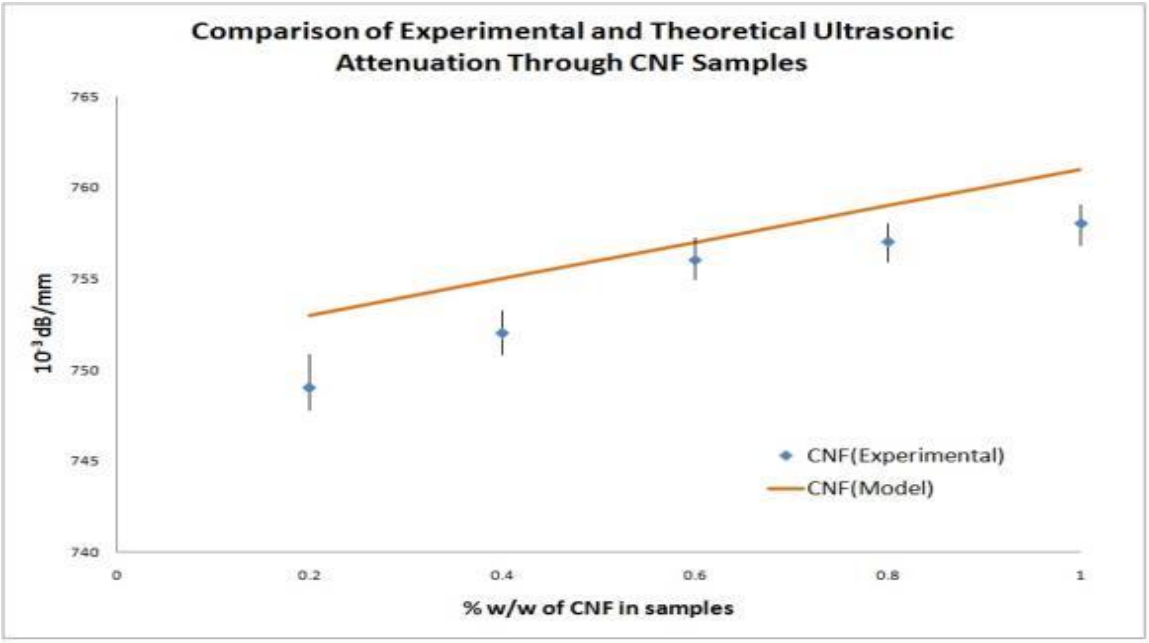

Figure 3.11: Graph comparing the results from measurement of experimental ultrasonic measurements through CNF samples and the proposed theoretical model.

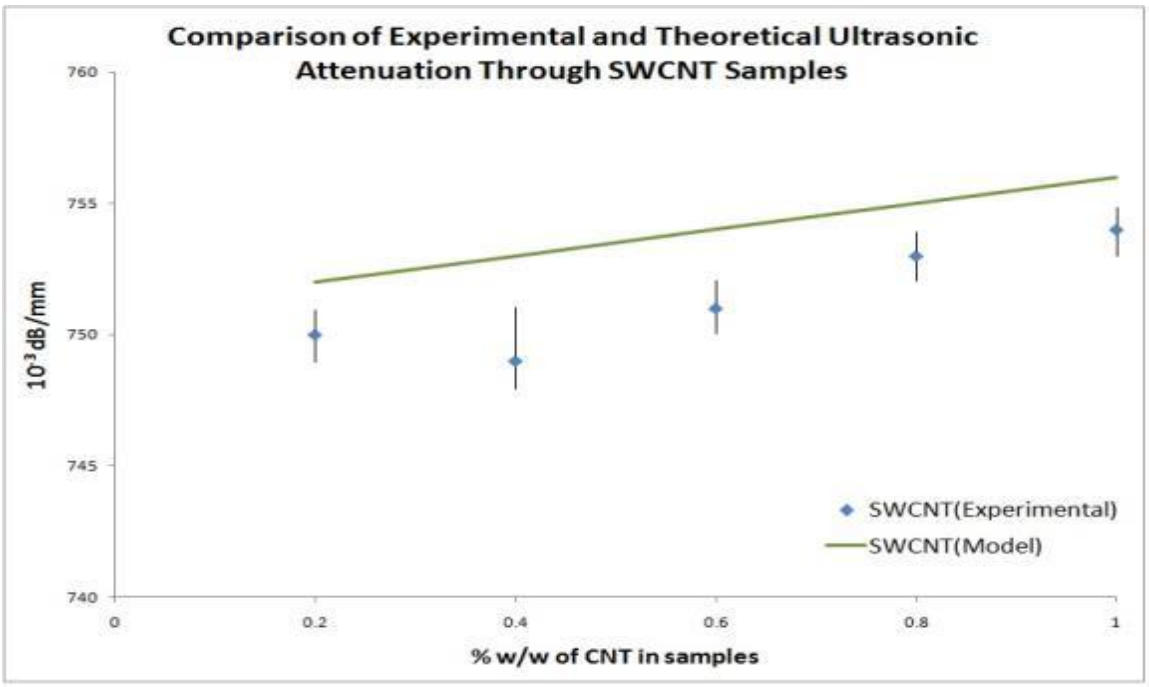

Figure 3.12: Graph comparing the results from measurement of experimental ultrasonic measurements through SWCNT samples and the proposed theoretical model.

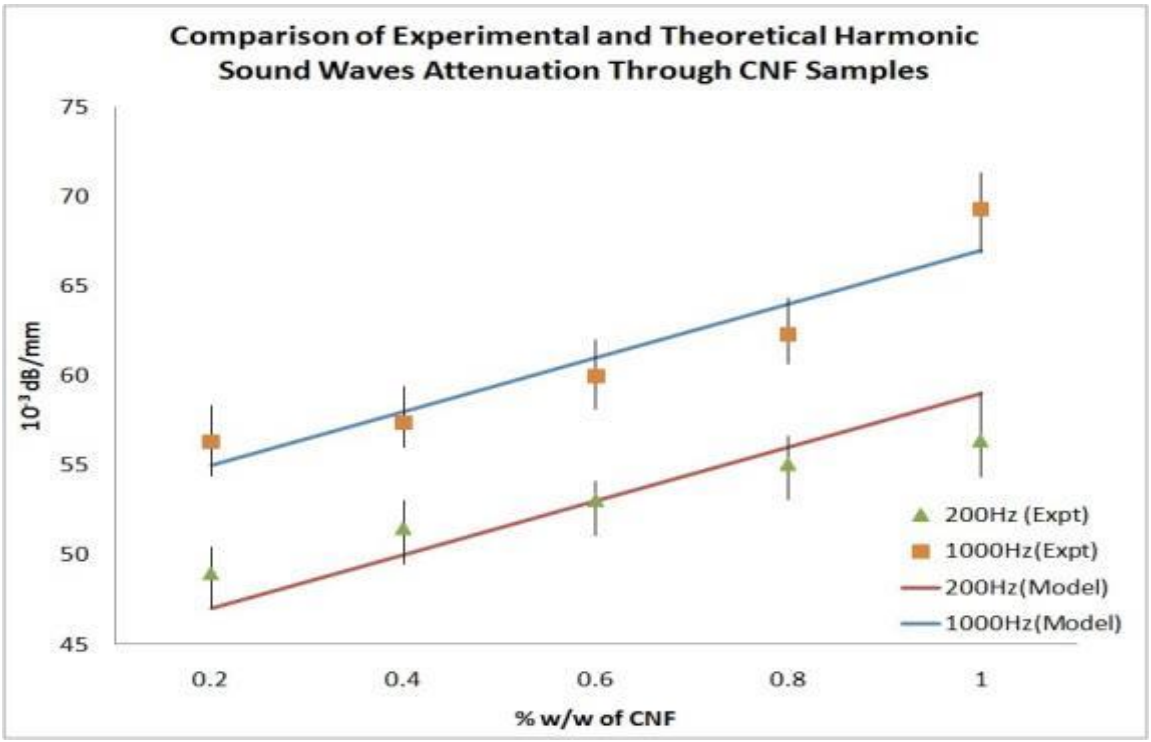

Figure 3.13: Graph comparing the results from measurement of experimental harmonic sound wave measurement of 200Hz and 1000Hz through CNF samples and the proposed theoretical model.

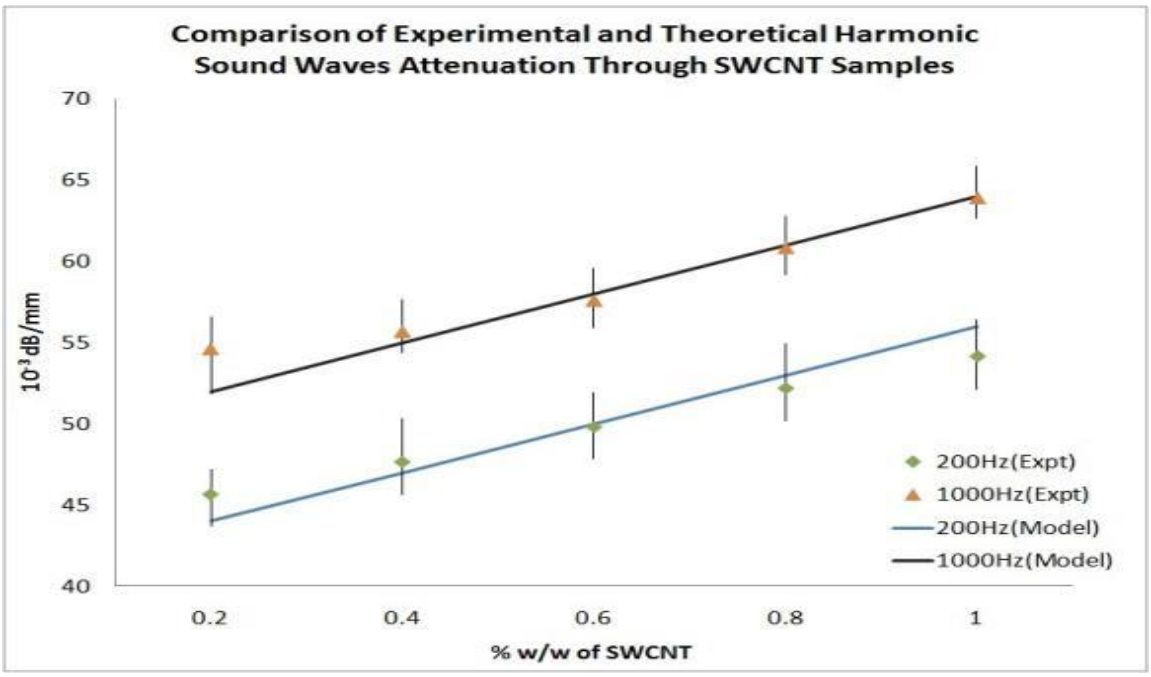

Figure 3.14: Graph comparing the results from measurement of experimental harmonic sound wave measurement of 200Hz and 1000Hz through SWCNT samples and the proposed theoretical model.

With the advancement of nanotechnology for the past few decades, new combinations and permutations of nanocomposites have been developed for a wide range of engineering applications. Nanocomposites have many superior physical properties, among which are damping and attenuation properties. A new method for prediction of attenuation in carbon-based nanocomposites (CNF-PDMS and SWCNT-PDMS) is proposed in this chapter. The model takes into consideration the dimensions and physical properties of the inclusions and matrix, as well as the properties of the incoming planar wave. Besides the Rayleigh scattering function of inclusions, the proposed model also incorporates the absorption of hollow air spaces and resonance of each CNF and SWCNT, and the interfacial friction between the inclusions and the matrix during vibration. The attenuation results from the model were then experimentally verified using an ultrasonic wave setup and a harmonic sound wave setup and were shown to be

consistent for both types of waves. The model can predict effectively at low weight fractions of inclusions.

Chapter 4

PROBABILISTIC PREDICTIVE MODELING OF CARBON NANOCOMPOSITES

Chua M, Chui CK (2015). Probabilistic Predictive Modeling of Carbon Nanocomposites for the Computer Aided Design of Medical Implants. *Journal of Mechanical Behavior of Biomedical Materials*. Doi: 10.1016/j.jmbbm.2015.01.013

This chapter presents work from the above paper published in 2015, which demonstrates the application of this model in the CAD of medical implants and finite element analysis for design evaluation and improvements. Section 4.1 introduces current material modeling and their application in engineering design. Section 4.2 proposes the probabilistic predictive model method while Section 4.3 presents the experimental and finite element validation. Section 4.4 discusses the application of the model in the design and evaluation of the tracheal implant design. Finally, Section 4.5 discusses and concludes the work.

4.1 Material Modeling for Engineering Design

The use of carbon nanotubes (CNT) in composites has a wide range of applications in the healthcare due to the many inherently unique properties that CNT possesses (Saito 2009). One such application is in dynamic load bearing implants in knee, hip and tracheal prostheses (Chua 2013, Lee 2011, Liu 2007). These however require the precise modeling of the mechanical properties of the implant in order to optimize its functions *in-*

vivo. Since it is difficult to deterministically quantify design outcome *in-vivo* due to variation in environmental and stress conditions, many CAD implant processes, mainly in orthopedics, have employed probabilistic approaches ranging from wear models to finite element simulations for evaluation and optimization (Kayabasi 2008, Layman 2010, Laz 2010, Pal 2008).

There is a need to model the mechanical properties of carbon nanocomposites accurately and efficiently for the CAD of medical implants. Constitutive models predict the mechanical properties of the nanocomposites based on input variables like inclusion aspect ratio, fiber weight fraction, Young's modulus of fibers and matrices and many more. However, it is difficult to obtain accurate results from these models due to uncertainties introduced into the variables like differences in fabrication techniques (Ma 2010), handling inconsistencies and differences in quality of different brands of reagents used.

We propose a probabilistic predictive model for the mechanical properties of the carbon nanocomposite implants based on initial loading data performed, and then demonstrate the application of the model in designing a medical implant.

4.2 Methods and Materials

4.2.1 Overview of Probabilistic Predictive Model

Initial tensile testing on 30 Carbon Nanotubes-Polydimethylsiloxane (CNT-PDMS) samples of three different CNT weight fractions was performed to obtain the scattered stress-strain curves. The experimental stresses at a certain inclusion weight fraction and strain were assumed to vary according to a normal distribution. These experimental data were then input into a modified Surface Response Method (RSM) that includes the non-

deterministic aspect of the stress results and utilizes Monte Carlo (MC) method to generate a predictive probabilistic polynomial equation. Experimental evaluation and FE simulation was then performed to validate the proposed method. The obtained results corresponded well with our model as they were within three standard deviation of the mean of the predictive model. Lastly, the probabilistic method was then applied to the CAD of trachea implants to model the mechanical property distribution of the design, which is useful for optimization and evaluation purposes.

4.2.2 Initial Loading Characterization

Stress-strain tensile stretching in the uniaxial direction of 30 CNT-PDMS nanocomposite samples of 3 varying mass fractions of CNT (0.25%, 0.5% and 0.75%) were performed *in-vitro.* Force displacement results were first measured during tensile loading using an Instron® 5543 precision instrument, which could support up to a load of ±1kN. The stress and strain mechanics in this study are represented using the Lagrangian system, whereby the stress is the load divided by the perpendicular cross sectional area of the sample in the stress-free state. The tensile strain is defined as the ratio of the length of the sample at a particular stress to the initial length at the stress-free state.

Multi-walled CNT (Sigma Aldrich, Singapore) of purity of greater than 98% were first immersed in concentrated nitric acid for 2 hours to functionalize and disperse the bundling, in order to reduce agglomeration when added into the matrix (Kwon & Kim, 2005). The solution was then drained and the CNT were rinsed with distilled water to remove any acidic residues and left overnight to dry in an oven at 80°C. Sylgard 184™ pre-polymer (Dow Corning, USA) was combined with its curing agent in a ratio of 10:1 and the various mass fraction of dried acid-treated CNT were added and dispersed

thoroughly to ensure homogeneity. Thirty aluminum molds of cavity dimensions 10mm by 10mm by 50mm were prepared. The CNT-PDMS mixtures were then carefully poured into their molds and placed in a vacuum oven for 1 hour to degas the mixture and remove any embedded air bubbles that might affect the mechanical properties of the composite. The parts were then cured at 120°C for 4 hours and removed thereafter. Microscopic images (X160) of a thin section of each sample type are shown in Figure 4.1.

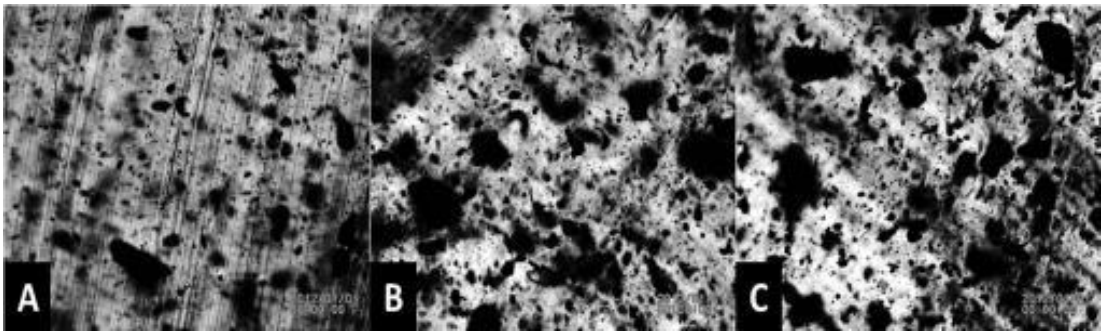

Figure 4.1: Microscope imaging (X160) of CNT-PDMS samples of mass fraction (A) 0.25%, (B) 0.5% and (C) 0.75%.

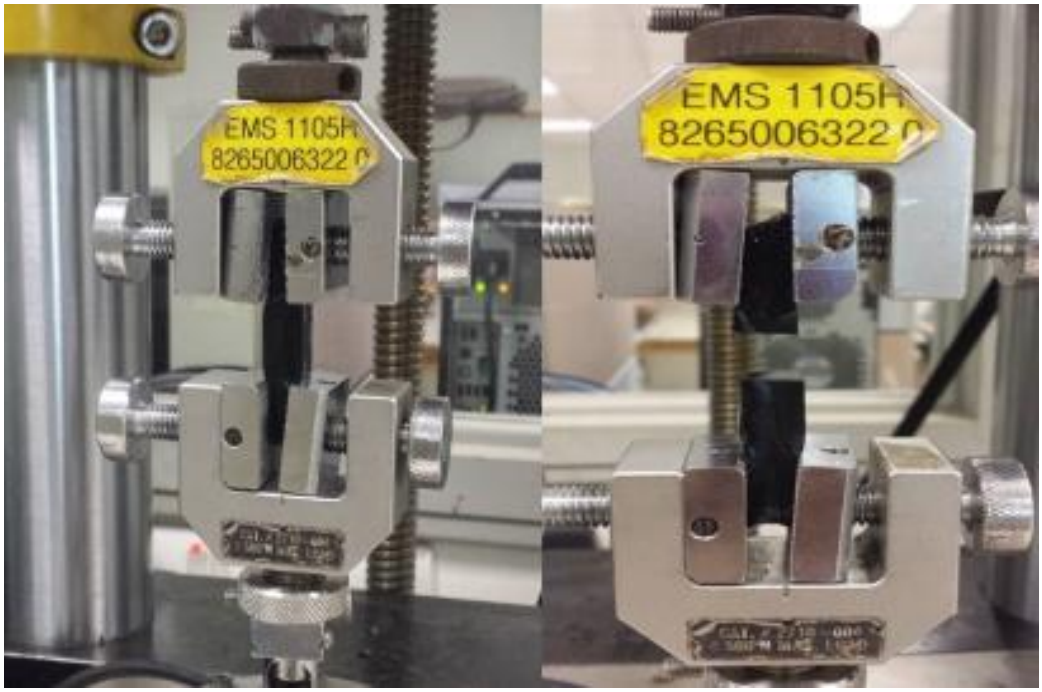

Figure 4.2: Experimental tensile testing of CNT-PDMS samples. Test samples at the (left) start and (right) fracture point.

All 30 samples were subjected to tensile testing till fracture at room temperature (Figure 4.2). The standardized gauge length used was 20mm and the force versus displacement data were logged with a cross head speed of 50mm/min.

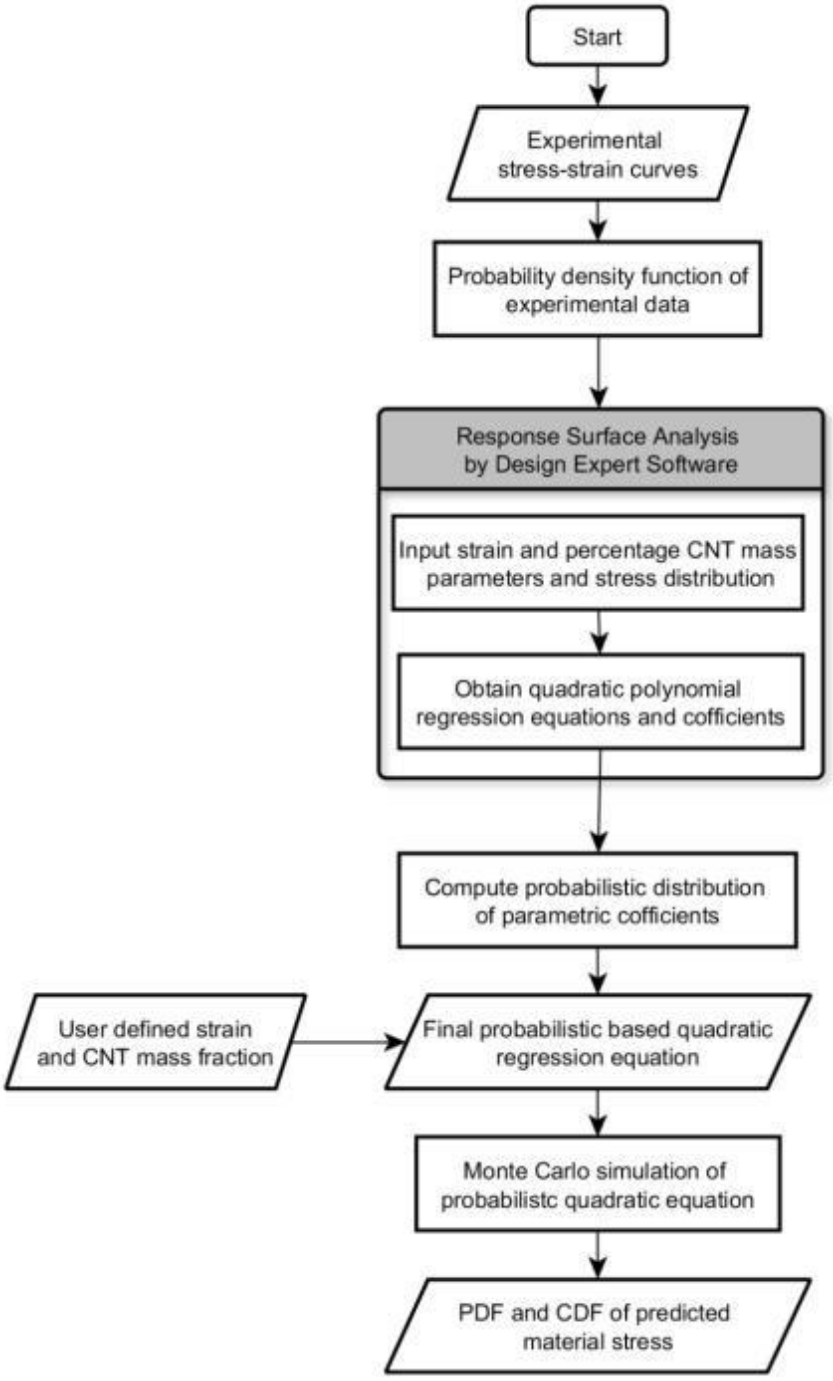

Figure 4.3: Proposed modified probabilistic response surface based flow process.

4.2.3 Probabilistic Surface Response Approach

Accurate prediction of the final stress-strain curve behavior in nanocomposites, due to changes in composition and/or fabrication variables, is crucial for medical implant design processes (Chua 2014). The mechanical outcome for a certain set of parameters is usually not a specific value but exists in a probabilistic distribution (Fu 2013). A modified probabilistic surface response approach can be used as a predictive model to generate the stress-strain distribution of carbon nanocomposites at various weight fraction of inclusion (Figure 4.3). Application of classical surface response method was described in (Cho 2011) for the optimization of a foaming jig reinforcement structure.

The Central Composite Design, based on the surface response method (Leardi 2009, Rostamiyan 2011), is the core algorithm utilized in this work that allows for the computation of the constant, linear terms, quadratic terms and the interaction coefficient between the variables. The general equation for two variables base is as follows:

$$Y_i = \beta_0 + \sum_{i=1}^{2} \beta_i x_i + \sum_{i=1}^{2} \beta_{ii} x_i^2 + \sum_{i,j=1}^{2} \beta_{ij} x_i x_j, \quad (4.1)$$

where Y_i is the predicted response, x_i and x_j are the coded input variables, β_0 is the intercept term, β_i is the linear effects, β_{ii} is the squared effect, and β_{ij} is the interaction term. The input variables were coded according to the following equation:

$$x_i = \frac{(X_i - X_0)}{\Delta x}, \quad (4.2)$$

where x_i is the coded value of the *i*th independent variable, X_i is the natural value of the *i*th independent variable, X_0 is the center point value and ΔX is the step change value. However, the mechanical outcome of the final predicted nanocomposite, based on user defined input variables, exists as a probabilistic distribution (which in this case, a normal

distribution assumption is made). As such, the coefficient of the constant, linear quadratic and interaction terms of the equation may be modified as distributions:

$$Y_i \sim N(\mu_Y, \sigma_Y) = \beta_0 \sim N(\mu_{\beta 0}, \sigma_{\beta 0}) + \sum_{i=1}^{2} \beta_i \sim N(\mu_{\beta i}, \sigma_{\beta i}) x_i + \sum_{i=1}^{2} \beta_{ii} \sim N(\mu_{\beta ii}, \sigma_{\beta ii}) x_i^2 + \sum_{i,j=1}^{2} \beta_{ij} \sim N(\mu_{\beta ij}, \sigma_{\beta ij}) x_i x_j, \quad (4.3)$$

where $N(\mu_a,\sigma_a)$ indicates the normal distribution that a coefficient term, a, varies according to a mean of μ_a and standard deviation of σ_a.

4.2.4 Experimental Validation

Experimental validation was performed to access the accuracy of the generated predictive polynomial equation and to verify the feasibility of the proposed algorithm. The 3 sigma rule of a normal distribution states that 68% of the values should lie within one standard deviation away from the mean while about 95% and 99.7% of the values lies within two and three standard deviation, respectively (Pukelsheim 1994). Therefore, evaluation of the proposed methodology via 3 sigma rule was done.

Ten new CNT-PDMS samples of 1% w/w CNT were fabricated according to the method described earlier. The new samples were then subjected to similar tensile testing and the stress-strain results were tabulated and compared with the predicted results from Equation (4.3).

4.2.5 Finite Element (FE) Validation

We further validate the accuracy of the probabilistic predictive model method and results using FE analysis. The geometry of the sample was modeled and its material

represented by a 2-constant Mooney-Rivlin material model (Boyce 2000, Huang 2008, Wang 2004) in COMSOL Multiphysics® software:

$$W = C_1(\bar{I}_1 - 3) + C_2(\bar{I}_2 - 3), \quad (4.4)$$

where W is the strain energy function, C_1 and C_2 are the material parameters, $\bar{I}_1$ and $\bar{I}_2$ are the strain invariants. The material parameters were determined using curve fitting tool which fits the stress-strain curve of the hyperelastic model to the mean stress-strain results from the proposed probabilistic model. The Levenberg-Marquardt (LM) optimization algorithm (Brown 1971, Moré 1978) was utilized to minimize the error between the simulated stress values and the corresponding predicted stress values. Objective function of the optimization algorithm was as follows:

$$R(C) = \sum_{i=1}^{n}\left(S^i_{predicted} - S^i_{sim}\right)^2, \quad (4.5)$$

where C is the material parameter vector, n is the number of sampled data, while $S^i_{predicted}$ and S^i_{sim} are the predicted stress and simulated stress, respectively.

4.3 Results

4.3.1 Initial Material Characterization

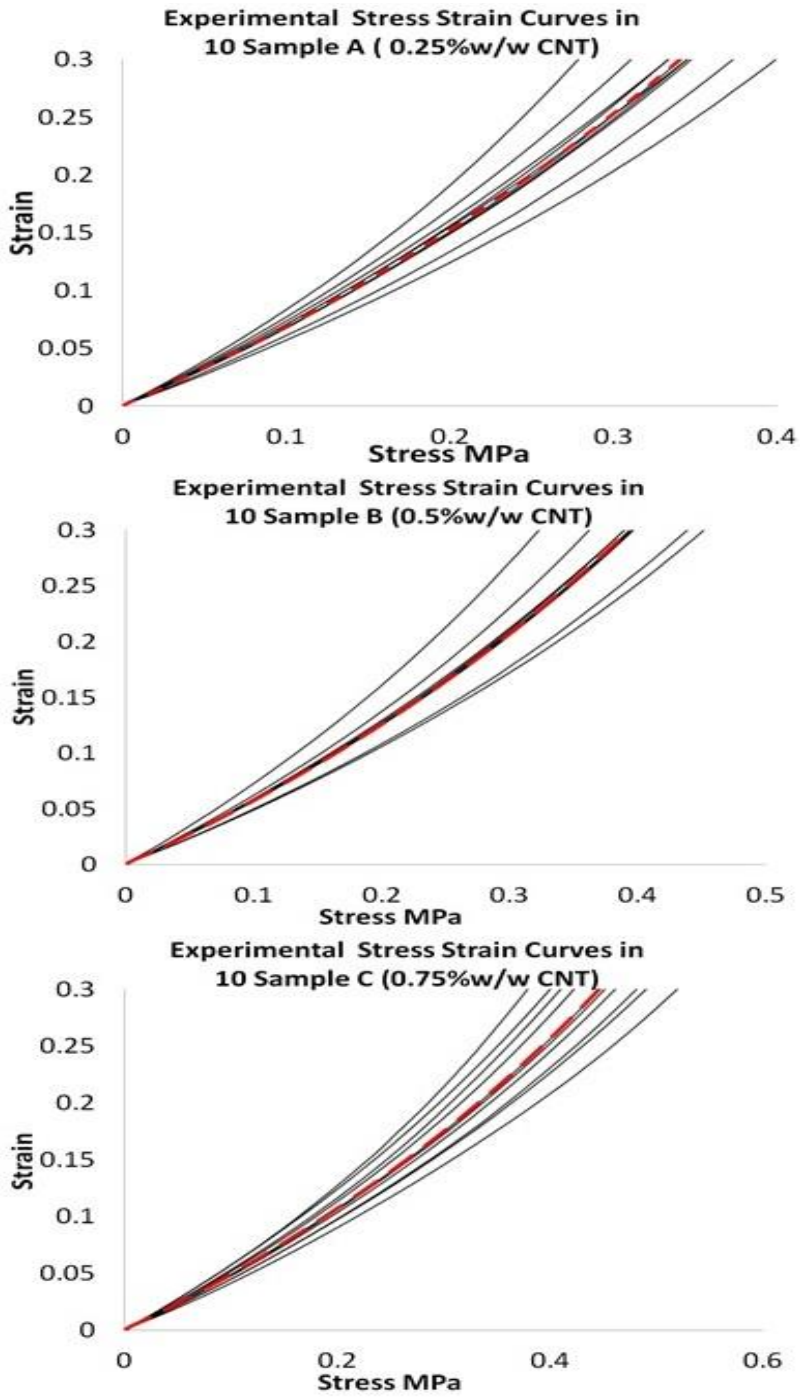

Figure 4.4: Experimental stress-strain results. Black solid lines indicate results of the 10 samples while red dashed lines indicate the mean result.

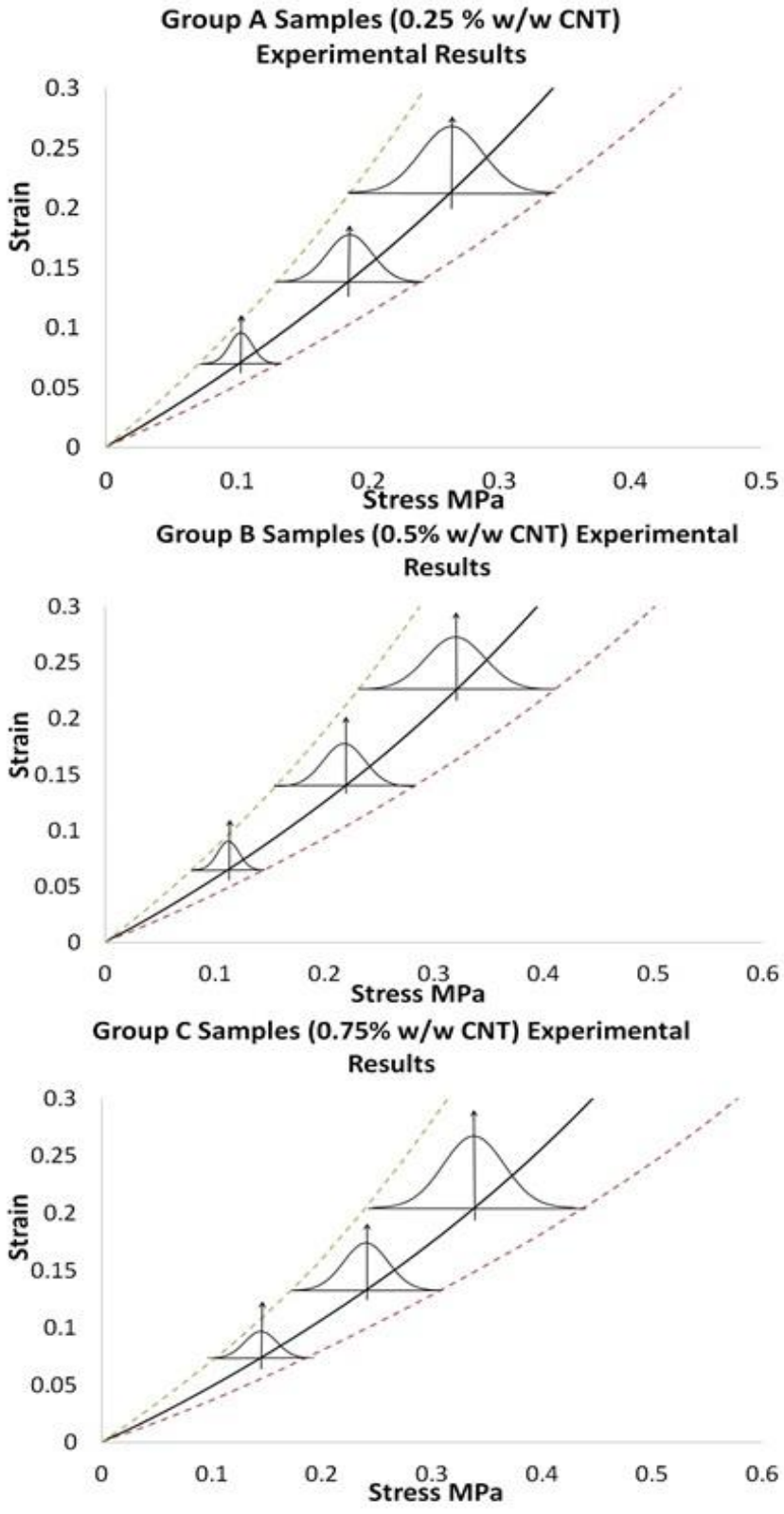

Figure 4.5: Stress-strain from uniaxial tensile measurements. Centre black line is the mean while 6-sigma normal distribution of stress values are represented by the horizontal bars.

In the initial loading tests for the varying weight percentage of nancomposites, strain-strain results were computed from the acquired force-displacement data and plotted individually according to their CNT mass fractions (Figure 4.4). The experimental stress results for strain are modeled according to a normal distribution as shown in Figure 4.5. The mean and standard deviation of the distribution are computed as follow:

$$\mu_\sigma = \frac{1}{N}\sum_{i=1}^{N} \sigma_i, \tag{4.6}$$

$$S.D_\sigma = \sqrt{\frac{1}{N}\sum_{i=1}^{N}(\sigma_i - \mu_\sigma)^2}, \tag{4.7}$$

where μ_σ is the mean stress, σ_i is the experimental stress value of a sample, $S.D_\sigma$ is the standard deviation of stresses and N is the number of sample in the group.

4.3.2 Probabilistic Surface Response

Using Equations (4.1), (4.2) and (4.3), the regression equation was computed and Table 4.1 presents the levels of variables (CNT weight fraction and tensile strain) used while Table 4.2 shows the corresponding experimental stress distribution values for each combination of variable input.

Computation of the surface response quadratic equation was performed with 1,000 runs of Monte Carlo simulation. The Monte Carlo method is one of the widely utilized sampling based algorithms, which relies on repeated random sampling to compute results (Halpin 1972, Hastings 1970, Hukushima 1996, Robert 1999). They are useful in scenarios whereby it is infeasible to calculate an exact result due to the probabilistic nature of the problem. Each run of Monte Carlo generates the ten random stress values based on the mean and standard deviation of the computed normal distributions shown in Table 4.2. These values are then used to generate the surface response quadratic

polynomial equations, which are collated and the overall mean and standard deviation of the coefficients were observed to follow a standard deviation and are presented in Table 4.3. Hence the final generated coded predictive quadratic polynomial can be written as:

$$\begin{aligned} Tensile\ Stress\ (MPa) = {} & [\beta_0 \sim N(0.293, 7.5 \times 10^{-2})] + \\ & [\beta_1 \sim N(3.83 \times 10^{-2}, 1.15 \times 10^{-2})]x_1 + \\ & [\beta_2 \sim N(0.117, 3.46 \times 10^{-2})]x_2 + \\ & [\beta_{12} \sim N(1.34 \times 10^{-2}, 7.45 \times 10^{-3})]x_1 x_2 + \\ & [\beta_{11} \sim N(-6.11 \times 10^{-5}, 4.63 \times 10^{-3})]x_1^2 + \\ & [\beta_{22} \sim N(-1.27 \times 10^{-2}, 1.53 \times 10^{-3})]x_2^2. \end{aligned} \quad (4.8)$$

TABLE 4.1
Coded and non-coded values of variables used

Variables	Range and levels		
	-1	0	1
X_1: CNT mass fraction (%)	25	50	75
X_2: Strain	0.1	0.2	0.3

TABLE 4.2
Experimental Matrix

No.	X_1	X_2	MWCNT weight fraction	Strain	Mean Stress (MPa)	Standard Deviation Stress (MPa)
1	-1	-1	0.25%	0.1	0.141	0.013
2	-1	0	0.25%	0.2	0.253	0.023
3	-1	+1	0.25%	0.3	0.345	0.031
4	0	-1	0.5%	0.1	0.165	0.014
5	0	0	0.5%	0.2	0.293	0.024
6	0	+1	0.5%	0.3	0.396	0.037
7	+1	-1	0.75%	0.1	0.188	0.016
8	+1	0	0.75%	0.2	0.0333	0.03
9	+1	+1	0.75%	0.3	0.446	0.044
10	0	0	0.5%	0.2	0.293	0.024

TABLE 4.3
Coefficient Derived from Monte Carlo Method

Coefficients	β_0	β_1	β_2	β_{12}	β_{11}	β_{22}
Mean	0.293	3.83×10^{-2}	0.117	1.34×10^{-2}	-6.11×10^{-5}	-1.27×10^{-2}
S.D	7.5×10^{-2}	1.15×10^{-2}	3.46×10^{-2}	7.45×10^{-3}	4.63×10^{-3}	1.53×10^{-3}

4.3.3 Experimental Validation

Results from the experimentally measured loading data of the Sample D (1% w/w CNT) were compared with the theoretically predicted results from the proposed model and are presented in Figure 4.6 and 4.7. From the results, it may be observed that the experimental stress-stain curves of the new tests lies within 3 standard deviations from the predicted mean (μ-3σ, μ+3σ). The experimental mean and the cumulative density function (CDF) at 3 different strains are also closely related to the predictive model. The experiment has successfully validated the proposed predictive model and has demonstrated that it could be used to predict stress at pre-defined variable inputs.

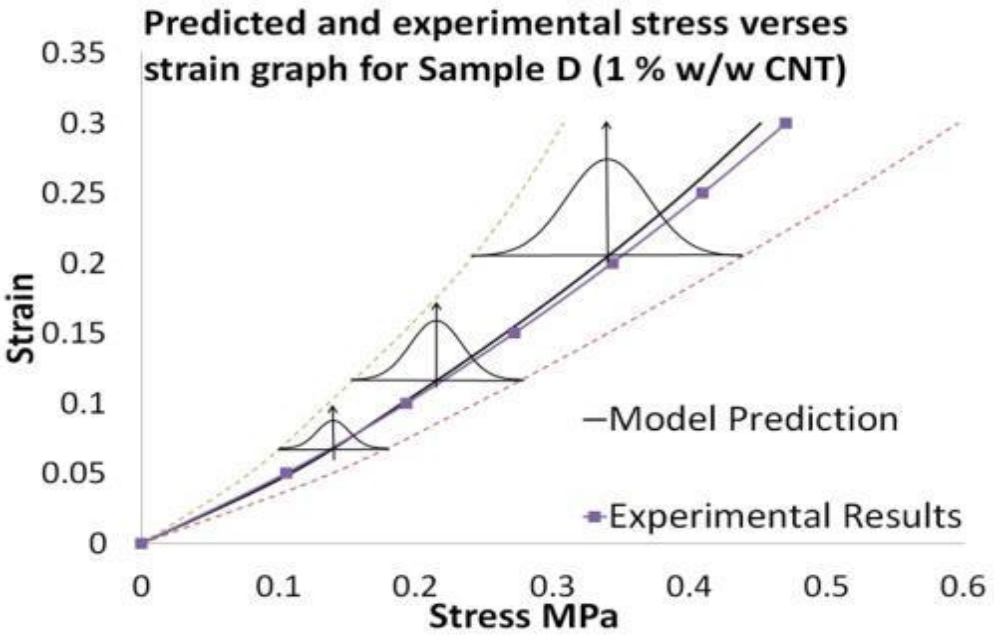

Figure 4.6: Stress-strain graphs from uniaxial tensile measurement on Sample D (0.5% w/w CNT). Centre black line is the mean predicted stress values and the 6-sigma normal distribution are represented by the horizonal bars. The mean of experimental results is represented by the line with square markers.

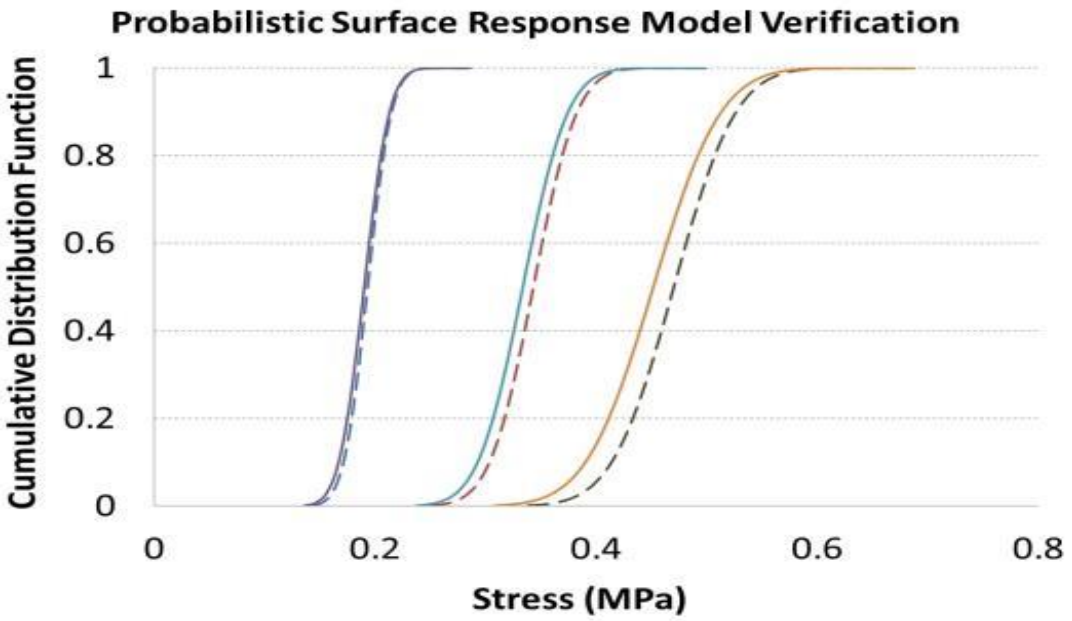

Figure 4.7: CDF of stress values at three different strains for 1 % w/w CNT. Strain of curves from left to right: 0.1, 0.2 and 0.3. Solid lines represent the predictive model results while dashed lines indicate experimental results.

4.3.4 Finite Element Validation

The values of C_{10} and C_{01} obtained from the curve fitting of the material parameter data to the 1% w/w CNT predicted model was 0.1512MPa and 0.2165MPa, with a root-mean-square-error (RMSE) of 0.00328MPa. A 3D model of the test sample was imported into COMSOL Multiphysics® for finite element analysis with the prescribed material parameters and the assumption of the solid being fully incompressible (Figure 4.8). The boundary conditions utilized were the equal and opposite displacements of the two square faces for strains up to 0.3. Figure 4.9 presents the predicted, simulated and experimental stress curves. It was observed that the simulated stress-strain curve falls within 3 standard deviation of the mean of the predictive model. This verifies the accuracy of the predictive model by demonstrating that its results are consistent with both experimental and FE simulation data.

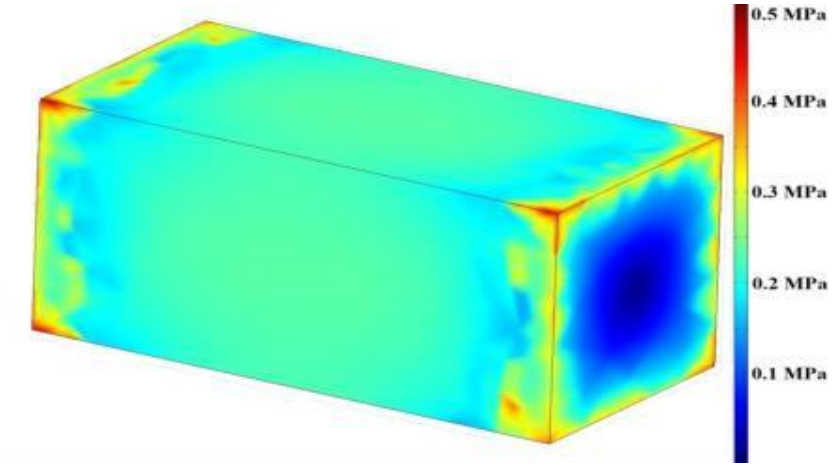

Figure 4.8: Simulation of tensile test on CNT-PDMS sample. The color bar indicates the intensity of the stress concentrations experienced by the body.

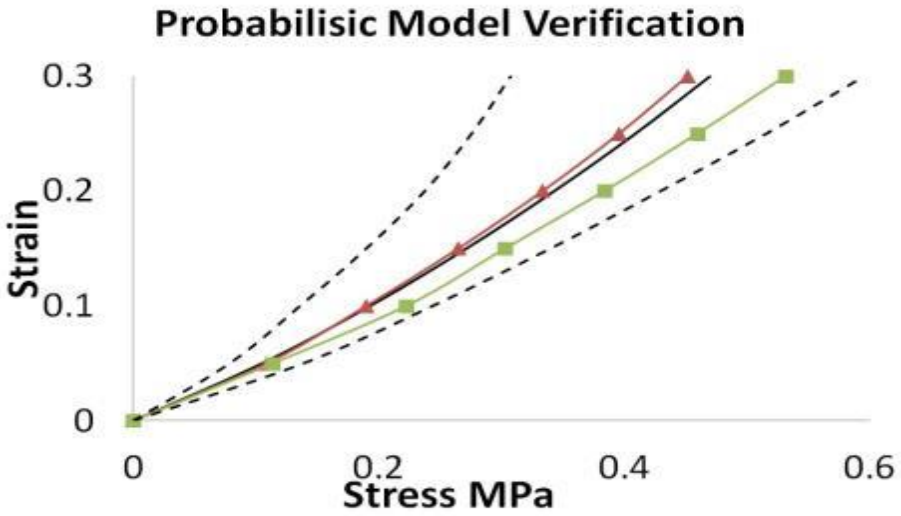

Figure 4.9: Stress strain curves of predicted, simulation and experimental results for 1% w/w CNT. Black solid line and dotted lines represents the predicted mean results and the ±3 standard deviations limit, respectively. Line with square markers indicates the simulation results while line with triangular markers refers to the experimental results.

4.4 Design of Tracheal Implant

The probabilistic predictive model presented in this chapter can be integrated into the CAD and development of medical implants for optimization. We have been experimenting novel carbon nanocomposite implants for airway restoration in severe trachea carcinoma cases (Chua 2013). Iterative FEA simulation of the implant model is

imperative for the evaluation and improvement of the design. Very often, the parametric input into the material model for simulation is deterministic, which produces a single outcome value. However in practice, this may not be sufficient in design applications since the mechanical properties of fabricated implants often display a range of values due to minor inconsistencies in the handling and fabrication process. Therefore, this probabilistic predictive model may be applied with FEA of CAD implants to acquire a probabilistic range of results.

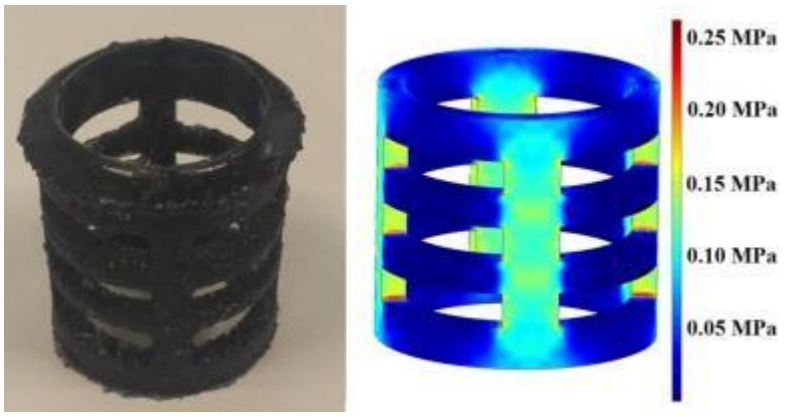

Figure 4.10: Finite element analysis of tracheal implant. (Left) Fabricated carbon nanocomposite implant and (Right) implant model under tensile stress analysis. The color bar denotes the stress concentration in the implant, which is observed to be the largest along the vertical columns.

To demonstrate the application of the probabilistic algorithm in the CAD and simulation of medical implants, a 3D tracheal implant (length 30 mm, outer diameter 33 mm and inner diameter 27 mm) was first modeled. Following which, Money Rivlin parametric distribution (C_{10}: mean = 0.1512MPa, S.D = 0.0424MPa; C_{01}: mean = 0.2165MPa, S.D = 0.0119MPa) for 1% w/w CNT composite material was computed using the predictive model presented in the previous section. One thousand runs of FEA of the designed implant (Figure 4.10) were performed with each run utilizing random

parametric values within the stated normal distribution range. The results were tabulated and plotted as shown in Figure 4.11. The normal human trachea undergoes up to 20% tensile strain in daily motion due to swallowing (Jungebluth 2014). In Figure 4.11, the predicted stress at +3σ above the mean stress at strain value of 0.2 is 1MPa, indicating it is significantly lower than the experimentally determined yield stress of the material used which is 20MPa, hence the design has a safety factor of 20. Besides tension, other forms of characteristics may be evaluated and optimized in future studies like rotation, compression, bending and the flexibility of the artificial trachea to mimic the behavior of the natural tissue. Hence, the feasibility of integrating the probabilistic model into CAD of medical implant has been shown through this application. The merits of such a method would be the generation of a probabilistic range of mechanical behavior of the design for improvements and better in-vivo performance.

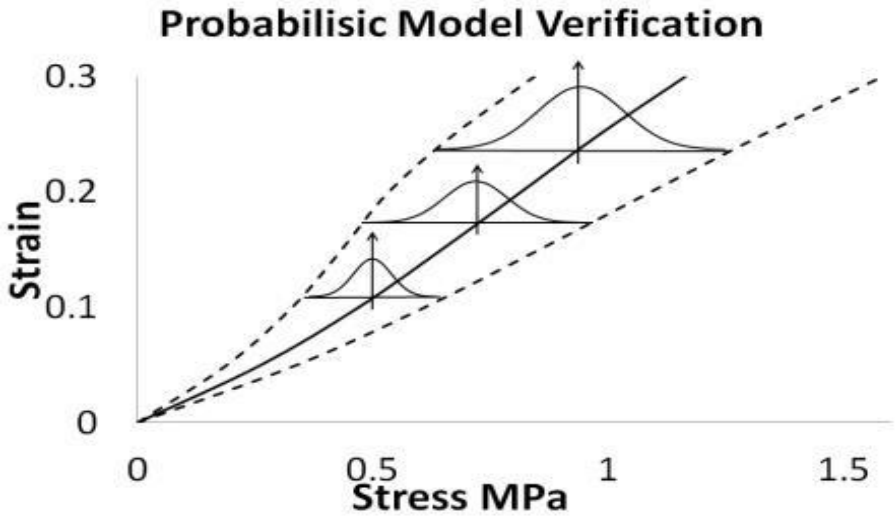

Figure 4.11: Stress-strain graphs from uniaxial tension FEA on tracheal implant model. Centre black line is the mean stress and the 6-sigma normal distributions are represented by the horizonal bars.

4.5 Discussions

The proposed probabilistic algorithm has been validated by both FE simulation and experimental results and was shown to be able to successfully predict the probability density stress-strain behavior of the material based on the input variables. This method has also eliminated the uncertainty errors of discrepancies in handling of materials, fabrication conditions and reagent properties that are present in other constitutive models, like the mean field approach (Halpin 1972) or the mechanical percolation model (Shanmuganathan 2010), by modeling according to initial experimental samples. Furthermore, this algorithm may be modified to include other input variables like curing duration, temperature and acid treatment duration to predict other physical properties like thermal coefficient, attenuation and degradation rates for a wide range of CAD and applications.

The FE validation using Mooney Rivlin model coefficients derived from the predicted stress-strain curve results has displayed good consistency with the latter. This indicates the possibility of having FE simulation of multiple models of different intricate geometries based on the predictive equation developed from an initial modular geometry. A 2-constant Mooney Rivlin hyperelastic model was used in this FE validation study to represent the carbon nanocomposite sample as it was sufficient to model the predicted stress-strain curve. Other material constitutive models (Chui 2004, Chui 2007) and viscoelastic models (Yang 2011) may be readily utilized in the proposed FE simulation to predict the mechanical behavior of the materials. As described in Section 4.4, the predictive model was applied to the CAD of a tracheal implant, which generated a stress

distribution curve that can be useful for safety evaluation and further optimization. The application of this predictive model is not limited to the CAD of medical implants.

This chapter has introduced and verified a new modified probabilistic-based surface response algorithm as a predictive model to estimate carbon nanocomposite mechanical behavior under tension for device design. The model utilized initial experimental stress-strain data and composition to generate a probabilistic polynomial regression equation that allows user-defined variable inputs to determine the range of mechanical outcome. This algorithm allows for timely and accurate modeling of the mechanical stress in the carbon nanocomposites that can be used for medical implant design and FE optimization processes. The development of such methodology is useful for the CAD of patient-specific ENT implants to improve the quality of healthcare (Chua 2013).

Chapter 5

CARBON NANOCOMPOSITE TRACHEAL PROSTHESIS

Chua M, Chui CK, Chng CB, Lau D (2013). Carbon Nanotube-Based Artificial Tracheal Prosthesis: Carbon nanocomposite implants for patient-specific ENT care. *Nanotechnology Magazine, IEEE, 7*(4), 27-31. Doi: 10.1109/mnano.2013.2289691

Chua M, Chui CK, Teo C, Lau D (2014). Patient Specific Carbon Nanocomposite Tracheal Prosthesis. *International Journal of Artificial Organs. D*oi: 10.5301/ijao.5000374

This chapter contains work from the above two articles which were published in 2013 and 2014, respectively. It describes the development of a patient-specific artificial trachea made of Carbon Nanotubes and Poly-di-methyl-siloxane (CNT-PDMS) composite material. Section 5.1 describes the current types of tracheal replacements and their limitations. Section 5.2 contains the development and simulation study of the developed patient-specific tracheal prosthesis. Section 5.3 presents the *in-vitro* and *in-vivo* experiments while the final section discusses the chapter.

5.1 Tracheal Replacements

According to the National Cancer Institute, the rate of tracheal cancer in the United States is 228,190 annually. Stenosis caused by the tumor growth in the trachea may be treated and controlled with radiation or stenting (Mornex 1998, Wallace 1986), but the current gold standard for treating severe tracheal carcinoma is by surgically removing the affected portion and joining the remaining ends via anastomosis. For surgical removal, trachea resection length of 6cm or more requires a replacement graft due to anastomotic

tension (Macchiarini 2008). There are current technologies for airway reconstruction, including autografts, allografts and synthetic grafts (Kucera 2007, Shi 2005).

Materials used in airway replacement should have the basic requirements of biocompatibility, non-immunogenicity and non-toxicity (Grillo 2002). Next, the graft needs to provide sufficient mechanical strength to resist collapse from lateral compressive stresses while possessing a certain degree of flexibility for bending, rotation and stretching due to head and neck motions (Baiguera 2010). Quick vascularization of the device is also essential in order to support the epithelium migration into the lumen (Doss 2007). Studies have suggested that epithelialization of the lumen affects patency rates as it facilitates mucous removal and reduce instances of stenosis caused by excessive granulation tissue growth (Doss 2007, Grillo 2002). Similarity in dimensions of the graft to the native trachea also contributes to the long term success and integration of the reconstructed airway.

Autografts such as the aorta, pericardium or esophagus have been experimented with in tracheal reconstruction (Azorin 2006, Yang 2007). Although such biological grafts may be immune-compatible, they often lack the required mechanical properties to maintain long term airway patency. To circumvent this limitation, attempts have been made to reinforce these autogenous tissues with foreign materials like silicone stents. However, the need for a secondary surgical site and donor site morbidity are still major disadvantages associated with this method (Yamashita 2007).

Fresh allografts are another alternative that has been explored. They usually require lifelong immunosuppressive therapy, which is undesirable in patients with extensive tracheal carcinoma (Grillo 2002). Macchiarini *et al.* (2008) has successfully

performed an allograft transplant by decellularizing a trachea segment from a human donor and repopulating the scaffold with the patient's autogenous cells before implantation. Although this method may address the issue of immunogenicity (Go 2010), the lengthy process behind it and difficulty in obtaining a good geometrical match of the donor trachea are still unmet needs(Fishman 2011).

Synthetic grafts of various material types have been extensively studied (Kawaguchi 2001, Park 2012, Tada 2012, Tsukada 2009). Tsukada *et al.* (2009) has experimented and evaluated artificial tracheas consisting of different types of bioabsorbable material sheets that were reinforced with a metallic stent as well as non-absorbable materials like Dacron (Tsukada 2004). Polypropylene mesh scaffolds layered with collagen sponge were developed by Nakamura *et al.* (2009) to provide suitable bedding for epithelium growth into the lumen. These artificial tracheas have high failure rates due to mechanical properties mismatch between implants and tracheas and the slow rate of epithelium migration (Yamashita 2007). Geometrical mismatch may also impede epithelium in-growth from the resected ends of the trachea into the prosthesis, resulting in eventual stenosis and implant failure. Prior works by the authors have been done on the development of a patient-specific PDMS tracheal prosthesis and carbon nanocomposites by the authors (Chua 2013).

There are several reviews on the potential of CNT based composites as biomaterials (Chłopek 2006). Most works focus on the use of carbon nanocomposites in bone and cartilage replacements (Sahithi 2010). Besides their non-biodegradability and excellent mechanical properties which make them ideal for permanent implants, CNT can be formulated to mimic the nanostructure of the ECM and enhance cell growth and

activity (Harrison 2007, Sahithi 2010, Tran 2009). Studies have indicated that CNT based substrates are proficient in accelerating the recruitment, growth and differentiation of osteoblasts and mesenchymal stem cells, which are crucial for bone and cartilage formation, respectively (Harrison 2007, Mooney 2008). Shi *et al.* (2007) has fabricated porous ultra-short SWCNT composites for bone tissue engineering and the material was proven to have superior osteoconductivity. CNT coatings applied on bone implants also showed improved bioactive behavior as CNT provided a template for the deposition of hydroxyapatite layers during bone regeneration (Boccaccini 2007). The use of CNT in polymeric composites can confer exceptional flexibility as well as strength (Zhan 2003), making it suitable for replacements that require a certain degree of bending, stretching and rotation like the trachea. Furthermore, these nano-inclusions reinforce the implants by reducing chances of brittle and ductile fracture under cyclic stresses (Thostenson 2001). Doping of natural materials, like chitosan and collagen, with CNT has shown promising results as well (Lau 2008).

Due to the superior mechanical properties and bioactivity of CNT based composites as presented, we hypothesize that a non-biodegradable CNT-PDMS nanocomposite can be used as the core material to develop a scaffold for tracheal replacement, which will be able to provide the necessary mechanical support for airway patency and trachea motions while promoting faster regeneration of the epithelium than current methods. The material's non-biodegradability and resistance to ductile failure can replace the functions of the resected cartilage rings as a permanent fixture under daily cyclic stresses in the patient. Furthermore, the design and fabrication of the prosthesis is patient-specific, hence translating to a better match of surfaces between the lumens of the

prosthesis and native trachea, which we believe is important for faster epithelial cell migration.

Simulation of the prosthesis design within 3D patient-specific tracheal model was performed to study the stress distribution of the prosthesis-implanted trachea and the suitability of the design. Also, in-vitro studies have been conducted to evaluate the biocompatibility of the graft and its ability to support epithelial cells proliferation and differentiation. Lastly, six in-vivo experiments in porcine models were carried out to provide a more comprehensive study of the material and design.

5.2 Methods and Materials

5.2.1 Artificial Tracheal Prosthesis

The multi-material tracheal prosthesis consists of a CNT-PDMS composite skeleton and biodegradable Type I collagen sponge (Figure 5.1). The non-degradable skeleton of the prosthesis is a permanent fixture in the trachea and takes over the function of the resected cartilage rings by providing structural support and maintaining airway patency. CNT added to the PDMS polymer can allow for tailoring of mechanical properties of the scaffold to closely mimic that of the natural tissue (Khan 2013, Thostenson 2003). This is important as the trachea is a dynamic tubular structure that experiences rotation, bending and stretching in daily activities. The Young's Modulus and Poisson ratio of PDMS (*Sylgard*® 184 Silicone Elastomer) in 10:1 ratio has a value of 2.60MPa and 0.45, respectively (Mata 2005, Schneider 2009), which is closely matched to that of the cartilage rings which are 3.33MPa and 0.49, respectively (Trabelsi 2010). The carbon nanotubes confer additional stiffness and enhance the strength of the composite and make it less prone to failure by shearing and ductile fracture. In addition,

the biocompatibility of CNT-PDMS nanocomposite has been proven in several literatures (Ha-Chul 2012, Sepulveda 2013, Zhou 2012) and further verified in this study.

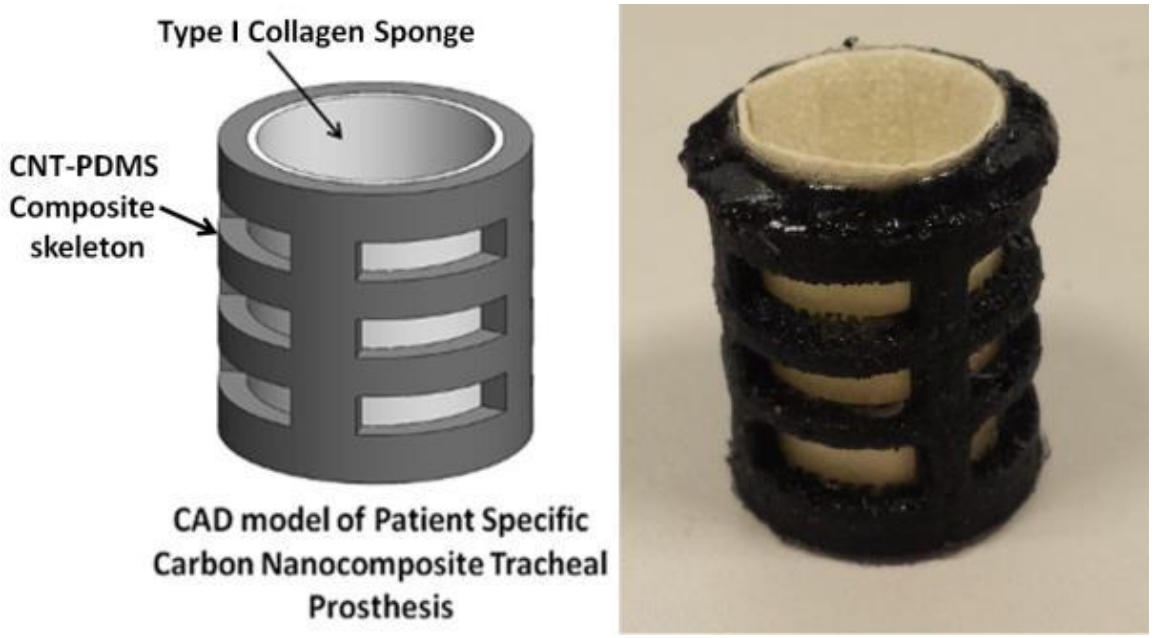

Figure 5.1: (Left) An isometric CAD model of the carbon nanocomposite tracheal prosthesis and its constituents. (Right) The final fabricated device without the external layer of collagen sponge.

The degradable portion consists of a layer of Type I porcine collagen sponge in the inner and outer surface of the CNT-PDMS skeleton. Type I porcine collagen has been shown to promote the proliferation and differentiation of the ciliated epithelium, which facilitates mucous removal from the trachea (Davenport 1996, Tada 2012). It also renders the device air tight when implanted, hence preventing leakages of interstitial fluids into the airway which could result in pneumonia. The collagen matrix is loaded with the protein Vascular Endothelial Growth Factor (VEGF) prior to implantation to accelerate vascularization and angiogenesis of the prosthesis, thus providing nutrients for the migration of ciliated epithelium from the distal ends (Genden 2003, Li 2005, Nomi

2006). The collagen matrix will degrade gradually and is replaced by tissue until the entire skeleton is engulfed by the regenerated membrane.

The fabrication of the CNT-PDMS skeleton is done via rapid prototyping of the mold followed by molding process. The mold model was designed according to patient-specific dimensions and its individual components were fabricated by rapid prototyping. The design is also such that it can be easily dismantled to facilitate easier removal of the cured composite part. PDMS pre-polymer (Sylgard 184^{TM} Silicone Elastomer, Dow Corning, Singapore) was combined with its curing agent in a 10:1 ratio and thoroughly mixed with a controlled amount of multi-walled carbon nanotubes (Sigma Aldrich, Singapore) via sonication for 1 hour to achieve homogeneity. The mixture was then poured into the mold and left in a vacuum oven for 1 hour to remove any trapped bubbles which could affect the mechanical properties of the cured device. It was left to cure in the oven at 100^0C for 2 hours, after which, the solid nanocomposite is removed from the mold.

A second aluminum mold was used for the fabrication of the Type I collagen sponge over the surface of the prosthesis. Type I porcine collagen (Sigma Aldrich, Singapore) was dissolved in aqueous hydrochloric acid (pH 3) to give a final concentration of 1% by weight (Yamashita 2007). This was followed by the homogenizing of the solution at 8000rpm for 15 minutes. . The cured CNT-PDMS scaffold was placed into the hollow region of the mould and the collagen solution was poured carefully into the mold cavity. The mold was placed into a freeze drier at -80^{o}C for 2 hours and then into a vacuum oven at 140^{o}C for 12 hours for cross linkage to occur.

This will slow down the degradation of the collagen sponge *in-vivo*. Upon completion, the collagen coated prosthesis was sealed in an air tight packaging and UV sterilized.

5.2.2 Simulation

Computational evaluation of the designed prosthesis was performed using simulation of a patient-specific augmented trachea undergoing daily motions of bending and stretching (Chua 2013). In a separate study, Palomar *et al.* (2010) has simulated a stent implantation into a patient-specific trachea to predict the outcome which was useful for optimization of the design.

Briefly, collated 2D images of the diseased trachea are processed to identify the contours of the cartilage rings, which are used for the dimensions of the prosthesis cross section (Figure 5.2). Next, a 3D patient-specific trachea model is reconstructed based on the volumetric CT images of the patient's trachea in the axial direction. The trachea model comprises primarily of 2 different tissues, namely the membranous tissues and the cartilage rings, each with their own different mechanical properties. Although recent research has utilized the elastic Neo Hookean model for tracheal cartilage behavior and Holzapfel strain energy of two orthogonal families of collagen fibers for the membranous tissue (Trabelsi 2010), these models were invalid for a 3D model undergoing motions due to the former's inherent assumption of incompressibility. An assumption was made in that the mechanical property of the cartilage ring is homogenous and linearly elastic for strains of up to 10% with minimal residual strains (Rains 1992). The mucosa membrane has been shown to behave differently in the longitudinal and transverse directions, hence it was modeled as an orthogonal behavioral material with different properties in all three

principle axis according to values from *Sarma et al* (2003). The values used in the simulation are presented in Table 5.1.

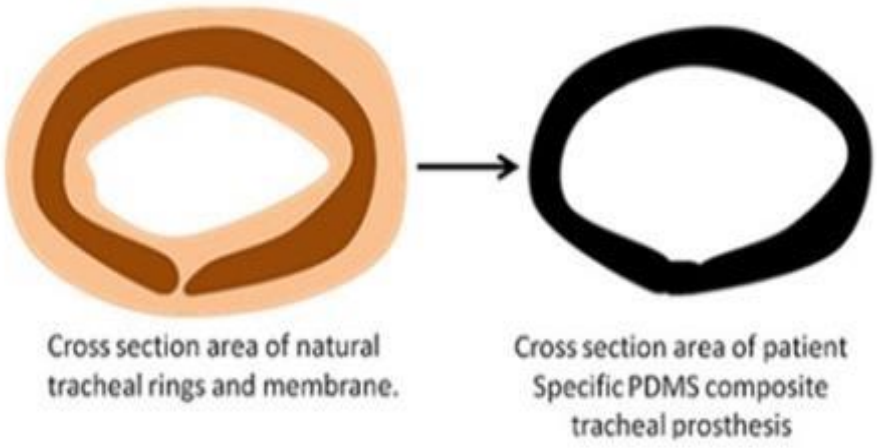

Figure 5.2: The contour of the cartilage rings are identified and imported to design the cross section of the prosthesis skeleton.

TABLE 5.1

Mechanical properties values of the tracheal cartilage rings and mucosa membrane.

Tracheal cartilage rings		Mucosa membrane		
E = 3.33MPa	$\upsilon = 0.4$	E_{xx}(longitudinal)=0.36MPa	G_{xy}=0.124MPa	υ_{xy}=0.45
		E_{yy}(transverse)=0.3MPa	G_{xz}=0.124MPa	υ_{xz}=0.375
		E_{zz}(radial)=0.3MPa	G_{yz}=0.124MPa	υ_{yz}=0.375

The center two cartilage rings from the tracheal model were removed and replaced with the designed scaffold (Figure 5.3). This is to simulate the final state in which the prosthesis skeleton is embedded in the membranous tissue after a period of tissue regeneration and complete collagen degradation. For comparison purposes, prostheses with modular circular and patient-specific shapes were designed and material properties of 316L stainless steel and CNT-PDMS were used. The assembly was then

subjected to stretching and bending motions in a multi-physics program to study the stress concentrations in the different regions during daily motions of the trachea. Longitudinal stretching by 10% strain (due to swallowing) and sideways bending in the Y and Z directions (due to head movements) were simulated on both natural and augmented tracheal models to study the stress effect of the prosthesis on surrounding membrane and cartilage rings. Maximum stress concentration values were computed from the surrounding membrane and cartilage rings and the results are plotted.

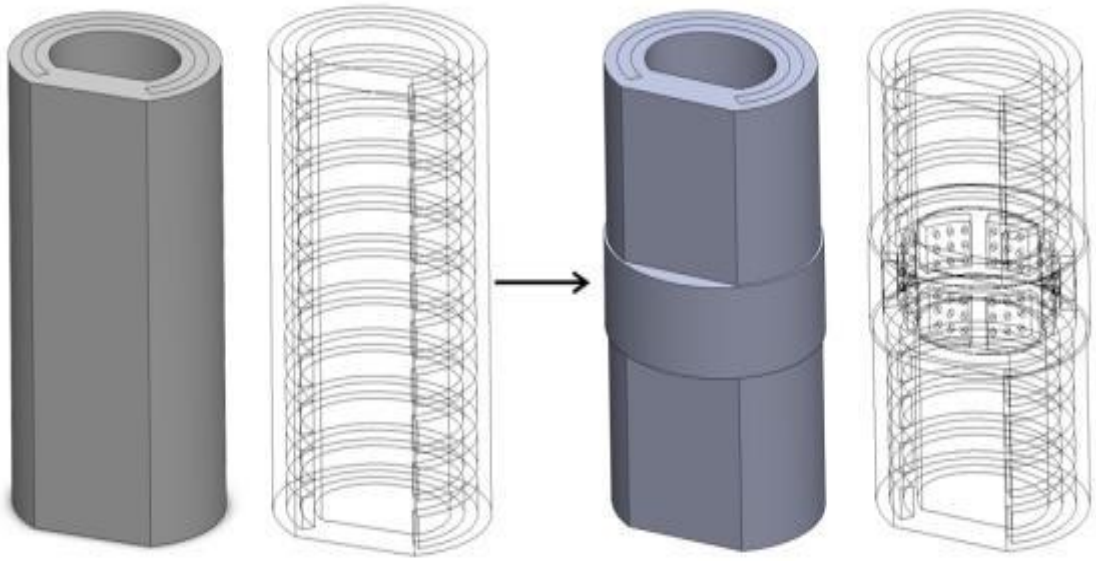

Figure 5.3: (Left) Natural tracheal model and (Right) augmented tracheal model with the center rings replaced with the prosthesis.

5.2.3 *In-Vitro* Experiment

The main aim of the in vitro cell culturing is to verify the ability of the proposed PDMS-CNT composite to support tracheal epithelial cell proliferation and differentiation. To the authors' best knowledge, there has not been any permanent implant made from PDMS-CNT nanocomposite and thus this experiment serves to assess its suitability for cell growth and differentiation.

Porcine tracheas were obtained fresh from the local slaughterhouse. The pigs slaughtered were weighed and determined to be approximately 45kg and healthy. The tracheal cells were harvested via methodology proposed by Mao *et al.* (2009). Briefly, the tracheas were immersed into cold Hanks solution (Sigma, St. Louis, MO) to maintain the tissue freshness until it was ready for dissection of the mucosa layer. The epithelial mucosa was carefully removed from the tracheas and washed 5 times using M199 (Bio-Source International, Camarillo, CA) with antibiotics. After which, the tissues were sliced into small pieces and incubated at 4^{o}C overnight in M199 supplemented with 1X of penicillin/streptomycin (Gibco, Grand Island, NY) and 0.6mg/ml type IV protease (Sigma, St. Louis, MO). Clusters of epithelial cells were harvested the following day by gently agitating the pieces of the sliced mucosa in a Petri dish containing M199 with 10% FCS (ATCC, Manassas, VA). The cells were then washed five times with M199 supplement with 1X of penicillin/streptomycin mix and re-suspended in medium BEGM (Lonza, Walkersville, MD) containing 5% FCS and 10-7M RA. The ingredients used in the BEGM include: epidermal growth factor (0.5ng/ml h_EGF), insulin (5µg/ml), hydrocortisone (0.5µg/ml), transferrin (10µg/ml), epinephrine (0.5µg/ml), triiodothyronine (6.5ng/ml), bovine pituitary extract (60µg/ml), gentamicin (50µg/ml), cholera toxin (10ng/ml), retinoic acid (0.1ng/ml), amphotericin (50ng/ml) and 0.8% penicillin-streptomycin. The cells were then stored under cryopreservation until they were needed.

Scaffold pieces with dimension 1 cm by 1 cm and 0.2 cm thickness were prepared. Prior to seeding, the batch of nanocomposites were subjected to UV sterilization and rinsed with PBS containing antibiotics. One scaffold was placed into

each well of the 12-well plates (Corning, USA) and 2ml of BEGM growth media was added, and pre-incubated at 37°C for 2 hours and then aspirated. Approximately 10,000 cells (in 100uL growth medium) were seeded onto each scaffold and incubated in at 37°C with 8% CO2 and 95% humidity for 4 hours for attachment to take place. After which, the scaffolds were transferred in new well plates and fresh 2ml BEGM growth medium were added in each well before being placed in the incubator. The old well plates were inspected under the microscope for any residual cells to ascertain that the tracheal cells have attached to the scaffold surface. The culture media was changed every 2 days. On the 2nd, 5th and 7th day, samples were taken out for assessment.

The samples were fixed in 2.5% glutaraldehyde in PBS (pH 7.4) for 4 hours at 4°C. Following which, the samples were rinsed with PBS and then fixed in Osmium for 2 hours. The samples were rinsed again with PBS and then dehydrated using graded ethanol series from 10% to 100% with three times 10 minutes incubation at the final concentration. The next phase of dehydration was by critical point drying using CO2. The specimens were then sputter coated with gold and viewed on a JEOL 5660LV scanning electron microscope (JEOL Asia Ltd). In addition, Quant-iTTM PicoGreen® dsDNA Assay Kit (Invitrogen, Oregon, USA) was used to stain for the presence of cell nuclei on the samples, while LIVE/DEAD® Reduced Biohazard Cell Viability Kit #1 (Invitrogen, Eugene, OR) was used to stain for the presence of live and dead cells.

5.2.4 *In-Vivo* Experiment

The aim of the in vivo animal experiment is to evaluate the effectiveness of the graft as an airway replacement. Briefly, pre-operation CT scans were conducted on 6 healthy female pigs, weighing around 60kg, to obtain the cross sectional image of the

tracheas. Subsequently, the prostheses were designed and fabricated based on the acquired trachea cross sectional contour of each pig. We compared 4 different prosthesis modifications of varying pore sizes, lengths and collagen sponge coatings. The details are summarized in Table 5.2 in the Results section. The animals were placed under anesthesia in a supine position on the operating table where incisions were made and 30mm of trachea was excised. The prostheses was soaked in the pig's blood to render it air tight and sutured to the resected ends of the trachea, after which another layer of collagen sponge was wrapped around the prostheses to prevent any leakages into the lumen (Figure 5.4). The pigs were finally sutured using degradable sutures and antibiotic ointment was applied on the wound to prevent infection. Post operation CT scans were performed immediately after surgery to inspect the airway with the new graft to ensure no blockages. Lastly, administering of antibiotics and standard post-operative care regimes were undertaken according to approved Institutional Animal Care and Use Committee protocol (IACUC No:133/12). The pigs were kept alive and monitored for 2 weeks before being sacrificed and their prostheses harvested for histology evaluation.

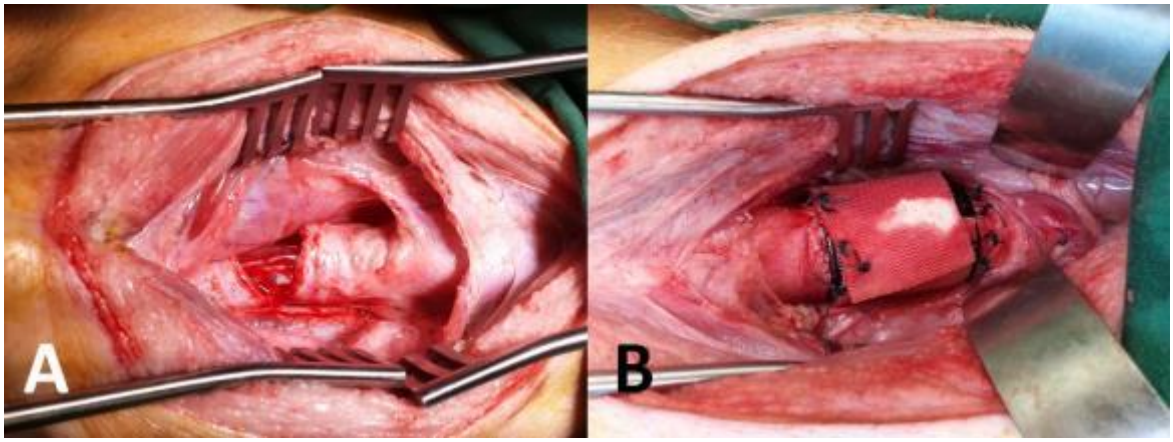

Figure 5.4: (A) The trachea exposed with the middle 30mm of it resected and removed. (B) The patient-specific CNT-PDMS prosthesis joined to the resected ends of the trachea with an additional layer of collagen sponge sutured around as a preventive measure to keep it air tight.

5.3 Results

5.3.1 Simulation

Simulation studies were performed on the designed prostheses with the trachea model under various loading conditions to study the stress outcome. Figure 5.5 shows that the stress computed in the patient-specific CNT-PDMS prosthesis is almost similar to the stress experienced by the natural cartilage ring in a healthy trachea. Furthermore a patient-specific shape results in a lower stress level in the prosthesis. In Figure 5.6, the membrane stress results are lower with the patient-specific CNT-PDMS composite compared to other cases, despite being higher than that of the membrane in a natural trachea. Similarly, Figure 5.7 shows the stress reduction of the surrounding cartilage rings in a CNT-PDMS implant scenario. Similarity in stress levels to the natural state is crucial as it reduces the chances of evoking granulation tissue overgrowth and tissue necrosis, which would lead to stenosis and eventual implant failure. Thus, patient-specificity in the designed implants can produce desirable outcomes in terms of device-tissue interactions.

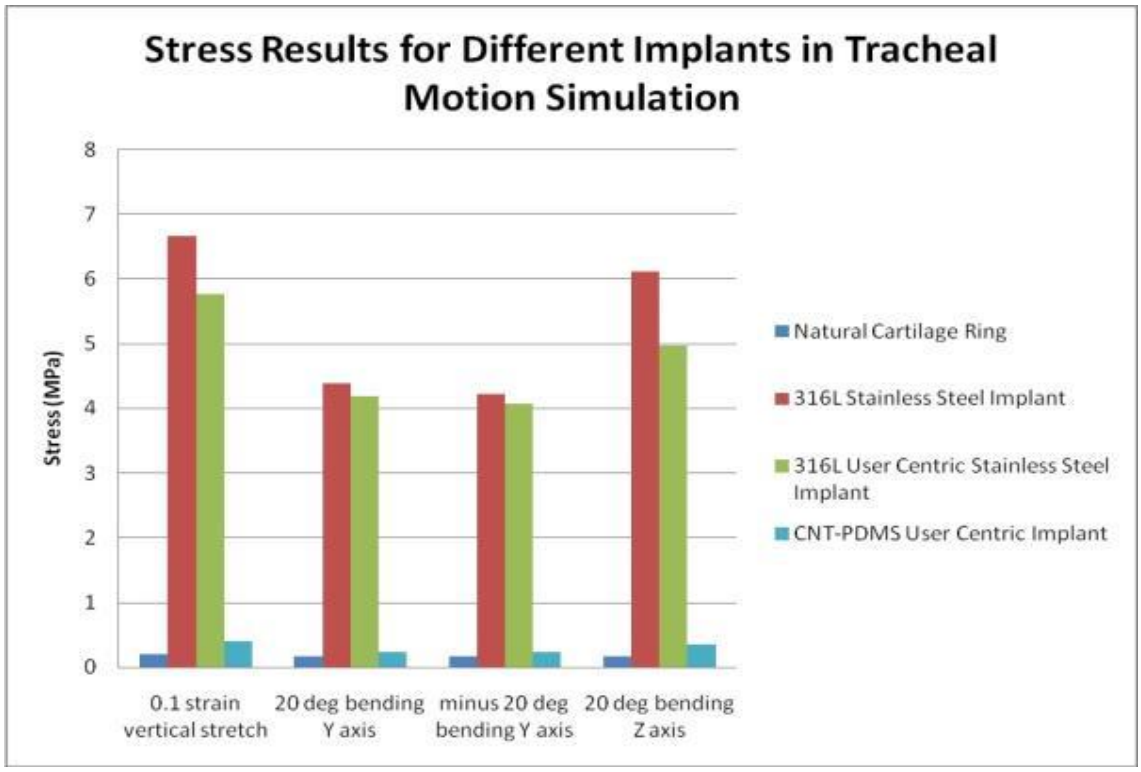

Figure 5.5: Graphs showing maximum stress in the different prostheses under different loading conditions.

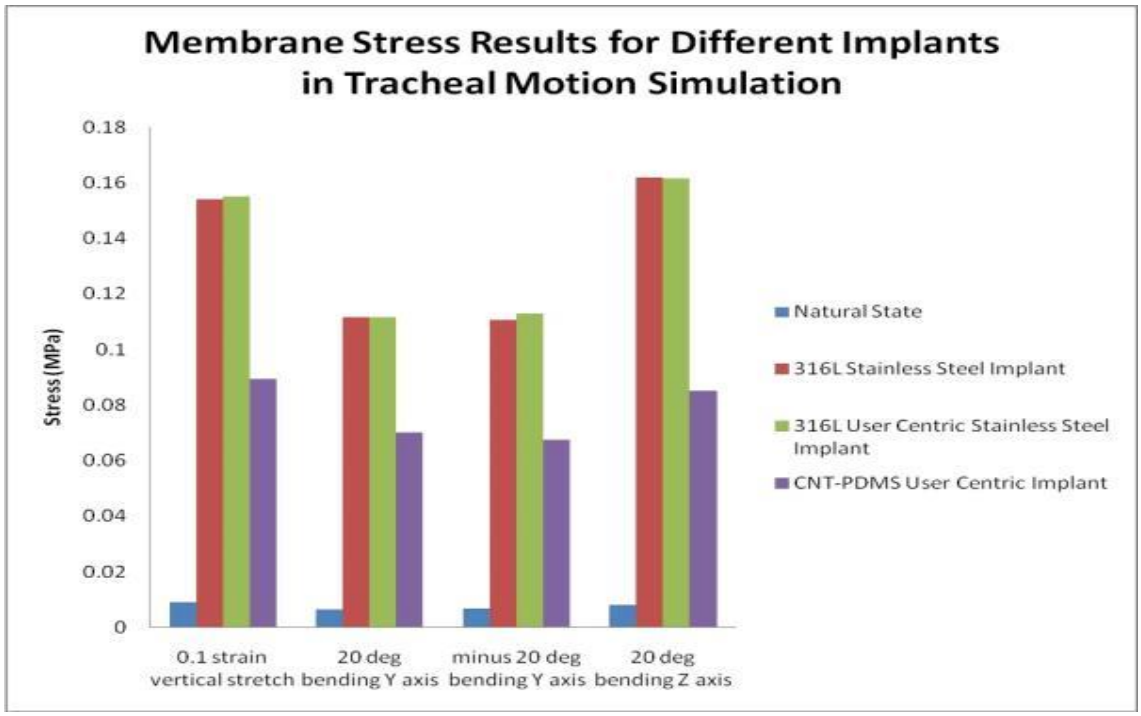

Figure 5.6: Graphs showing maximum stress in the surrounding mucosa membrane under different loading conditions and prostheses types.

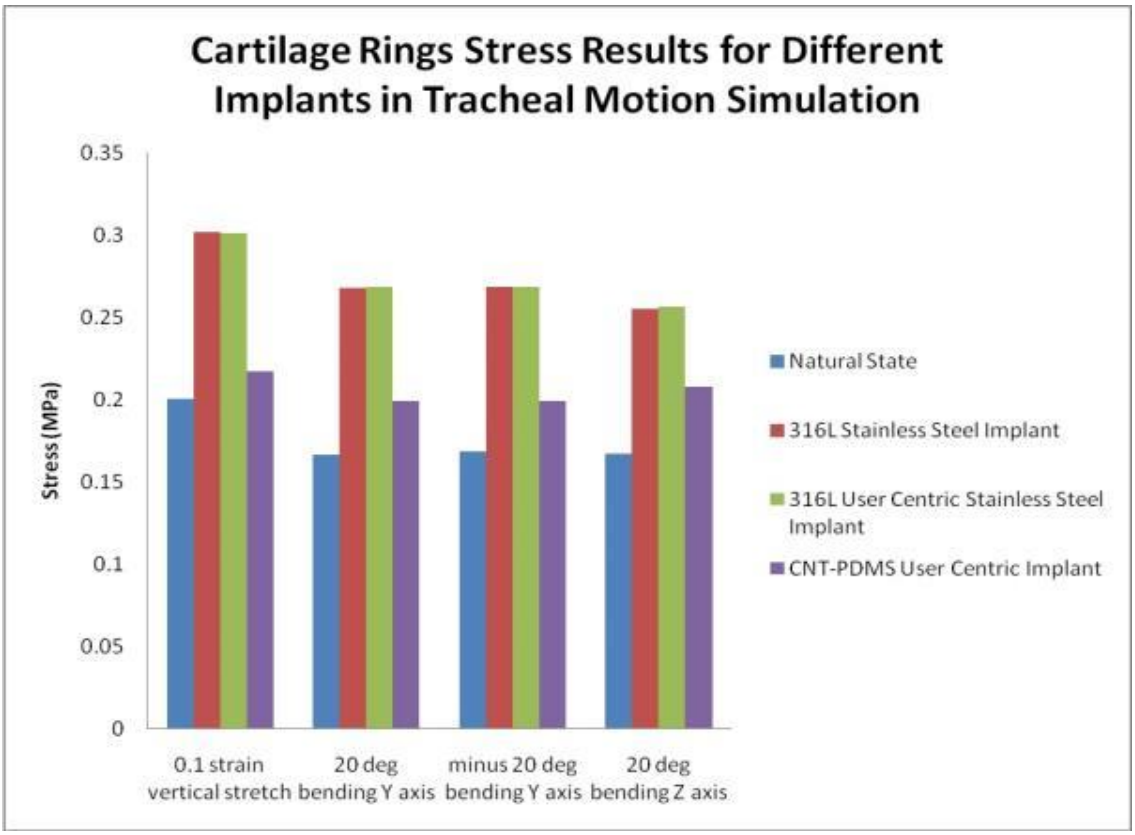

Figure 5.7: Graphs showing maximum stress of the neighboring cartilage rings under different loading conditions and prostheses types.

5.3.2 *In-Vitro* Experiment

Micro-plate readings of the PicoGreen® stained samples (Figure 5.8) have indicated an increased in the DNA concentration over the period of 7 days. The readings were obtained from a sample size of 3 per time point. Images captured by fluorescence microscopy (Figure 5.9) for LIVE/DEAD® staining of cells shows greater number of live (green) cells than dead (red) cells in both time point of 2nd and 7th day. The density of live cells also seems to be greater on the 7th day compared to the 2nd day. In addition, the confocal images reflect the formation of cell to cell adhesion, a possible evidence of healthy epithelial cell growth. These results indicate the ability of the PDMS-CNT

nanocomposite to provide a biocompatible and conducive environment for the proliferation of the tracheal cells.

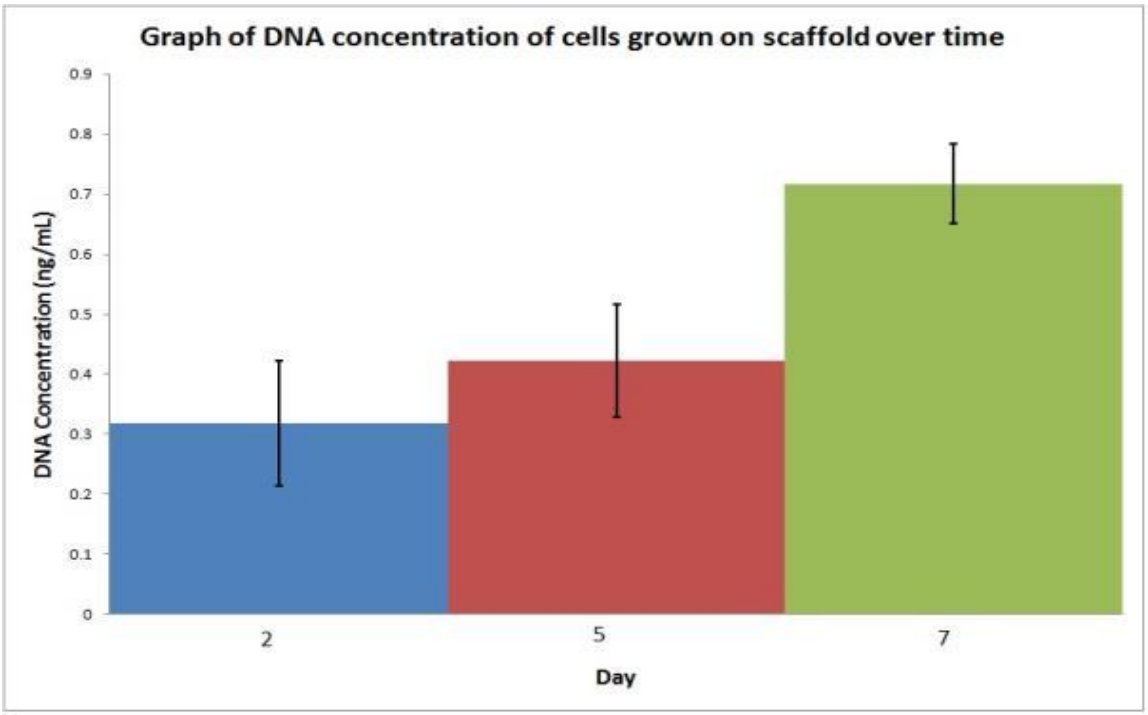

Figure 5.8: DNA concentration of cells grown on the scaffold measured by microplate reader over time.

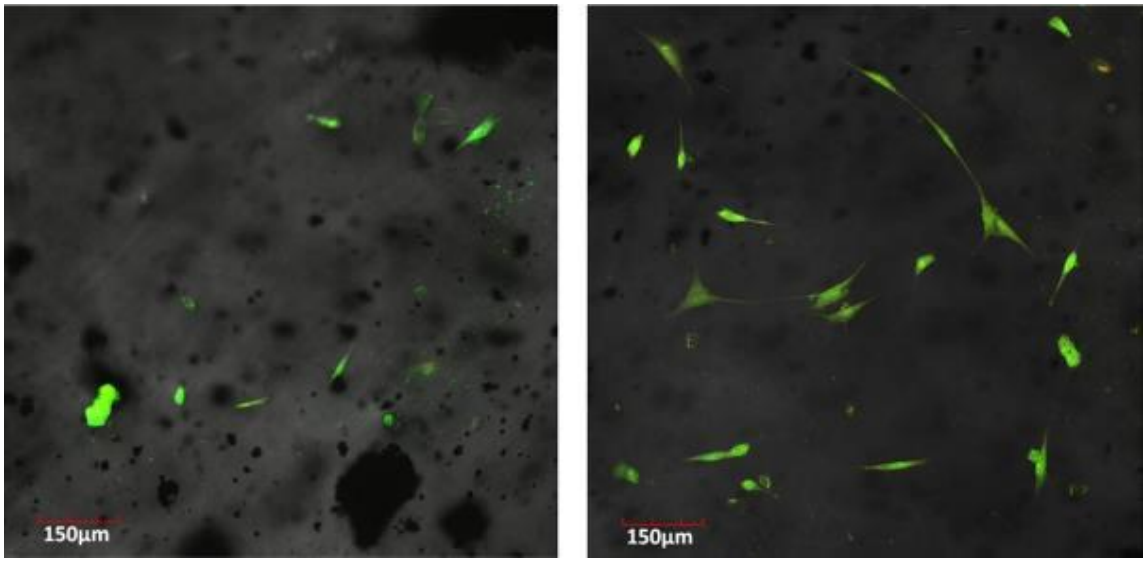

Figure 5.9: Confocal microscopy images (20 X) with phase contrast background of LIVE/DEAD® staining of cells on the 2nd day (left) and 7th day (right). Green stains indicate live cells while red stains indicate dead cells. Black particles in the background indicate the carbon nanotubes embedded in the PDMS matrix.

SEM images of the cells on day 2 show that the cell surfaces are almost devoid of cilia (Figure 5.10). By day 5, a substantial density of cilia was observed on the surfaces of the tracheal epithelial cells (Figure 5.11). The ciliated structures found on the surface of cells are comparable to those in literature (Chopra 1992, Mao 2009, Ziegelaar 2002). This highlights the capability of the CNT-PDMS composite to support the ciliogenesis of the trachea epithelial cells grown on its surface. A greater cell density was also observed in the SEM images on day 5 which is consistent with the previous results from LIVE/DEAD® staining and Picogreen® staining.

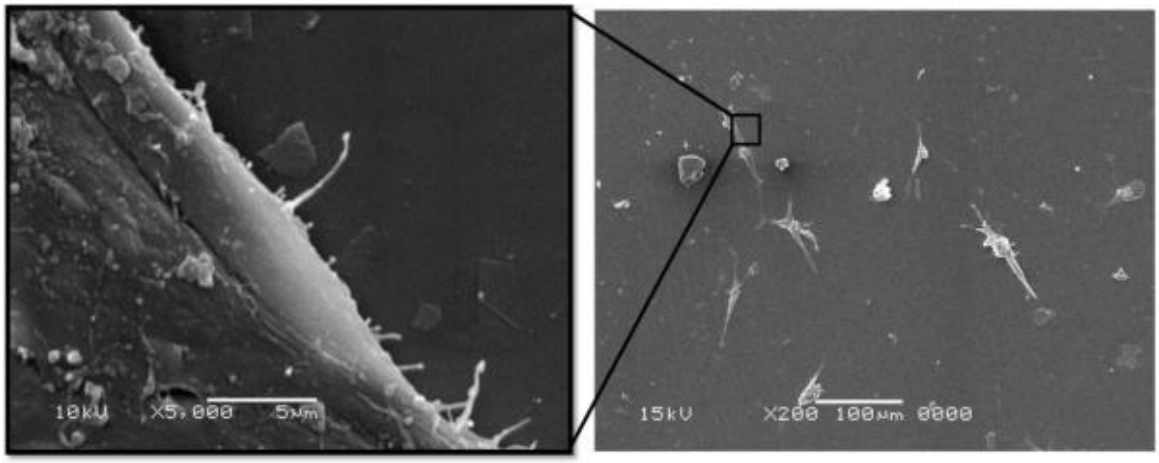

Figure 5.10: SEM images of the trachea cells in lesser density on the 2nd day (right) with minimal cilia on the cell surface (left).

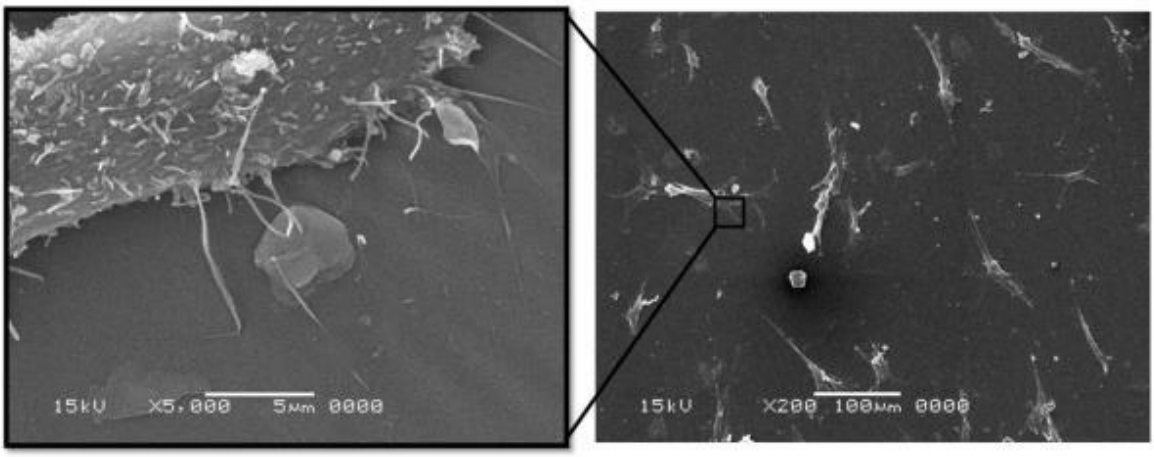

Figure 5.11: SEM images of the trachea cells in greater density on the 5th day (right) with more cilia sprouting on the cell surface (left).

5.3.3 *In-Vivo* Experiment

The *in-vivo* airway replacement surgery performed on 6 pigs were sucessful. Besides the first pig which died of complications during endoscopy on the 7th day, the remaining five pigs managed to survive for 2 weeks. The animals were able to resume daily activities with unhindered neck and head motions and appetite was as per normal. However, the studies were terminated by the end of the second week as the pigs either started developing stenosis at the site of anastomosis or did not survive.

TABLE 5.2
Summary of *in-vivo* experiments

Pig No.	Prosthesis Configuration			Duration	Observations at sacrifice
	Pore Size	Length	Collagen sponge coating		
1	1.5 mm	10 mm	Inner and outer	1 week due to complications during attempted endoscopy.	N.A.
2	1.5 mm	10 mm	Inner and outer	2 weeks	Ingrowth and complete epithelium in lumen.
3	1.5 mm	30 mm	Inner and outer	2 weeks	Ingrowth and complete epithelium in lumen.
4	0.6 mm	30 mm	Outer	2 weeks	Ingrowth and partial epithelium in lumen.
5	0.6 mm	30 mm	Outer	2 weeks	Ingrowth and partial epithelium in lumen.

6	4 by 2 mm	30 mm	Inner and outer	2 weeks	Ingrowth and complete epithelium in lumen.

Post-operation CT scans of the pigs shows the graft in position and mantaining airway patency (Figure 5.12). During the 2nd week, the pigs were placed under general anaesthesia and a laryngoscope was introduced into the trachea to inspect the lumen. It was observed that for cases with double sided collagen coating configurations, the inner lumen of the prostheses had been covered with a layer of epithelium (Figure 5.13A). At the point of sacrifice, the scaffolds were harvested and an incision was made longitudinally to expose the lumen. Substantial tissue in-growth into the pores of the prostheses were observed in all cases with no remnants of the collagen sponge left. For those with initial inner collagen sponge coatings, the lumen surfaces were covered completely with a layer of epithelium that was continuous with the resected ends of the native trachea (Figure 5.13B). However, prosthesis configurations that did not have an inner coating of collagen sponge resulted in partial and discontinous epithelization. Variation of the three different pore sizes and two lengths of the prostheses did not seem to have any noticeable impact on the post-sacrificial end results.

A transverse section of the prostheses was histopathologically evaluated for the five pigs. Due to the processing of tissue using xylene, the scaffold was dissolved with no remnants of it in the histogy section (Figure 5.14). There was mucosa and submucosa present around the prosthesis with intact neutrophils and lymphocytes and plasma cells. Some inflammatory cells were present in the surrounding tissues and there was goblet cells hyperplasia and mononuclear cells infiltration into the pores of the prosthesis. The lumen of the prostheses were observed to be completely lined by epithelial cells for the

prostheses with inner collagen coating. The *in-vivo* study has demonstrated that the nanocomposite scaffold was able to mantain airway patency and faciliate epithelium regeneration with no breathing difficulties observed.

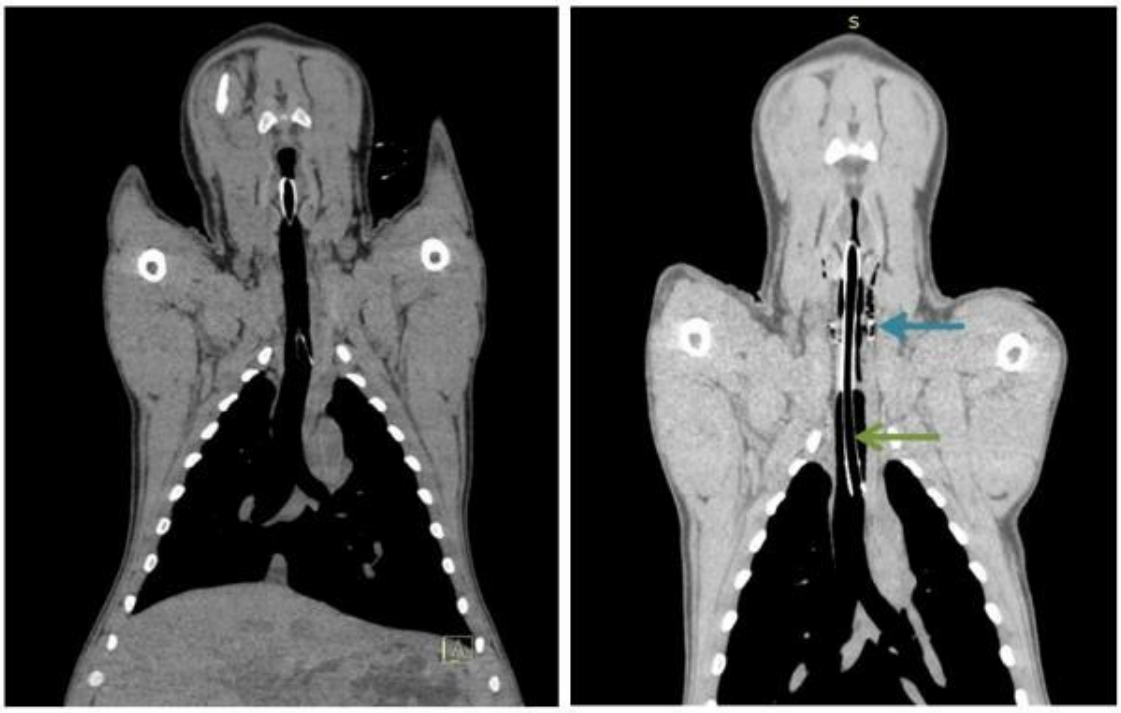

Figure 5.12: Pre-op CT scans of the pig (Left). Post-op CT scans of the pig (Right). Blue arrow indicates the tracheal prosthesis implanted while the green arrow shows the intubation tube.

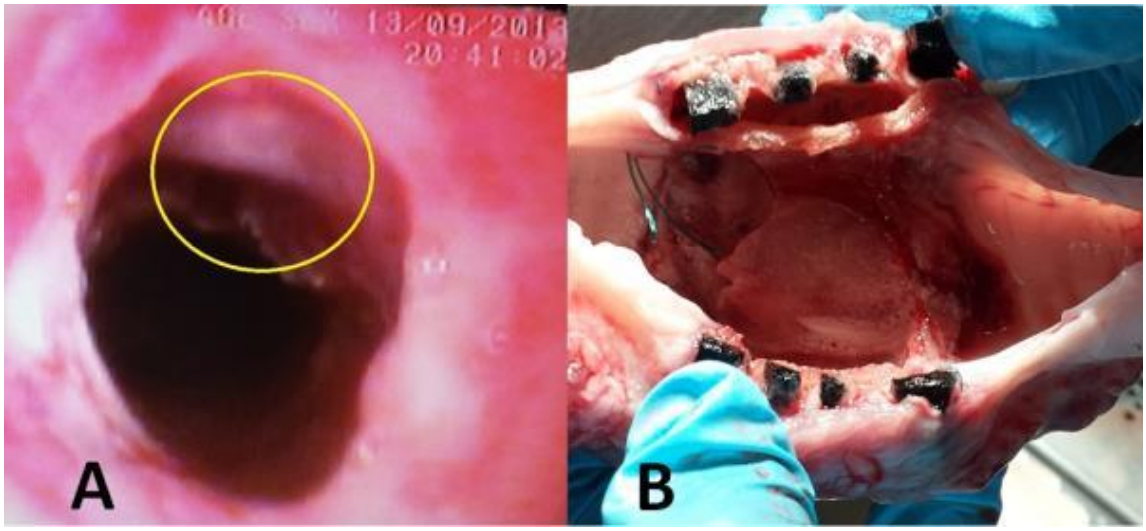

Figure 5.13: (A) Endoscopy showing successful epithelialization of the double-sided collagen coated prosthesis lumen by the 2nd week as shown by the yellow circle. (B)

Exposed lumen of the prosthesis has a complete layer of epithelium and substantial tissue ingrowth has occurred at point of sacrifice.

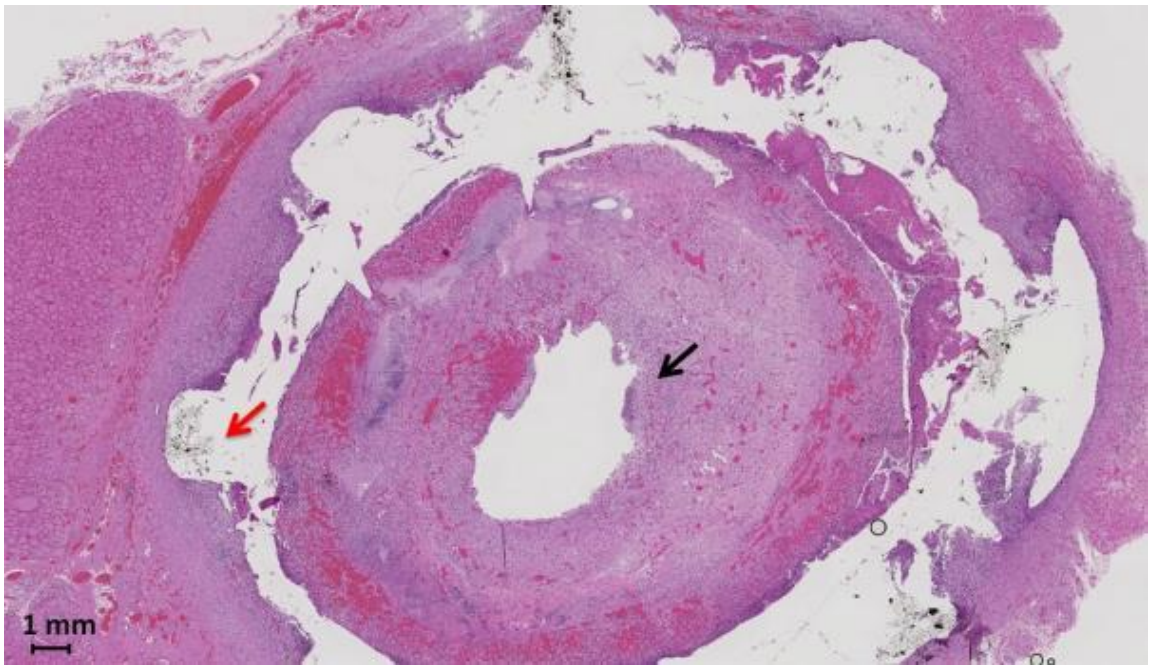

Figure 5.14: H&E staining of the transverse section of the tissue-scaffold sample. Black arrow indicates regenerated epithelial cell layer while the red arrow points to the void produced by the dissolved scaffold.

5.4 Discussions

5.4.1 Biocompatibility of CNT-PDMS

In airway replacements using synthetic materials, it is reported that the cartilage rings do not regenerate in the resected portion of the trachea, despite the membranous tissue and epithelium ingrowth into the prosthesis (Doss 2007). The ideal prosthesis should therefore be biocompatible to host the migration, proliferation and differentiation of tracheal cells, while maintaining the construct's long term non-biodegradability and mechanical properties in order to assume the functions of the resected rings. The biocompatibility of our CNT-PDMS composite has been validated via in-vitro and in-vivo experiments conducted. From the in-vitro study, tracheal epithelial cells cultured on the CNT-PDMS displayed an increase in cell population and cell-to-cell adhesions over 7

days and an elongation in cell shape. This is similar to the reported findings by Barrow *et al.* (1992) whereby reparative proliferation of trachea epithelial cells between the 4th and 8th day is marked by the differentiation of hyperplastic cells through its elongation and formation of cell to cell contact, after which leading to ciliogenesis of non-ciliated cells. From the SEM pictures, an observable increase in cilia density on cell surface indicates cell viability and differentiation. This may be attributed to the dimensional similarity of CNT to cartilage, which causes it to exhibit unique surface properties due to their significantly greater surface area and roughness, hence improving cell adherence on the material and boosting their bioactivity (Zhang 2009).

Our in-vivo experiments have shown that the CNT-PDMS material is also non-toxic as there was no severe tissue necrosis present around the implant. The presence of a healthy mucosa and sub-mucosa around the implant and a complete lining of epithelial cells in the lumen further substantiate the biocompatibility of the material. Another primary concern of the materials used to reconstruct an artificial airway is hydrolysis and weakening of mechanical strength over time due to enzymatic activities and chemicals in the body (Jungebluth 2011). This can potentially result in the premature collapse of the construct after a period of constant cyclic stresses and obstruction of the airway. However, careful inspection of the core CNT-PDMS scaffold after sacrifice showed no surface erosion or reduction of structural integrity, which indicates a degree of in-vivo chemical stability. Therefore, CNT-PDMS nanocomposite material may be a suitable replacement for non-regenerative tissues due to its physical and chemical durability.

5.4.2 Mechanical Properties and Design of Prosthesis

The prosthesis should be as flexible as the natural trachea tissue and possess mechanical strength to resist buckling under external pressure and failure due to cyclic tensile stresses and anastomotic tension of the sutures. The use of CNT-PDMS as core material in the prosthesis has demonstrated unhindered natural motions of the prosthesis of the pigs in daily activities without causing stress erosion to neighboring tissues that may result from stiffer implants (Doss 2007, Kucera 2007). Such materials may be deployed in other biomechanical applications that involve dynamic loading and actuation such as cartilage and soft bone replacements. Although the utilization of CNT in the tracheal prosthesis has not be optimized, it permits control of properties by varying orientation and concentration of CNT within the spatial architecture of the construct to better mimic the non-homogenous properties of cartilage rings in future studies (Harrison 2007, Rains 1992).

With the current paradigm shift towards patient-specific treatment and devices, this study has evaluated a medical implant developed in this direction. Simulation results have established that patient-specificity in design leads to lower and more natural stress levels in the prosthesis and its surrounding tissues. This is crucial for optimal cell functioning, growth and remodeling as cellular activities are affected by its surrounding mechanical stress and excessive levels may lead to cell necrosis (Benhardt 2009, Shimko 2008, Swartz 2001). Studies have highlighted that incomplete and slow rate of epithelium regeneration is one of the main causes in tracheal graft failure due to granulation tissue overgrowth and subsequent stenosis (Doss 2007, Grillo 2002). The *in-vivo* experiments displayed an accelerated regenerative process whereby complete epithelialization

occurred over the prosthesis lumen within 2 weeks of implantation, compared to the reported time of 4-8 weeks from literature (Elliott.2013, Kanzaki 2006, Tada 2012, Tsukada 2004). It is believed that the identical match of the prosthesis cross sectional geometry to the remaining ends of the native trachea has created a seamless connective terrain that promoted unhindered and quicker migration of the epithelium into the lumen. In addition, the presence of the collagen sponge layer in the lumen plays a vital role to guide and accelerate epithelial cell migration from the distal ends of the prosthesis lumen. In two of the in-vivo studies utilizing prostheses without an inner collagen sponge layer, the epithelium formation was slower, incomplete and discontinuous within the similar span of time. Similarly, other studies have reported that the use of collagen sponges have stimulated epithelium development (Chvapil 1977), possibly because it is one of the major constituent of tracheal tissue and its ability to induce mucociliary differentiation of epithelial cells (Davenport 1996).

Hence, a patient-specific and tissue-specific approach may be applied in the design of implants to yield a desirable outcome which is both cost and time saving. Combined with state of the art additive manufacturing, implants of biomimetic geometries, surface topographies and mechanical properties may be reproduced accurately and quickly.

A patient-specific artificial trachea made of CNT-PDMS nanocomposite material was proposed and investigated. Computational simulations and finite element analysis were used to study the stress behavior of the designed implant in a patient-specific tracheal model, while *in-vitro* studies were performed to evaluate the biocompatibility and suitability of the graft material for sustaining tracheal epithelial cell proliferation and

differentiation. *In-vivo* studies carried out in porcine models showed no adverse side effects or breathing difficulties, with complete regeneration of the epithelium in the prosthesis lumen within 2 weeks, a milestone improvement from the reported 4 to 8 weeks in literature. There are, however, limitations to this study and they are presented and discussed in Chapter 7 of this thesis.

This chapter reports the development and evaluation of a novel patient-specific CNT-PDMS prosthesis via *ex-vivo* and *in-vivo* experiments. The nanocomposite was shown to be able to successfully support epithelial cell growth and differentiation *in-vitro*. Simulation results indicated that patient-specificity produced stress results in surrounding tissues that are closer to that of a healthy trachea. Preliminary animal experiments were successful as airway patency was maintained and daily activities resumed without any signs of respiratory difficulties. A layer of Type I collagen sponge in the lumen is required for complete epithelialization of the CNT-PDMS scaffold within 2 weeks. This study holds promising potential of the use of patient-specific CNT-PDMS prostheses in airway replacements. It has also demonstrated and widened the possibilities of nanocomposites in biomimetic tissue engineering applications to yield more desirable *in-vivo* outcomes.

Chapter 6

CARBON NANOCOMPOSITE VOICE PROSTHESIS

Chua M, Chui CK, Teo C (2014). Computer Aided Design and Experiment of a Novel Patient Specific Carbon Nanocomposite Voice Prosthesis. *Computer Aided Design*. doi: 10.1016/j.cad.2014.09.002

This chapter contains work from the above article which was published in 2014. A Computer Aided Design (CAD) methodology that utilizes patient's imagining data, simulations and rapid prototyping to develop the world's first patient-specific carbon nanocomposite voice prosthesis is introduced. Finite element analysis and flow experiments were performed to study the flow characteristics of the prosthesis. Successful preliminary in-vivo experiments in porcine models were carried out to verify the feasibility of the patient-specific CAD methodology. Section 6.1 introduces voice restoration after laryngectomy and existing voice prostheses and their limitations. Section 6.2 presents the overview of the device, patient-specific CAD methodology and simulation study, while Section 6.3 describes the fabrication of the device, *in-vitro* and *in-vivo* experiments. Lastly, Section 6.4 discusses the new methodology and concludes this chapter.

6.1 Voice Restoration and Voice Prostheses

Advances in computer technology and biomedicine have created novel approaches in the design and optimization of medical prostheses (Dean 2003, Groover 1983, Rekow 1987). The Food and Drugs Administration (FDA) of the United States of America has

been promoting computational simulations in the design process as part of the prerequisite for medical device approval, due to benefits of cost saving, efficiency and safety. From the authors' best knowledge, this study is the first to utilize patient-specific Computer Aided Design (CAD) in the design, evaluation and fabrication of better voice prosthesis in speech rehabilitation (Saringer 2002, Starly 2005, Wei Sun 2002, Sun 2005).

Although many types of voice prostheses are available commercially and under research, transprosthetic and periprosthetic leakages continue to be a problem (Kress 2014, Thomson 2007). Formation of candida biofilm and inappropriate sizing shortens the lifespan of the voice prosthesis (Eerenstein 2002, Leunisse 2001). This causes inconvenience like the closure of the fistula, formation of granulation tissue and aspiration (Chone 2005). Transprosthetic leakages of food and liquid through the valve accounts for 80% of all leakages (Hilgers 2008) and often results in candida formation, which then prevents the complete closure of the valves, thus leading to even more leakages and candida formation. Candida also rapidly degrades the voice prosthesis and increase the flow resistance of air through it (Elving 2001), hence interfering with speech rehabilitation (Starmer 2011). The second problem faced by all prosthesis is the misfit of size in the fistula. Fistulas usually have irregular cross sectional areas; therefore it is hard to achieve an accurate fit since the prostheses have similar geometric shapes and fixed size ranges. A tight fit of the prosthesis will lead to the formation of granulation tissue while a loose fit results in periprosthetic leakages (Chone 2005).

Several works have been done to tackle these issues. Firstly, Leder *et al.* (2005) proposed the use of a modified flap mechanism to reduce transprosthetic leakages.

However, a potential problem with all flap-valve prosthesis is the loosening of the polymeric hinge due to cyclic stress, leading to transprosthetic leakages. A prosthesis design with a deformable esophageal flange was also investigated (Van Den Hoogen 1997). Although it was effective in preventing leakages, the air flow resistance in the prosthesis was high, thus requiring patients to exert during speech. To address issues of periprosthetic leakages, Lewin *et al.* (2012) developed the use of enlarged collars to fill up additional space between the prosthesis and the tissue that result from fistula enlargement. The drawback of their method is that it causes uneven stress distribution due to the irregular shape of the fistula, potentially causing granulation and further widening. Computational simulations can predict the in-vivo outcomes of prosthesis-tissue interactions through the input of geometrical and material parameters (Heissler 1998, Hieu 2002). Hence, a tailored and better functioning prosthesis can be obtained by embedding computational design and simulation based on patient-specific models within the design framework.

6.2 Methods and Materials

6.2.1 Patient-Specific Voice Prosthesis

The voice prosthesis comprises of multiple parts of different materials (Figure 6.1). The inner core of the prosthesis is a rigid material, Polyvinyl Chloride (PVC), in order to maintain airway patency under external pressure from surrounding tissues. It houses a magnetic ring and a magnetic stainless steel ball bearing that seals the airflow passage when the patient is not phonating and opens while sufficient air pressure is directed

through the valve from the trachea when the patient covers his stoma during speech. The strength of the magnetic valve may be varied according to the needs of the patient.

The outer skin of the prosthesis, made from CNT-PDMS nanocomposite, is interchangeable and has a patient-specific geometry. The Young's Modulus and Poisson ratio of the base material PDMS (Sylgard® 184 Silicone Elastomer) in 10:1 ratio are 2.60MPa and 0.45, respectively (Mata 2005, Schneider 2009), which are closely matched to that of the tracheal wall (Trabelsi 2010). Carbon nanotubes added to the polymer can significantly enhance the mechanical properties of the scaffold (Khan 2013, Thostenson 2003) to mimic that of the surrounding trachea-esophageal wall tissue. This yields a more uniform stress distribution around the fistula and a better fit of the prosthesis. The removable CNT-PDMS skin also allows patients and clinicians to conveniently swap between shapes and sizes to cater to changing fistulas. In addition, the biocompatibility of CNT-PDMS, which is in contact with surrounding tissues, has been proven in several literatures (Ha-Chul 2012, Sepulveda 2013, Zhou 2012) and was verified in our previous work (Chua 2013).

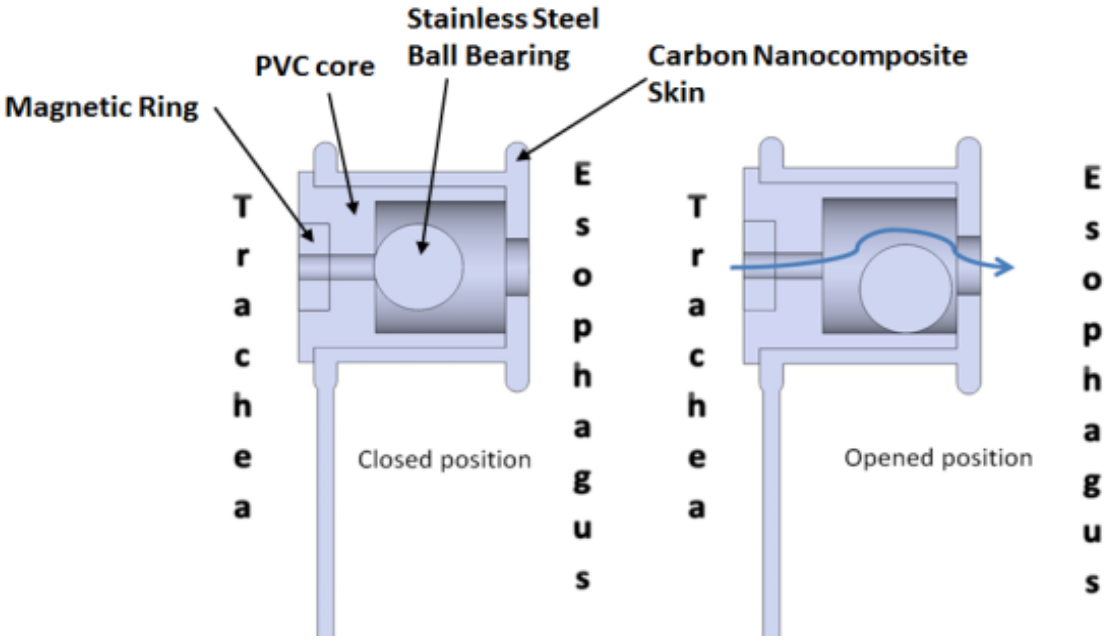

Figure 6.1: Overview of the designed voice prosthesis, its components and the working mechanism.

6.2.2 Computer Aided Design Methodology

The design of the voice prosthesis is paramount in enabling the patient to speak with minimal effort, while preventing leakages of liquid from the esophagus into the trachea. Since fistula dimensions vary in individuals, there is a need to design patient-specific prosthesis to address the problems of leakages and misfit. A process flowchart based on CAD and simulation is proposed in Figure 6.2. Firstly, through CT imaging of the transverse section of the patient's trachea, the thickness of the tracheoesophageal wall is identified and extracted (Figure 6.3) to determine the length of the required prosthesis and the depth of the fistula-tissue model. The shape of the patient's fistula may be captured via photography through the stoma, enabling one to design the cross section of the prosthesis skin model accordingly. This method of photography is only applicable for patients with matured fistulas (>1 month) that has visibly enlarged and changed in shape

and size overtime. The design model is then analyzed in multi-physics simulations and evaluated before 3D-printing fabrication.

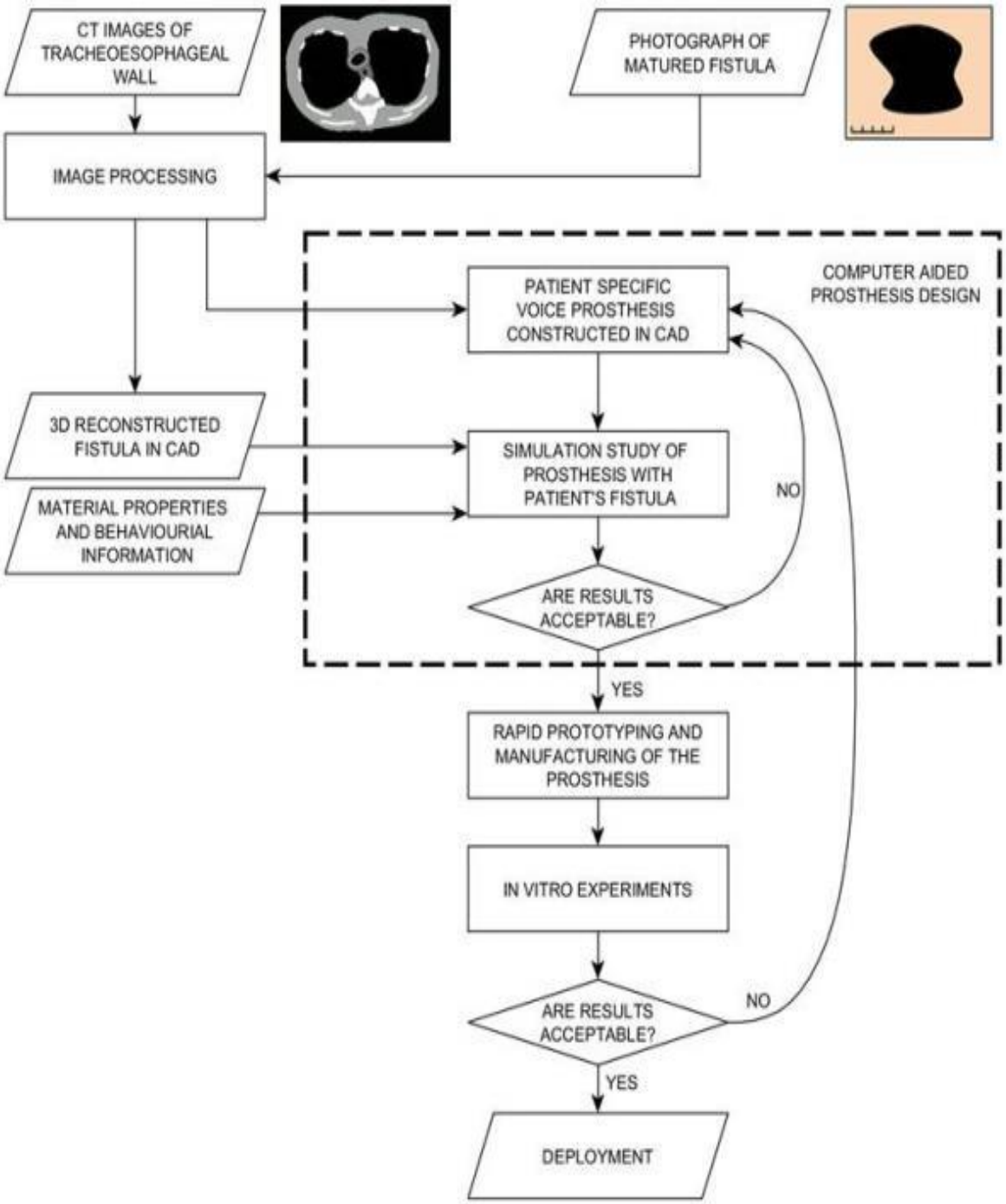

Figure 6.2: Proposed computer aided design process for the development of a new patient-specific voice prosthesis based on CT images and photos from the patient.

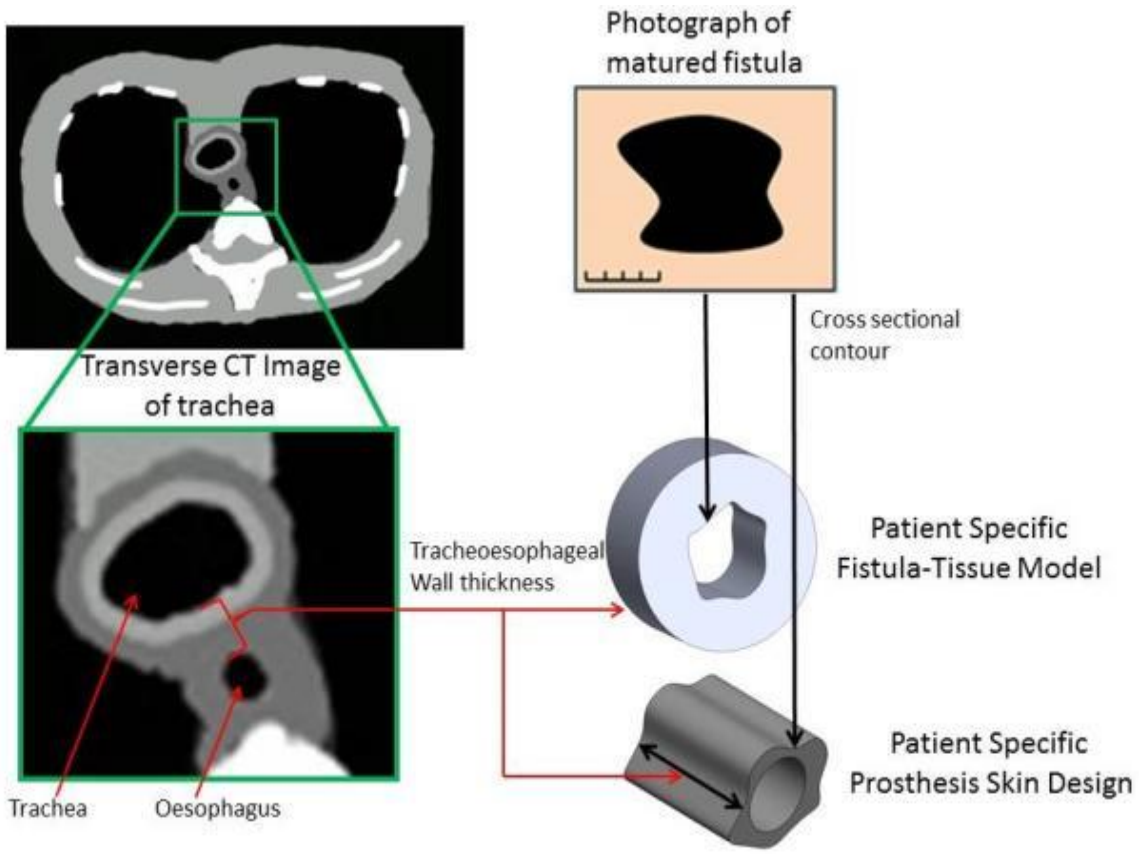

Figure 6.3: Graphical illustration on how the dimensions of the patient-specific fistula-tissue model and the prosthesis skin model are derived from the acquired transverse CT image of the trachea and the photograph taken of the matured fistula.

6.2.3 Simulation

Two different computational simulations were performed with the aim to evaluate the patient-specific design methodology and to optimize the flow design parameter. In the first simulation, stress analysis was carried out for patient-specific and a regular cylindrical prosthesis designs in order to determine the effect of design on stress outcomes (Figure 6.4). Lesser mechanical stress and trauma in the surrounding tissues is desirable as it may reduce tissue irritation and fistula widening. The prosthesis and fistula-tissue models were assembled in COMSOL Multi-physics® (Figure 6.5) and their respective material parameters assigned. The trachea-esophageal wall was modeled as a linearly elastic (Trabelsi 2010) and orthogonal behavioral material with different material

properties in all three principle axes according to the values from Sarma *et al*. (2003) as shown in Table 6.1. Inwards radial stresses ranging from 1.5kPa to 9kPa were applied on the tissue to simulate real life tissue compression by the inserted voice prosthesis and the von Mises stress distribution in the tissue was examined (Figure 6.6). The second simulation study involves computing the pressure change against airflow rate of the prostheses using the flow module in COMSOL Multi-physics®. The purpose is to analyze the airflow resistance of the proposed voice prosthesis design for different inner diameters. Smaller diameter prostheses are desirable due to reduced trauma on the surrounding tissues, but flow resistance increases with decreasing diameter. Therefore the purpose of this study is to determine the smallest diameter for the design, while ensuring that flow resistance is kept reasonably low for ease of phonation by the patients. Briefly, CAD models of the proposed magnetic ball bearing valve of inner minimum diameters of 1mm, 2mm, 3mm, 4mm and 5mm were prepared. This inner diameter range is selected based on the smallest outer diameter of 16 Fr (approximately 6mm) of the Blom-Singer voice prosthesis available. The 1mm increments in the inner prosthesis diameter were utilized according to our fixed magnetic ball bearing valve sizes available. The first pressure probe was positioned at the entrance of the tracheal side while the second one at the esophageal side (Figure 6.7). Air flow rates within the human speaking range, 50mL/s to 300mL/s, were simulated in the prosthesis models and the pressure readings recorded. The flow simulation was taken to be a one-way fluid-mechanical interaction as the highly rigid prosthesis core does not undergo any changes at the stipulated airflow range.

TABLE 6.1

Mechanical property values of the trachea-esophageal wall

Trachea-esophageal Mucosa Wall Material Properties		
E_{xx}(longitudinal)=0.36MPa	G_{xy}=0.124MPa	υ_{xy}=0.45
E_{yy}(transverse)=0.3MPa	G_{xz}=0.124MPa	υ_{xz}=0.375
E_{zz}(radial)=0.3MPa	G_{yz}=0.124MPa	υ_{yz}=0.375

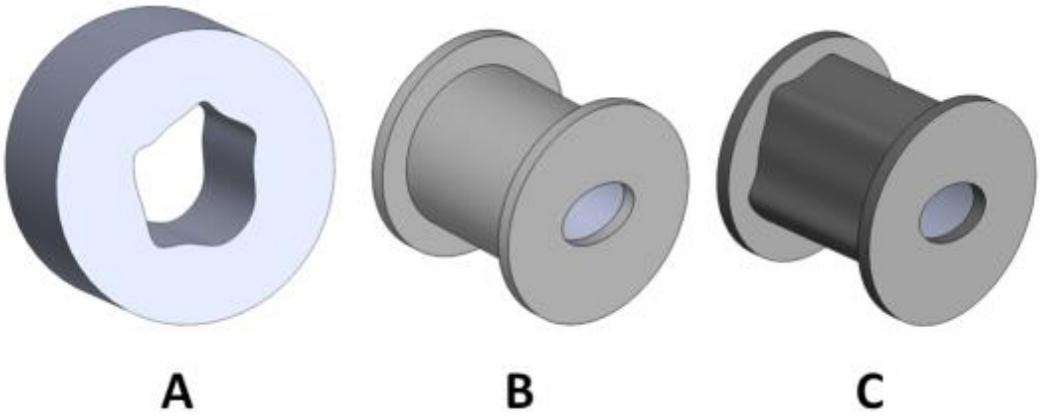

Figure 6.4: Constructed CAD models of (A) Patient's fistula, (B) Uniform Cylindrical Voice Prosthesis and (C) Patient-Specific Voice Prosthesis.

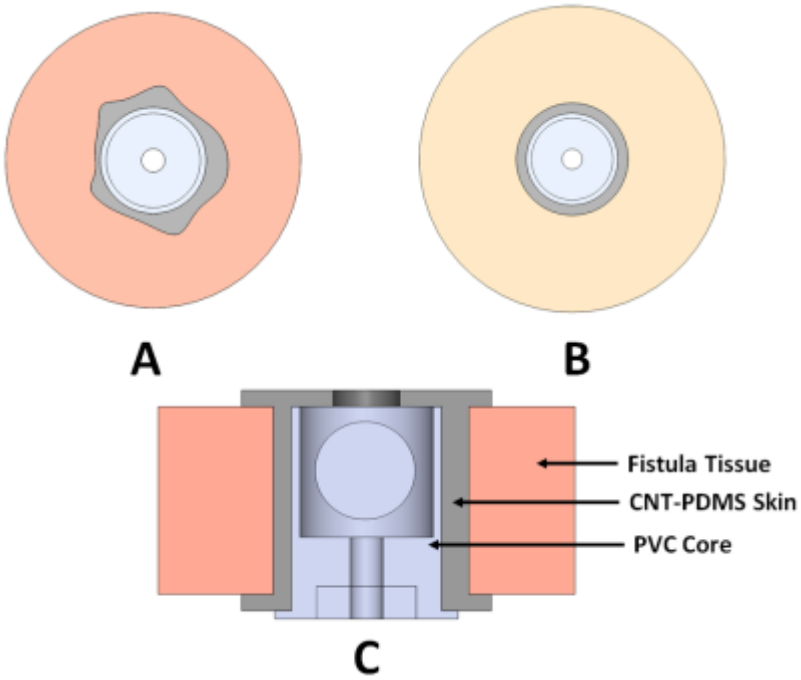

Figure 6.5: Position of the voice prosthesis in fistula in the multi-physics simulation. (A) Lateral section of the patient-specific voice prosthesis - tissue assembly, (B) uniform cylindrical voice prosthesis – tissue assembly. (C) Longitudinal section of voice prosthesis- tissue assembly.

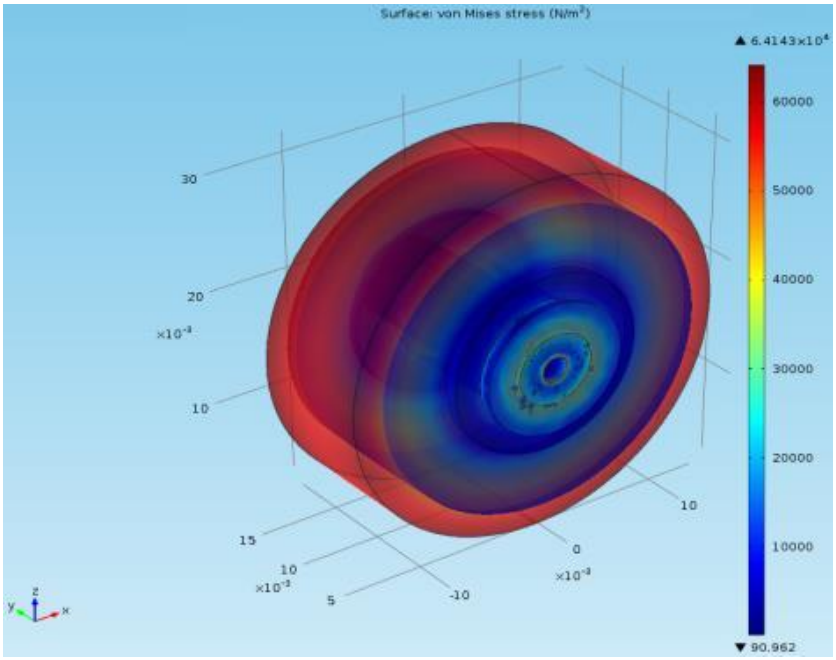

Figure 6.6: Radial compression on the prosthesis-tissue assembly to analyze the stress distribution in the fistula tissue.

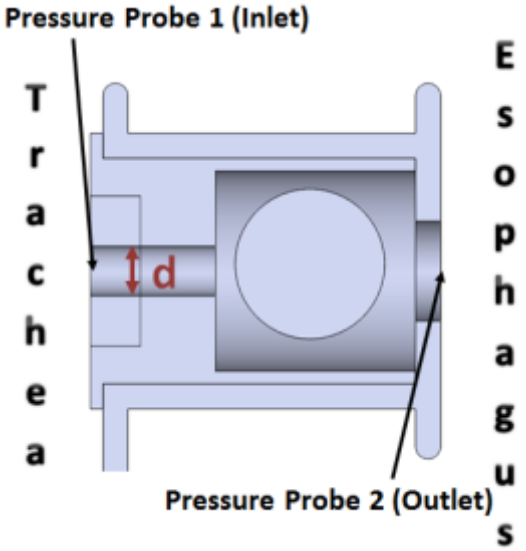

Figure 6.7: Cross section of the proposed voice prosthesis with the indicated positions of the two pressure probes. The location of the minimum diameter is denoted by *d*.

6.2.4 Fabrication

A sacrificial mold for the CNT-PDMS skin was designed according to the patient-specific dimensions and fabricated via rapid prototyping using Objet Eden350™ (Stratasys, Asia) and material Fullcure®950 TangoGray (Figure 6.8). Sylgard 184™ pre-polymer was combined with its curing agent in a 10:1 ratio and thoroughly mixed with a controlled amount of carbon nanotubes to obtain a Young Modulus similar to that of the membranous trachea-esophageal wall. The mixture was then carefully poured into the mold and left in a vacuum for 1 hour. This facilitates the removal of any air bubbles that could affect the mechanical integrity of the composite. After degassing, the mold was left in an oven to cure for 24 hours at 100°C. Fabrication of the fixed rigid PVC core was done through precision machining of a piece of PVC cylinder. Magnetic rings and ball bearings (Misumi, Singapore) were then mounted into the rigid core. The final products were subjected to UV sterilization before use and are shown in Figure 6.9.

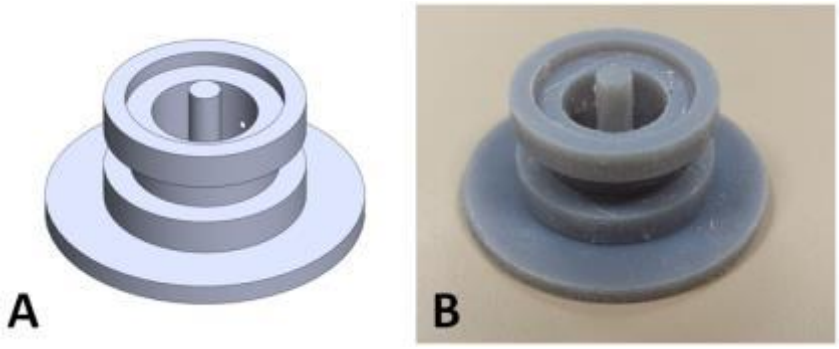

Figure 6.8: (A) Patient-specific voice prosthesis mold designed in CAD software. (B) Rapid prototyping of the sacrificial mold to fabricate the carbon nanocomposite skin.

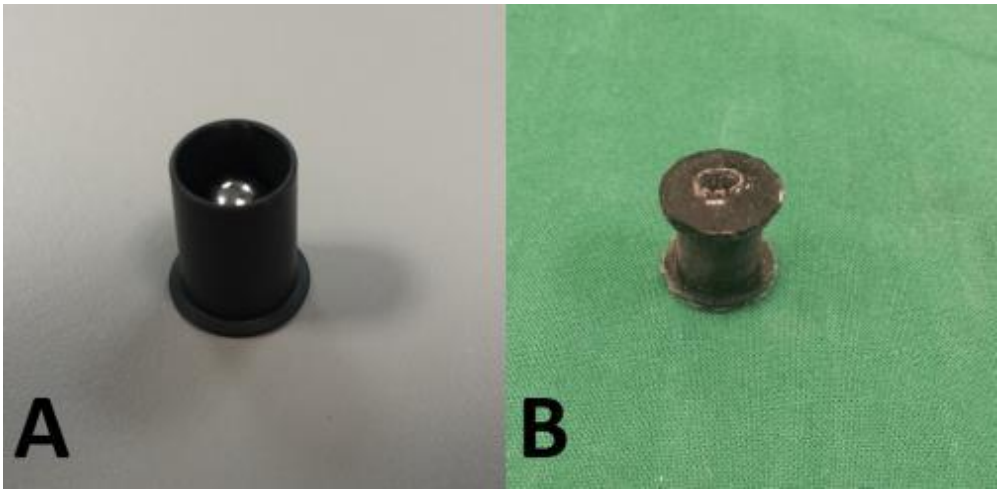

Figure 6.9: Final fabricated products. (A) PVC inner core and ball bearing. (B) Assembled prosthesis with carbon nanocomposite skin.

6.2.5 *In-Vitro* Experiment

In-vitro and *in-vivo* experiments were carried out to study and evaluate the prosthesis functionality and the effectiveness of the proposed patient-specific CAD process. Since the operational performance of the developed prosthesis is difficult to evaluate in animal models due to issues on ethical animal handling, the *in-vitro* tests serves to demonstrate the workability of the proposed prosthesis as an effective valve.

The purpose of the *in-vitro* experiment is to evaluate the performance of the proposed magnetic ball bearing valve by studying the forward flow characteristics of the developed magnetic ball bearing voice prosthesis and the reverse flow characteristics.

The forward flow characteristic is the air flow resistance through the prosthesis and it determines the ease of speech for patients. The reverse flow characteristic is the relationship between the amounts of leakage through the prosthesis in the reverse direction with increasing pressure from the esophageal side (Belforte 2002).

A specially constructed testing apparatus was prepared for measurement of forward flow characteristics (Figure 6.10). Air supply was provided by a motorized air pump with an onboard variable flow valve, R, which could vary the amount of air flow. F represents the electronic flow meter (PFMB7201S-C8-A-M, SMC Singapore) which measures and displays the rate of air flow through it. A specially constructed acrylic pressure chamber, C, which is leak proof and houses the prosthesis, V, was fabricated. P is the pressure transducer (ISE40A-C6-X-M, SMC Singapore) that is connected parallel to the pressure chamber and effectively measures the air pressure in the chamber. The pressure change across the prosthesis can be determined by subtracting atmospheric pressure from the measured pressure. Flow rates between 50mL/s to 300mL/s were used, which were within the normal range of human air flow recorded during speech (Grolman 2007). The air flow resistance results were then tabulated and compared with other voice prostheses from literature.

An experimental setup was designed and prepared to measure the reverse flow characteristics of the prosthesis (Figure 6.11). It is paramount to assess the reverse resistance as it determines the tendency of fluid to leak from the esophagus to the trachea through the prosthesis, which could result in pneumonia. The esophageal part of the valve was subjected to dynamic pressures of 10kPa, 20kPa and 30kPa for 30 seconds each before measuring the weight of water that leaks through the valve into the beaker.

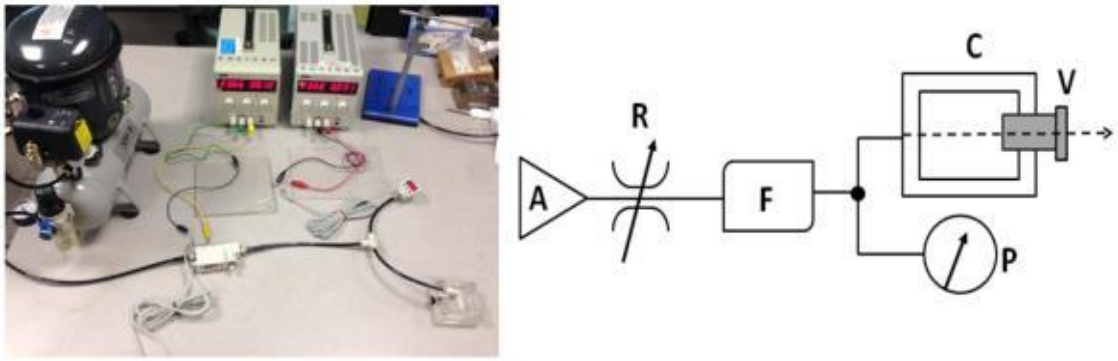

Figure 6.10: (Left) Test rig for forward flow characteristics measurement. (Right) Schematic of the setup where A is the air pump input, R is the variable flow valve, F is the electronic flow meter, P is the pressure transducer, C is the pressure chamber and V is the voice prosthesis.

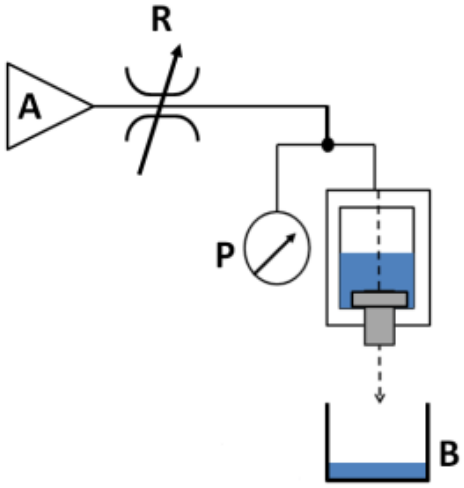

Figure 6.11: Test rig designed for reverse flow characteristic measurement.

6.2.6 *In-Vivo* Experiment

In-vivo studies on porcine models were conducted to verify the accuracy and feasibility of the patient-specific CAD methodology for voice prosthesis. This is done through the fabrication subject-specific voice prosthesis using CT data of the pigs and implanting them *in-vivo*. The experiments were performed according to an approved Institutional Animal Care and Use Committee protocol (IACUC No: 018/09). Briefly, five healthy female pigs weighing around 60kg were anaesthetized and CT-scanned in both the transverse and sagittal planes. The CT images were used to estimate the length

required between the prosthesis flanges for a good fit (Figure 6.12). The animals were then placed in a supine position on the operating table. A longitudinal midline neck incision was made using a mono-polar diathermy blade and the skin and muscles were laterally retracted to expose the trachea. Following which, a rectangular piece was longitudinally incised from the top portion of the trachea to expose the inner lumen. At this point, the endotracheal tube was immediately retracted from the mouth and reinserted into the end of the trachea directly to intubate the pig (Figure 6.13). A puncture through the trachea-esophageal wall was made using our previously developed Measurement And Insertion Device (MAID), which allows for primary in-office voice restoration (Lau 2014). The fabricated voice prostheses models based on the individual animal's tracheoesophageal wall thickness were then carefully inserted into the fistula using the MAID. Once in position, the prostheses were left implanted for 30 minutes, during which careful inspection and evaluation were carried out to ensure a good fit.

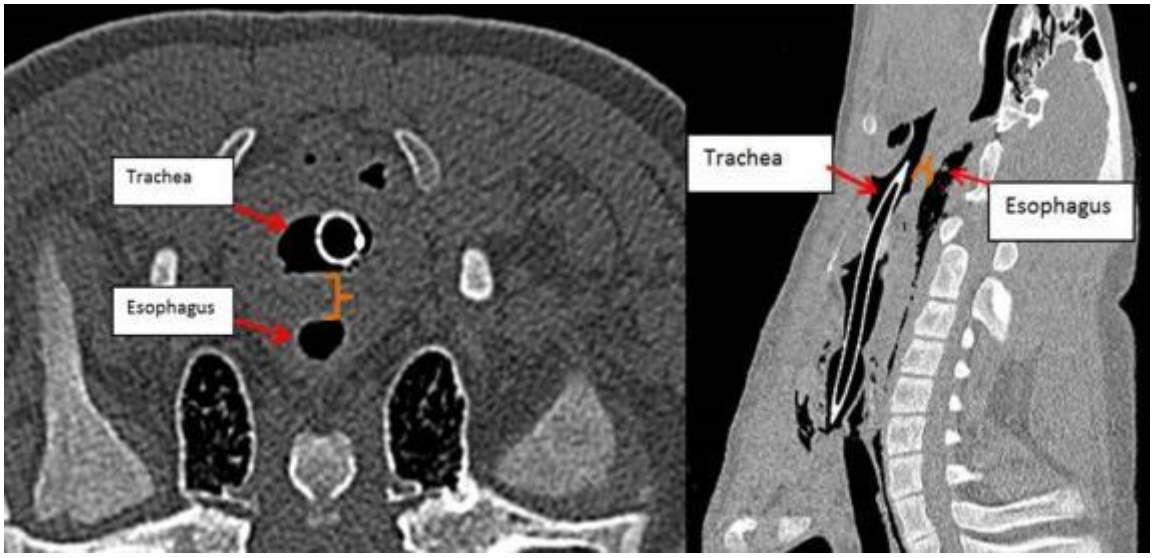

Figure 6.12: Pre-surgical (Left) Transverse and (Right) Sagittal CT images of the pig with the positions of the trachea and esophagus labeled. The orange bracket denotes the thickness of the tracheoesophageal wall measured to estimate the length of the voice prosthesis model to be constructed and fabricated.

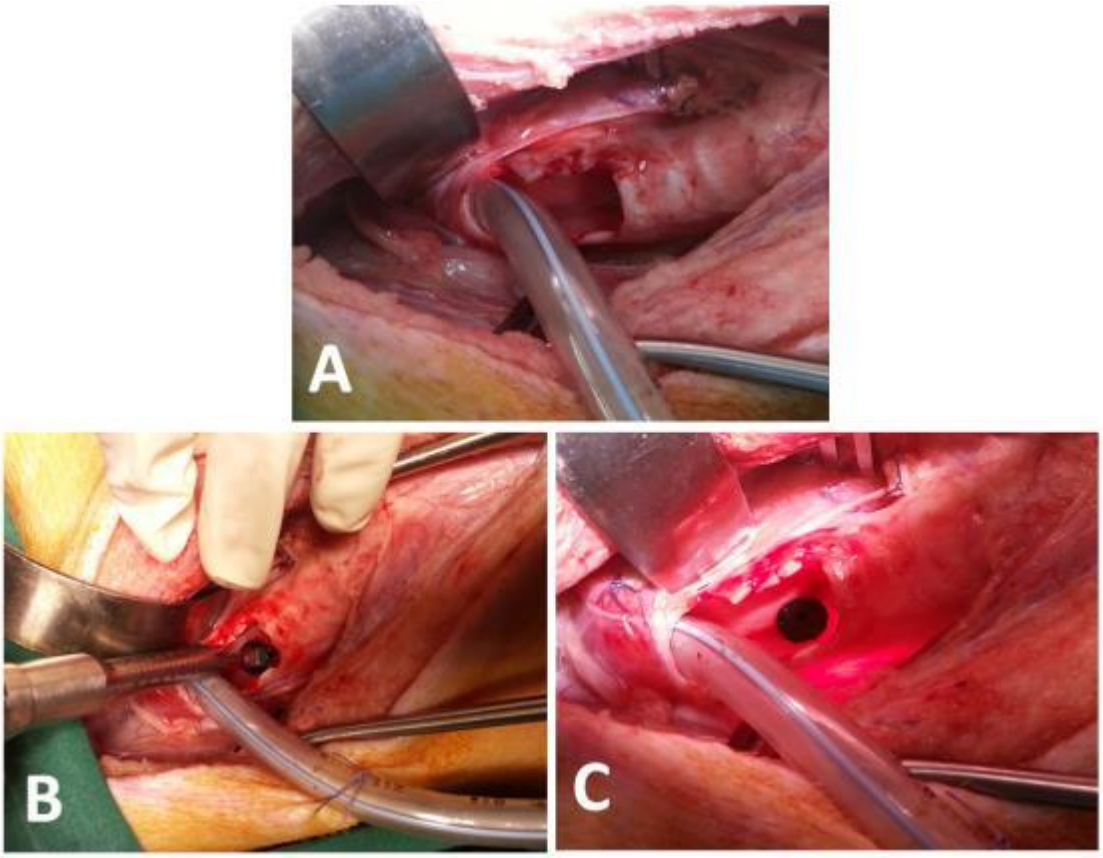

Figure 6.13: Insertion of carbon nanocomposite voice prosthesis into live pig models. (A) Endotracheal tube inserted into lower end of trachea to maintain ventilation and anesthesia. (B) Puncture and insertion of prosthesis using the MAID. (C) Voice prosthesis in position.

6.3 Results

6.3.1 Simulation

From the first simulation study, the von Mises stress values in the fistula tissue were recorded for both uniform design and patient-specific design voice prostheses under various radial compressions. From Figure 6.14, it can be seen that a patient-specific design will result in lower minimum and maximum stress values in the surrounding tissues for different radial compression values. This may be attributed to a better fit of the prosthesis in the fistula hence resulting in an even stress distribution around the tissue as

observed from the smaller difference in maximum and minimum stresses. The matching geometry between prosthesis and the fistula also led to greater reduction in maximum stress as increasing radial compression is exerted. Although it is hard to derive absolute stress values from the first simulation study and verify them, this process serves to compare the relative performances of tissue stress concentration between patient-specific and modular designs.

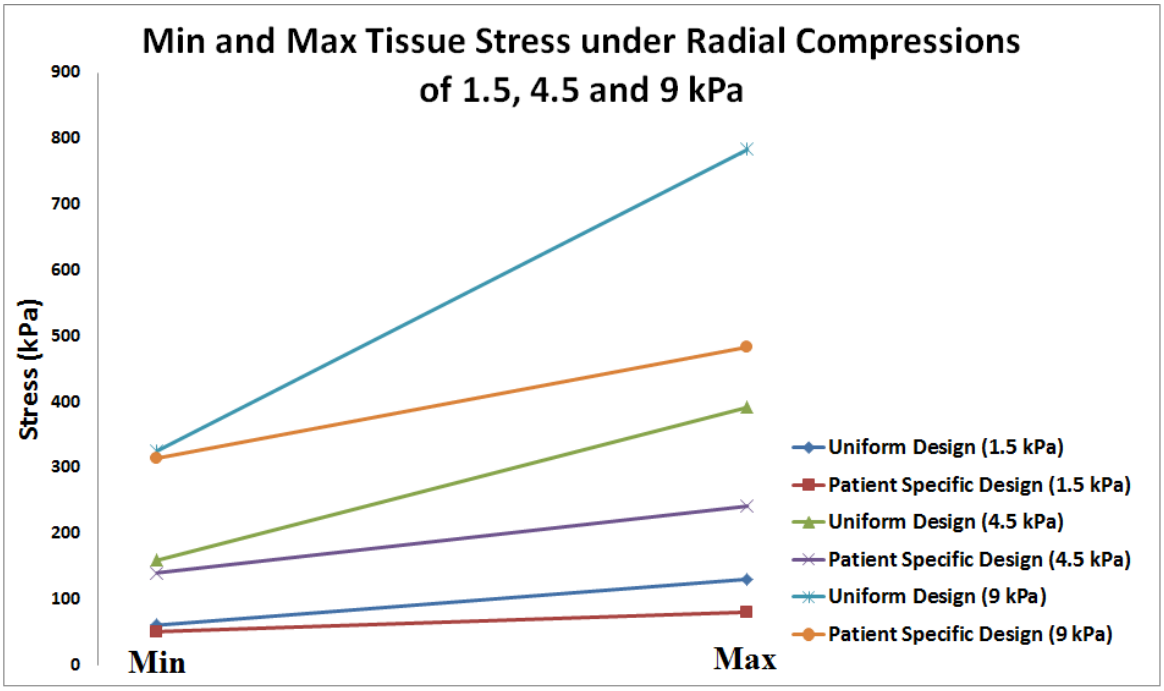

Figure 6.14: Graph comparing the minimum and maximum stress in the surrounding tissues for uniform and patient-specific design under radial stresses of 1.5, 4.5 and 9 kPa.

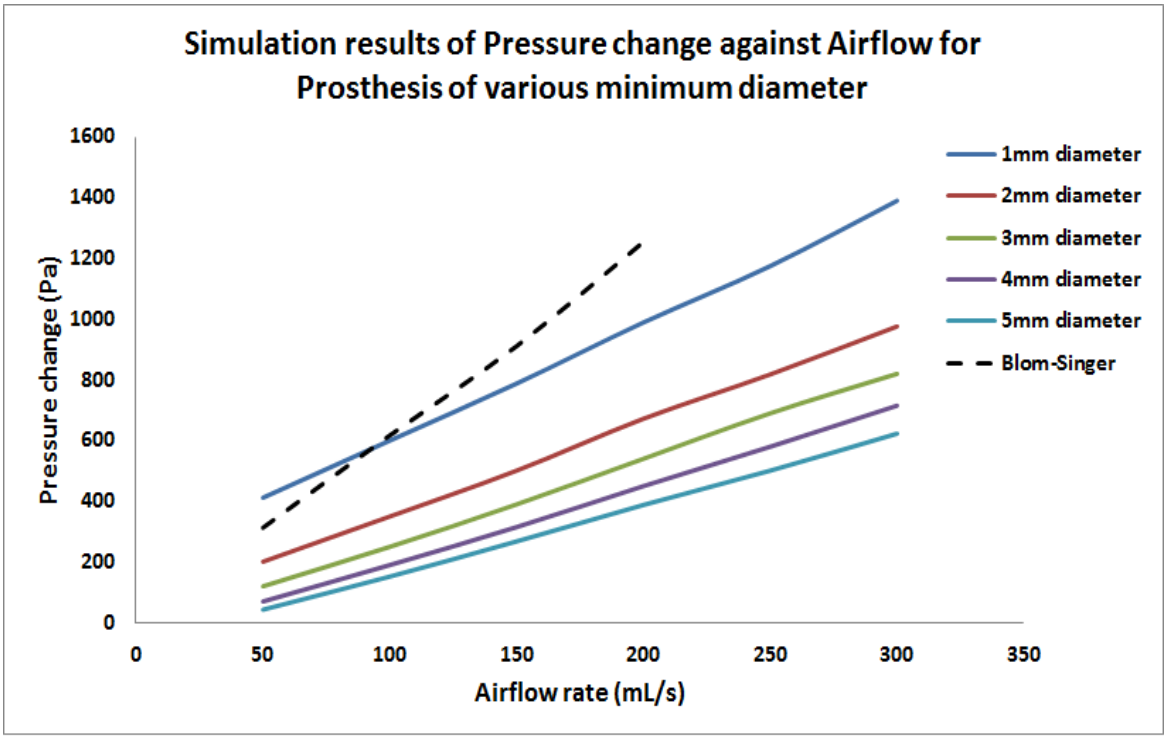

Figure 6.15: Graph presenting the pressure change against airflow rate for the proposed prosthesis of various minimum diameters. The dotted line is denotes the *in-vitro* airflow resistance characteristics of the current Blom-Singer voice prosthesis, which serves as the benchmark.

The results from the second simulation study on the air flow resistance for voice prostheses of different inner minimum diameter was tabulated and plotted (Figure 6.15). The resistance of the prosthesis at a particular airflow rate is the ratio of pressure change to airflow rate. The Blom-Singer voice prosthesis was selected as the bench mark for design as it is one of the most widely used in Europe and Singapore. From the results, optimal inner diameter would be 2mm as it is the smallest diameter for which airflow resistance is less than the Blom-Singer prosthesis. Through this process of CAD and simulation analysis, the designs of the medical device can be optimized easily and efficiently.

6.3.2 *In-Vitro* Experiments

For the first *in-vitro* experiment, each airflow rate was repeated 10 times and the change in pressure measured. The results of the pressure change against volumetric flow rate across the carbon nanocomposite voice prosthesis was plotted in Figure 6.16 and also compared with other types of voice prostheses from literature (Ben 1989) in Figure 6.17. The forward flow resistance of the prosthesis is the gradient of the pressure change - flow rate graph. It is observed (Figure 6.17) that the developed voice prosthesis has a lower gradient amongst the other prostheses presented and therefore a lower forward flow resistance. A low forward flow resistance implies ease of speaking in patients since high resistance would mean more effort in speaking. In the second experiment which determines the reverse air flow characteristics, the average water leakage was collected, weighed and tabulated into a graph (Figure 6.18). It was established in literature that the average person can cough out about 0.3g of fluid from the airway (Belforte 2002) without causing any airway complications. From Figure 6.18, the leakages measured through the proposed prosthesis valve throughout all 3 pressure values are less than 5% of the critical amount of 0.3g. Thus, the design has demonstrated its ability to achieve relatively lower forward flow resistance while having good backward leakage resistance through these two experimental studies.

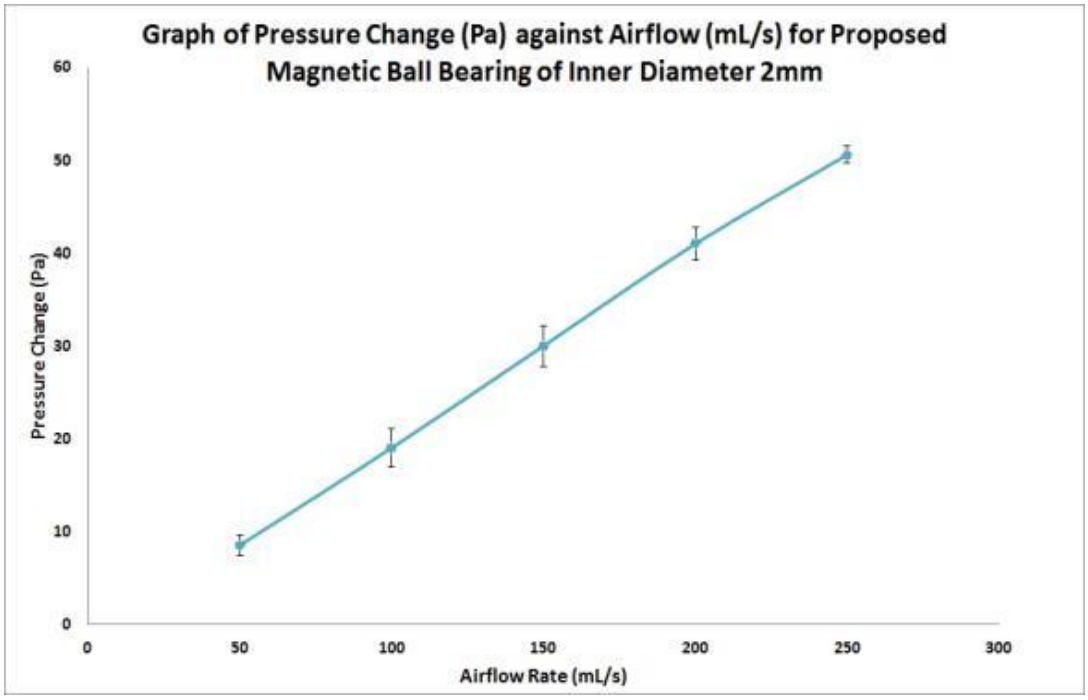

Figure 6.16: Measured airflow resistance for the proposed magnetic ball bearing prosthesis design of inner diameter 2mm. 10 runs were performed for each airflow rate test point and the average results and standard deviation tabulated.

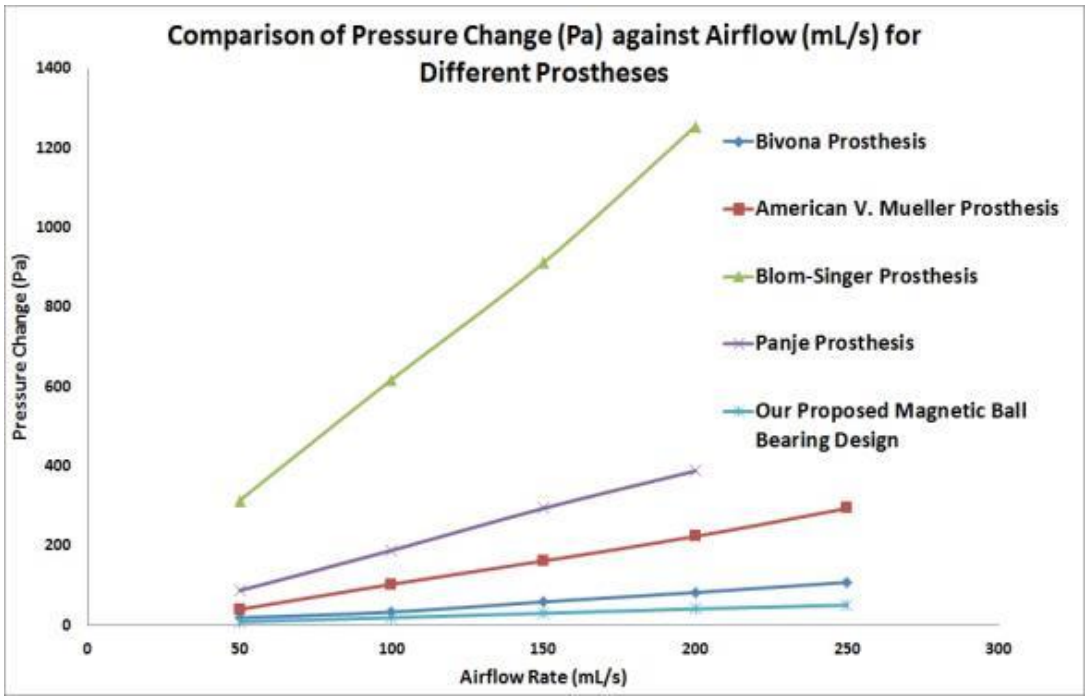

Figure 6.17: Comparison of pressure change versus airflow for different prostheses in literature and the proposed prosthesis.

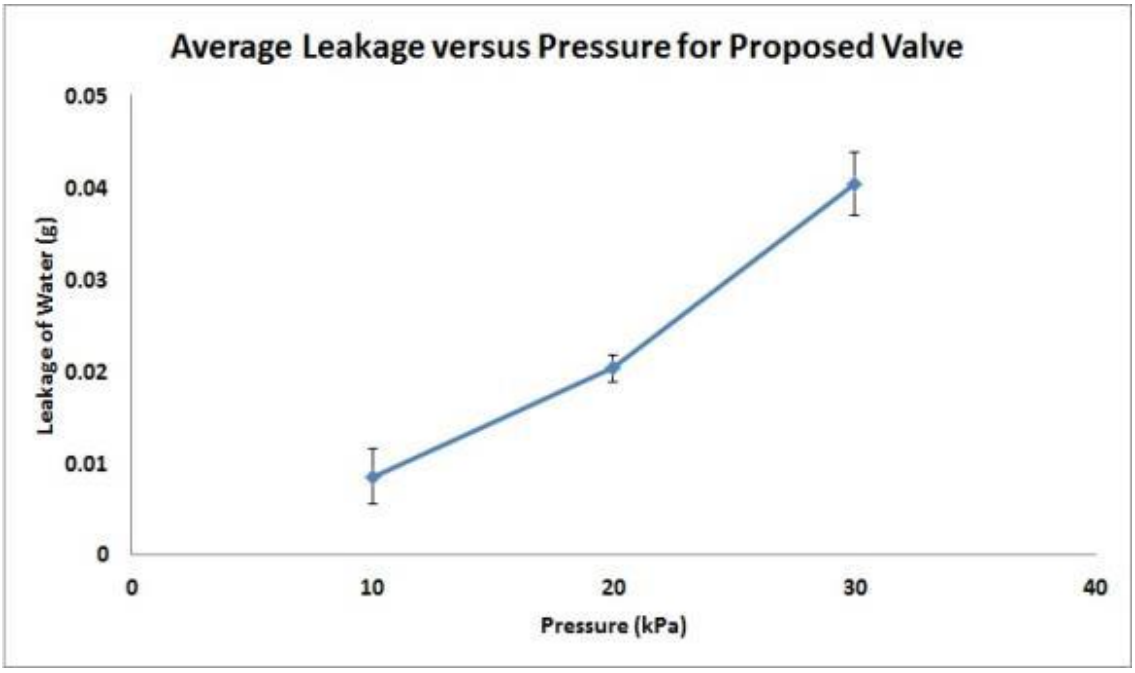

Figure 6.18: Average water leakage measured over 30 seconds versus pressure for proposed magnetic ball bearing prosthesis valve. Each pressure test point was performed 10 times for better accuracy.

6.3.3 *In-Vivo* Experiments

With the performance of the magnetic ball bearing valve evaluated through the *in-vitro* experiments, the successful *in-vivo* experiment has verified the feasibility of the use of CAD in the development of patient-specific voice prosthesis. Based on our experience with the sizing outcome during initial implantations which resulted in a shorter than required prosthesis length, a positive tolerance of around 2mm for the length was subsequently factored in for a good fit. This may be attributed to the angle of approach in the puncturing of the fistula, resulting in a longer fistula tract compared to the thickness of the wall itself. However, this limitation can be easily overcome via insertion of a dilator into the fistula prior to CT imaging for patients undergoing in-office secondary voice prosthesis insertion or those with matured fistulas. The dilator will be able to reveal clearly the actual length and position of the fistula tract on the CT images.

The second set of implanted prostheses, with the length tolerance factored in, displayed better fit in the animals. Forceps were used to grip and tug at prosthesis flanges to ensure that there was no sliding along the fistula tract and that the flanges rested securely on each end of the wall. Water was flushed down the esophagus using the Pentax EG-2930K endoscope (Pentax, Singapore) and inspection for any leakages from the esophagus into the trachea was done, to which there was none. The animal experiments has successfully demonstrated that CAD of the prosthesis based on patient's imaging data is a viable option and can accurately predict the dimensions of the prosthesis required for fabrication. The voice prosthesis will be tested in human trials in future to further assess the quality of use in patients, which includes speech.

6.4 Discussions

The proposed method of computer aided design of voice prosthesis based on patient-specific data has brought several advantages over the conventional voice prosthesis. The conventional method uses standard sizes and shapes of prosthesis. It has been reported clinically that these standard sizes and shapes do not accommodate for more than 28% of patients whose tracheoesophageal fistula size lies beyond the standard range of prosthesis sizes available, thus resulting in periprosthetic leakages and potential complications (Blom 2003). This number is set to increase due to the gradual exacerbation of fistula dilation from prosthesis weight and mechanical trauma over time. Currently, patients who are unable to find a matching prosthesis size because of excessive fistula size, have to undergo surgery to reduce the size of the hole. Our methodology of patient-specific computer aided design can create customized voice prosthesis accurately to match any tracheoesophageal fistula sizes. Furthermore, from the reduction in

mechanical stress concentration in the surrounding tissues as presented in our simulation, we believe that this may retard the formation of granulation tissues and fistula widening in patients. However, this remains to be studied and verified in future works.

The proposed design methodology has significantly improved the effectiveness of new voice prosthesis. It is important to customize the design processes with computer simulation specific to the device and its clinical application. The resultant design of our device has overcome the transprosthetic and periprosthetic leakages that are common in existing voice prostheses by offering accurate customization. Patient-specific implants will typically cost more than a one-size-fits-all device. However, we have learnt from our experience with the development of patient-specific prosthesis that a patient-specific device can also be cost effective especially for low volume implant devices.

The methodology of the development of patient-specific carbon nanocomposite voice prosthesis has been proposed in this chapter. CAD was the key feature embedded within the developmental process that encompassed user-centric designing, multi-physics simulations and rapid prototyping of the device. This is the first time that a CAD process is developed specifically for voice restoration. Simulation results have indicated that a patient-specific design can yield better stress reduction in the surrounding tissues, thereby reducing fistula widening. The *in-vitro* experiments have proven the functionality of the prosthesis novel magnetic ball bearing valve, which has a relatively lower forward flow resistance compared to other prostheses and a strong backflow resistance against transprosthetic leakages. Lastly, the effectiveness of the patient-specific CAD process of the voice prosthesis was evaluated in five porcine models and verified. Additionally, the effectiveness of the new voice prosthesis has been improved due to the proposed design

methodology. Future refinements will be made on this prosthesis, including augmentation of the carbon nanocomposite material to yield a more natural speaking tone and conducting of clinical trials with human subjects.

Chapter 7

CONCLUSION AND FUTURE WORK

This chapter summarizes and outlines the main contributions of this thesis in the field of carbon nanocomposites and patient-specific ENT implants. The limitations of our works and subsequent future works in this research are discussed in Section 7.2.

7.1 Conclusion

A predictive model for the attenuation of sound waves through CNF and CNT based composites was proposed. The model explores the nano-scale conditions by taking into consideration the Rayleigh scattering function, absorption, resonance and interfacial friction of the dispersed inclusions within the matrix to compute the overall damping characteristic. The results were validated against experimental data obtained from ultrasonic testing and measurement of sound wave attenuations through composites of varying weight fraction of inclusion. Although many experimental works were performed to characterize the attenuation through nanocomposites, the proposed model in this thesis provides a physical explanation to the attenuation of the nanocomposite materials at the nano-scale level, while allowing computation of the results from input of existing material properties and weight fractions of the nano-inclusions. This provides a quick and accurate model for attenuation prediction and optimization of material parameters for ENT implant design.

A probabilistic predictive model for the mechanical properties of carbon nanocomposites was proposed and validated in this thesis. The model was able to

circumvent the limitations of current constitutive models by taking into consideration the probabilistic outcome of the fabricated material based on initial experimental data acquired. The algorithm was based on a modified surface response methodology coupled with MC method. The results from the probabilistic regression equations were validated with more experimental work and FE simulations. The application of the proposed model was also demonstrated in the design and evaluation of a carbon nanocomposite tracheal implant model. This method provides a more realistic probabilistic based outcome compared to deterministic approaches in the modeling of nanocomposite materials.

A patient-specific carbon nanocomposite tracheal prosthesis is also proposed and investigated. *In-vitro* experiments were performed to evaluate the ability of the CNT-PDMS material to host the proliferation and ciliogenesis of tracheal epithelial cells. Simulation results also indicate that the patient-specific design resulted in a more even distribution and lower levels of stress concentration throughout. Finally, the implantation of the developed tracheal prosthesis yield promising outcomes as the regeneration of the ciliated epithelium was achieved within a span of 2 weeks compared to the reported time of 4-8 weeks in literature. This patient-specific tracheal prosthesis can provide a timely solution for airway replacements in patients with advanced tracheal carcinoma. The similarity in mechanical properties and biocompatibility of the CNT-PDMS nanocomposite may be further applied in other areas like cartilage replacement and even soft bone tissues repair.

New CAD methodology based on patient's CT imaging data, simulation-based evaluations and rapid prototyping to develop the world's first patient-specific carbon nanocomposite voice prosthesis was investigated. The patient customized prosthesis is

made from CNT-PDMS, which possesses similar material properties to the surrounding trachea-esophageal wall. CAD and simulation of the prosthesis is based on acquired patient's CT images to customize its design. *In-vitro* flow experiments indicated lower flow resistance compared to other types of prostheses and verified its workability. Lastly, the feasibility of the patient-specific CAD methodology was evaluated in porcine model. This proposed design methodology for voice prosthesis eliminates the need for surgical correction to seal oversized fistulas and unnecessary multiple insertions due to incorrect misfit of voice prosthesis. Patients can also enjoy a better quality of life as transprosthetic and periprosthestic leakages are reduced.

Specific contributions in this thesis include:

1. A patient-specific framework for optimizing ENT implants using patient's CT data and simulation-based design;
2. An attenuation model for nanocomposites that includes the energy dissipation by the inclusions and interfacial friction and
3. A probabilistic-based predictive modeling of nanocomposite for engineering design processes.
4. The development of CNT-PDMS trachea and voice prosthesis that is superior to the state-of-the-art; and
5. New knowledge of the behavior and proliferation of tracheal epithelial cells on CNT-PDMS material both *in-vitro* and *in-vivo*;

7.2 Future work

The characterization and prediction of attenuation in carbon nanocomposite in Chapter 3 requires future work to refine its mathematical model. The model proposed in this thesis can only predict effectively at low weight fractions of inclusions as shown from experimental data. Further investigation of this model will include experiments conducted at high weight fractions to evaluate its accuracy. This is necessary as the direction to develop ultra-thin (<1mm) tracheal scaffolds would require high densities of continuous CNT fibers within the polymeric matrix to enhance its strength and mechanical properties. Such a scaffold would allow for faster vascularization and regeneration of the ciliated epithelium, while invoking less foreign body response. Future work will hence involve utilizing both the attenuation predictive model and the proposed hybrid stochastic degradation model in the design process to optimize the tracheal prosthesis. In addition, the attenuation experiment involving harmonic sound waves of 200Hz and 1000Hz is not fully representative of the full human harmonic range of 20Hz to 20,000Hz *in vivo*. Hence, further experimental validation of the model with the full harmonic range will be required.

In Chapter 4, a potential limitation of the proposed predictive model is that it may reduce in accuracy as the input strain and CNT weight fraction values deviate further away from those used in the initial experimental data. Future studies will include investigating the accuracy of the model at much greater variable values and modifying the algorithm. Another limitation may be the inadequacy of the normal distribution to represent the scattered stress-strain experimental data, which has resulted in slight deviation of the predicted model from the experimental study. Future works will include

exploring the use of beta distributions (McDonald 1995) to better represent the stress-strain data and hence improving the quality of results.

In the development of a patient specific tracheal prosthesis in Chapter 5, a limitation of the proposed device is its definite default shape, which results in its inability for structural reconfiguration in accordance to dimensional changes in the native trachea. As such, it will be unsuitable in infants and younger patients whose tracheas significantly increase in size with growth since multiple revision surgeries would be required to swap the smaller prosthesis with bigger ones to avoid airway complications. The majority of the six pigs were able to survive for 2 weeks without any breathing difficulties with complete regeneration of the epithelium. However, there were signs of stenosis occurring around the end of the 2^{nd} week mark at the site of anastomosis and all pigs did not survive past 2 weeks. The possible causes of the anastomosis might be due to inconsistent surgical technique, infection of wound site or even material and design incompatibility. This issue requires further investigation as other studies in literature face similar limitations. Longer end points will be required in future to fully evaluate the implications of the proposed carbon nanocomposite tracheal prosthesis before human trials can begin. Furthermore, other non-invasive imaging techniques will be explored to capture the time dependent *in-vivo* scaffold degradation and tissue regeneration process for better understanding. The current use of discontinuous carbon nanotubes scattered in the polymer matrix may not be the optimal configuration in terms of mechanical properties. Edwards *et al.* has studied the use of a continuous carbon nanotube yarn in nanocomposite scaffolds, and the conclusion was that the fiber continuity fully retained

the CNT electrical and mechanical properties (Edwards 2009). Future work may include the use of continuous carbon nanotube yarn within the nanocomposite matrix to allow for the development of thinner and stronger prostheses.

With regards to the future improvements of the patient-specific voice prosthesis in Chapter 6, manipulation of the CNT-PDMS material configuration, like alignment, to recreate artificial vocal folds with the prosthesis for improved speech quality will be carried out. Currently, the quality of speech produced by voice prosthesis is monotonous and unnatural. The enhanced elastic property of the carbon nanocomposite can be tapped on to produce biomimetic vocal flaps that would be able to generate a range of pitches based on airflow. Additionally, human trials will be conducted to better evaluate the effectiveness of the patient-specific carbon nanocomposite voice prosthesis since we were unable to test the ability of the porcine models to phonate with the device.

APPENDIX A

List of special terms

1. **Attenuation:** It is a term that refers to the reduction in strength of a signal or energy wave across a distance.
2. **Trachea Ciliated Epithelium:** The outer most surface of the lumen of the airway that consists of finger-like structures called cilia for mucus removal.
3. **Rayleigh Scattering:** The scattering of light or wave energy off the molecules of air or particles about a tenth the wavelength of the wave.
4. **Carcinoma:** A cancer forming from the lining of the internal organ.
5. **Cell Differentiation:** A process whereby a less specialized cell becomes a more specialized cell type.
6. **Tracheo-Esophageal Puncture (TEP):** A surgically created hole between the windpipe and the gullet.
7. **Fistula:** A surgically made hole between a hollow or tubular organ and the body surface or between two tubular or hollow organs.
8. **Epithelialization:** The migration of cells across the surface of the wound to form a barrier between the wound and the environment.
9. **Granulation Tissue:** New connective tissue and tiny blood vessels that form on the surface of a wound or implant during the healing process.
10. **Angiogenesis:** The development of new blood vessels.
11. **Vascularization:** The natural development of vessels in a tissue or implant.

REFERENCES

Adachi, T., Osako, Y., Tanaka, M., Hojo, M., & Hollister, S. J. (2006). Framework for optimal design of porous scaffold microstructure by computational simulation of bone regeneration. *Biomaterials, 27*(21), 3964-3972. doi: 10.1016/j.biomaterials.2006.02.039

Affdl, J., & Kardos, J. (1976). The Halpin-Tsai equations: a review. *Polymer Engineering & Science, 16*(5), 344-352. doi: 10.1002/pen.760160512

Alemani, D., Pappalardo, F., Pennisi, M., Motta, S., & Brusic, V. (2012). Combining cellular automata and lattice Boltzmann method to model multiscale avascular tumor growth coupled with nutrient diffusion and immune competition. *Journal of Immunological Methods, 376*(1–2), 55-68. doi: 10.1016/j.jim.2011.11.009

Azorin, J. F., Bertin, F., Martinod, E., & Laskar, M. (2006). Tracheal replacement with an aortic autograft. *European Journal of Cardio-Thoracic Surgery, 29*(2), 261-263. doi: 10.1016/j.ejcts.2005.11.026

Azuaje, F. (2011). Computational discrete models of tissue growth and regeneration. *Briefings in Bioinformatics, 12*(1), 64-77. doi: 10.1093/bib/bbq017

Baiguera, S., Birchall, M. A., & Macchiarini, P. (2010). Tissue-Engineered Tracheal Transplantation. *Transplantation, 89*(5), 485-491. doi: 410.1097/TP.1090b1013e3181cd1094ad1093.

Barrow, R., Wang, C.-Z., Cox, R., & Evans, M. (1992). Cellular sequence of tracheal repair in sheep after smoke inhalation injury. *Lung, 170*(6), 331-338. doi: 10.1007/bf00177579

Belforte, G., & Carello, M. (2002). Experimental comparison between a Staffieri and a New Prototype tracheo-oesophageal valve. *Medical Engineering & Physics, 24*(7–8), 485-491. doi: 10.1016/S1350-4533(02)00066-8.

Ben Jebria, A., Gioux, M., Henry, C., Devars, F., & Traissac, L. (1989). New prosthesis with low airflow resistance for voice restoration following total laryngectomy. *Medical and Biological Engineering and Computing, 27*(2), 204-206. doi: 10.1007/bf02446231

Benhardt, H. A., & Cosgriff-Hernandez, E. M. (2009). The Role of Mechanical Loading in Ligament Tissue Engineering. *Tissue Engineering, 15*(4), 9. doi: 10.1089/ten.teb.2008.0687

Berryman, J. G. (1980). Long wavelength propagation in composite elastic media I. Spherical inclusions. *Acoustical Society of America, 68*(6), 11. doi: 10.1121/1.385172

Bian, Z., Wang, R. J., Zhao, D. Q., Pan, M. X., Wang, Z. X., & Wang, W.-H. (2003). Excellent ultrasonic absorption ability of carbon-nanotube-reinforced bulk metallic glass composites. *Applied Physics Letters, 82*(17), 2790-2792. doi: 10.1063/1.1570938

Binder, B. J., Landman, K. A., Simpson, M. J., Mariani, M., & Newgreen, D. F. (2008). Modeling proliferative tissue growth: A general approach and an avian case study. *Physical Review E, 78*(3), 031912. doi: 10.1103/PhysRevE.78.031912

Blom, E. D. (2003). SOme comments on the escalation of tracheoesophageal voice prosthesis dimensions. *Archives of Otolaryngology–Head & Neck Surgery, 129*(4), 500-502. doi: 10.1001/archotol.129.4.500-a

Boccaccini, A. R., Chicatun, F., Cho, J., Bretcanu, O., Roether, J. A., Novak, S., & Chen, Q. Z. (2007). Carbon Nanotube Coatings on Bioglass-Based Tissue Engineering Scaffolds. *Advanced Functional Materials, 17*(15), 2815-2822. doi: 10.1002/adfm.200600887

Boyce, M. C., & Arruda, E. M. (2000). Constitutive models of rubber elasticity: a review. *Rubber chemistry and technology, 73*(3), 504-523. doi: 10.5254/1.3547602

Boyd, J. H., Petrof, B. J., Hamid, Q., Fraser, R., & Kimoff, R. J. (2004). Upper Airway Muscle Inflammation and Denervation Changes in Obstructive Sleep Apnea. *American*

Journal of Respiratory and Critical Care Medicine, 170(5), 541-546. doi: 10.1164/rccm.200308-1100OC

Brown, K. M., & Dennis Jr, J. E. (1971). Derivative free analogues of the Levenberg-Marquardt and Gauss algorithms for nonlinear least squares approximation. *Numerische Mathematik, 18*(4), 289-297. doi: 10.1007/bf01404679

Causin, P., Sacco, R., & Verri, M. (2013). A multiscale approach in the computational modeling of the biophysical environment in artificial cartilage tissue regeneration. *Biomechanics and Modeling in Mechanobiology, 12*(4), 763-780. doi: 10.1007/s10237-012-0440-5

Chao, G., Xiaobo, S., Chenglin, C., Yinsheng, D., Yuepu, P., & Pinghua, L. (2009). A cellular automaton simulation of the degradation of porous polylactide scaffold: I. Effect of porosity. *Materials Science and Engineering: C, 29*(6), 1950-1958. doi: 10.1016/j.msec.2009.03.003

CheapTubes. (2014). Single Walled Nanotubes, from http://www.cheaptubes.com/swnts.htm#single_walled_nanotubes_swnts_90wt%_specifications

Chen, Y., Zhou, S., & Li, Q. (2011). Mathematical modeling of degradation for bulk-erosive polymers: Applications in tissue engineering scaffolds and drug delivery systems. *Acta Biomaterialia, 7*(3), 1140-1149. doi: 10.1016/j.actbio.2010.09.038

Chłopek, J., Czajkowska, B., Szaraniec, B., Frackowiak, E., Szostak, K., & Béguin, F. (2006). In vitro studies of carbon nanotubes biocompatibility. *Carbon, 44*(6), 1106-1111. doi: 10.1016/j.carbon.2005.11.022

Cho, C.-S., Choi, E.-H., Cho, J.-R., & Lim, O. K. (2011). Topology and parameter optimization of a foaming jig reinforcement structure by the response surface method. *Computer-Aided Design, 43*(12), 1707-1716. doi: http://dx.doi.org/10.1016/j.cad.2011.08.008

Chone, C. T., Gripp, F. M., Spina, A. L., & Crespo, A. N. (2005). Primary Versus Secondary Tracheoesophageal Puncture for Speech Rehabilitation in Total Laryngectomy: Long-term Results with Indwelling Voice Prosthesis. *Otolaryngology - Head and Neck Surgery, 133*(1), 89-93. doi: 10.1016/j.otohns.2005.02.014

Chopra, D. P., Kern, R. C., Mathieu, P. A., & Jacobs, J. R. (1992). Successful in vitro growth of human respiratory epithelium on a tracheal prosthesis. *The Laryngoscope, 102*(5), 528-531. doi: 10.1288/00005537-199205000-00011

Chua, M., Chee-Kong, C., Chin-Boon, C., & Lau, D. (2013). Carbon Nanotube-Based Artificial Tracheal Prosthesis: Carbon nanocomposite implants for patient-specific ENT care. *Nanotechnology Magazine, IEEE, 7*(4), 27-31. doi: 10.1109/mnano.2013.2289691

Chua, M., Chui, C. K., Chng, C. B., & Lau, D. (2013, November). Experiments of carbon nanocomposite implants for patient specific ENT care. In*Nano/Molecular Medicine and Engineering (NANOMED), 2013 IEEE 7th International Conference on* (pp. 72-76). IEEE. doi: 10.1109/NANOMED.2013.6766318

Chua, M. C. H., Chui, C. K., Rai, B., & Lau, D. D. P. (2013, July). Development of a patient specific artificial tracheal prosthesis: Design, mechanical behavior analysis and manufacturing. In *Engineering in Medicine and Biology Society (EMBC), 2013 35th Annual International Conference of the IEEE* (pp. 6236-6239). IEEE. doi: 10.1109/EMBC.2013.6610978

Chui, C., Kobayashi, E., Chen, X., Hisada, T., & Sakuma, I. (2004). Combined compression and elongation experiments and non-linear modelling of liver tissue for surgical simulation. *Medical and Biological Engineering and Computing, 42*(6), 787-798. doi: 10.1007/bf02345212

Chui, C., Kobayashi, E., Chen, X., Hisada, T., & Sakuma, I. (2007). Transversely isotropic properties of porcine liver tissue: experiments and constitutive modelling.

Medical & Biological Engineering & Computing, 45(1), 99-106. doi: 10.1007/s11517-006-0137-y

Chung, C. A., Lin, T.-H., Chen, S.-D., & Huang, H.-I. (2010). Hybrid cellular automaton modeling of nutrient modulated cell growth in tissue engineering constructs. *Journal of Theoretical Biology, 262*(2), 267-278. doi: 10.1016/j.jtbi.2009.09.031

Chvapil, M. (1977). Collagen sponge: Theory and practice of medical applications. *Journal of Biomedical Materials Research, 11*(5), 721-741. doi: 10.1002/jbm.820110508

Cotado, F. P., & I., U. d. B. D. d. C. F. (2007). *Effects of Mechanical Stimuli of Vibration and Stretch on Airway Epithelial Cells.* Universitat de Barcelona.

Croll, T. I., Gentz, S., Mueller, K., Davidson, M., O'Connor, A. J., Stevens, G. W., & Cooper-White, J. J. (2005). Modelling oxygen diffusion and cell growth in a porous, vascularising scaffold for soft tissue engineering applications. *Chemical Engineering Science, 60*(17), 4924-4934. doi: 10.1016/j.ces.2005.03.051

Dai, R. L., & Liao, W. H. (2007). Modeling of carbon nanotube composites for vibration damping. 652809-652809. doi: 10.1117/12.716019

Davenport, E. A., & Nettesheim, P. (1996). Regulation of mucociliary differentiation of rat tracheal epithelial cells by type I collagen gel substratum. *American Journal of*

Respiratory Cell and Molecular Biology, 14(1), 19-26. doi: 10.1165/ajrcmb.14.1.8534482

Davenport, E. A., & Nettesheim, P. (1996). Type I Collagen Gel Modulates Extracellular Matrix Synthesis and Deposition by Tracheal Epithelial Cells. *Experimental Cell Research, 223*(1), 155-162. doi: 10.1006/excr.1996.0069

Dean, D., Min, K.-J., & Bond, A. (2003). Computer Aided Design of Large-Format Prefabricated Cranial Plates. *Journal of Craniofacial Surgery, 14*(6), 819-832.

Dewdney, A. K. (2008). Cellular Automata. In J. Editors-in-Chief: Sven Erik & F. Brian (Eds.), *Encyclopedia of Ecology* (pp. 541-550). Oxford: Academic Press.

Dick, C., Georgii, J., Burgkart, R., & Westermann, R. (2008). *Computational Steering for Patient-Specific Implant Planning in Orthopedics.* Paper presented at the VCBM.

Doss, A. E., Dunn, S. S., Kucera, K. A., Clemson, L. A., & Zwischenberger, J. B. (2007). Tracheal Replacements: Part 2. *ASAIO Journal, 53*(5), 631-639 610.1097/MAT.1090b1013e318145ba318113.

Edwards, S. L., Church, J. S., Werkmeister, J. A., & Ramshaw, J. A. M. (2009). Tubular micro-scale multiwalled carbon nanotube-based scaffolds for tissue engineering. *Biomaterials, 30*(9), 1725-1731. doi: 10.1016/j.biomaterials.2008.12.031

Eerenstein, S. J., Grolman, W., & Schouwenburg, P. F. (2002). Downsizing of voice prosthesis diameter in patients with laryngectomy: An in vitro study. *Archives of Otolaryngology–Head & Neck Surgery, 128*(7), 838-841. doi: 10.1001/archotol.128.7.838

Elliott, M. J., De Coppi, P., Speggiorin, S., Roebuck, D., Butler, C. R., Samuel, E., Birchall, M. A. (2013). Stem-cell-based, tissue engineered tracheal replacement in a child: a 2-year follow-up study. *The Lancet, 380*(9846), 994-1000. doi: 10.1016/S0140-6736(12)60737-5

Elving, G. J., van der Mei, H. C., Busscher, H. J., van Weissenbruch, R., & Albers, F. W. J. (2001). Air-flow resistances of silicone rubber voice prostheses after formation of bacterial and fungal biofilms. *Journal of Biomedical Materials Research, 58*(4), 421-426. doi: 10.1002/jbm.1037

Favier, V., Cavaille, J., Canova, G., & Shrivastava, S. (1997). Mechanical percolation in cellulose whisker nanocomposites. *Polymer Engineering & Science, 37*(10), 1732-1739. doi: 10.1002/pen.11821

Finegan, I. C., Tibbetts, G. G., & Gibson, R. F. (2003). Modeling and characterization of damping in carbon nanofiber/polypropylene composites. *Composites Science and Technology, 63*(11), 1629-1635. doi: 10.1016/S0266-3538(03)00054-X

Fishman, J. M., De Coppi, P., Elliott, M. J., Atala, A., Birchall, M. A., & Macchiarini, P. (2011). Airway tissue engineering. *Expert Opinion on Biological Therapy, 11*(12), 1623-1635. doi: 10.1517/14712598.2011.623696

Formica, G., Lacarbonara, W., & Alessi, R. (2010). Vibrations of carbon nanotube-reinforced composites. *Journal of Sound and Vibration, 329*(10), 1875-1889. doi: 10.1016/j.jsv.2009.11.020

Fu, Y. B., Chui, C. K., & Teo, C. L. (2013). Liver tissue characterization from uniaxial stress–strain data using probabilistic and inverse finite element methods. *Journal of the Mechanical Behavior of Biomedical Materials, 20*(0), 105-112. doi: http://dx.doi.org/10.1016/j.jmbbm.2013.01.008

Garijo, N., Manzano, R., Osta, R., & Perez, M. A. (2012). Stochastic cellular automata model of cell migration, proliferation and differentiation: Validation with in vitro cultures of muscle satellite cells. *Journal of Theoretical Biology, 314*(0), 1-9. doi: 10.1016/j.jtbi.2012.08.004

Garzón-Alvarado, D. A., Velasco, M. A., & Narváez-Tovar, C. A. (2012). Modeling porous scaffold microstructure by a reaction–diffusion system and its degradation by hydrolysis. *Computers in Biology and Medicine, 42*(2), 147-155. doi: 10.1016/j.compbiomed.2011.11.002

Gelb, A., & Vander Velde, W. E. (1968). *Multiple-input describing functions and nonlinear system design*: McGraw-Hill.

Genden, E. M., Iskander, A., Bromberg, J. S., & Mayer, L. (2003). The Kinetics and Pattern of Tracheal Allograft Re-Epithelialization. *American Journal of Respiratory Cell and Molecular Biology, 28*(6), 673-681. doi: 10.1165/rcmb.2002-0214OC

Giannatsis, J., & Dedoussis, V. (2009). Additive fabrication technologies applied to medicine and health care: a review. *The International Journal of Advanced Manufacturing Technology, 40*(1-2), 116-127. doi: 10.1007/s00170-007-1308-1

Gibson, R. F., Ayorinde, E. O., & Wen, Y.-F. (2007). Vibrations of carbon nanotubes and their composites: A review. *Composites Science and Technology, 67*(1), 1-28. doi: 10.1016/j.compscitech.2006.03.031

Go, T., Jungebluth, P., Baiguero, S., Asnaghi, A., Martorell, J., Ostertag, H., Macchiarini, P. (2010). Both epithelial cells and mesenchymal stem cell–derived chondrocytes contribute to the survival of tissue-engineered airway transplants in pigs. *The Journal of Thoracic and Cardiovascular Surgery, 139*(2), 437-443. doi: 10.1016/j.jtcvs.2009.10.002

Göpferich, A. (1996). Mechanisms of polymer degradation and erosion. *Biomaterials, 17*(2), 103-114. doi: 10.1016/0142-9612(96)85755-3

Göpferich, A., & Tessmar, J. (2002). Polyanhydride degradation and erosion. *Advanced Drug Delivery Reviews, 54*(7), 911-931. doi: 10.1016/s0169-409x(02)00051-0

Grillo, H. C. (2002). Tracheal replacement: a critical review. *The Annals of Thoracic Surgery, 73*(6), 1995-2004. doi: 10.1016/s0003-4975(02)03564-6

Grolman, W., Eerenstein, S. E. J., Tan, F. M. L., Tange, R. A., & Schouwenburg, P. F. (2007). Aerodynamic and Sound Intensity Measurements in Tracheoesophageal Voice. *ORL, 69*(2), 68-76. doi: 10.1159/000097401

Groover, M., & Zimmers, E. (1983). *CAD/CAM: computer-aided design and manufacturing*: Pearson Education.

Ha-Chul, J., Jin-Hee, M., Dong-Hyun, B., Jae-Hee, L., Yoon-Young, C., Joung-Sook, H., & Sang-Hoon, L. (2012). CNT/PDMS Composite Flexible Dry Electrodesfor Long-Term ECG Monitoring. *Biomedical Engineering, IEEE Transactions on, 59*(5), 1472-1479. doi: 10.1109/tbme.2012.2190288

Halpin, J., & Kardos, J. (1972). Moduli of crystalline polymers employing composite theory. *Journal of Applied Physics, 43*(5), 2235-2241. doi: 10.1063/1.1661482

Harrison, B. S., & Atala, A. (2007). Carbon nanotube applications for tissue engineering. *Biomaterials, 28*(2), 344-353. doi: 10.1016/j.biomaterials.2006.07.044

Harrysson, O., Hosni, Y., & Nayfeh, J. (2007). Custom-designed orthopedic implants evaluated using finite element analysis of patient-specific computed tomography data: femoral-component case study. *BMC Musculoskeletal Disorders, 8*(1), 1-10. doi: 10.1186/1471-2474-8-91

Hastings, W. K. (1970). Monte Carlo sampling methods using Markov chains and their applications. *Biometrika, 57*(1), 97-109. doi: 10.1093/biomet/57.1.97

Heissler, E., Fischer, F. S., Boiouri, S., Lehrnann, T., Mathar, W., Gebhardt, A., Bler, J. (1998). Custom-made cast titanium implants produced with CAD/CAM for the reconstruction of cranium defects. *International Journal of Oral and Maxillofacial Surgery, 27*(5), 334-338. doi: 10.1016/S0901-5027(98)80060-X

Hieu, L. C., Bohez, E., Sloten, J. V., Oris, P., Phien, H. N., Vatcharaporn, E., & Binh, P. H. (2002). Design and manufacturing of cranioplasty implants by 3-axis cnc milling. *Technology and Health Care, 10*(5), 413-423.

Hilgers, F. J. M., Soolsma, J., Ackerstaff, A. H., Balm, F. J. M., Tan, I. B., & van den Brekel, M. W. M. (2008). A Thin Tracheal Silicone Washer to Solve Periprosthetic Leakage in Laryngectomies: Direct Results and Long-Term Clinical Effects. *The Laryngoscope, 118*(4), 640-645. doi: 10.1097/MLG.0b013e31816067d5

Hilgers, F. M., Lorenz, K., Maier, H., Meeuwis, C., Kerrebijn, J. F., Vander Poorten, V. & Brekel, M. M. (2013). Development and (pre-) clinical assessment of a novel surgical tool for primary and secondary tracheoesophageal puncture with immediate voice prosthesis insertion, the Provox Vega Puncture Set. *European Archives of Oto-rhino-laryngology, 270*(1), 255-262. doi: 10.1007/s00405-012-1976-9

Huang, J., Xie, G., & Liu, Z. (2008). FEA of hyperelastic rubber material based on Mooney-Rivlin model and Yeoh model [J]. *China Rubber Industry, 8*, 007.

Huang, Y., & Tangpong, X. W. (2010). A distributed friction model for energy dissipation in carbon nanotube-based composites. *Communications in Nonlinear Science and Numerical Simulation, 15*(12), 4171-4180. doi: 10.1016/j.cnsns.2010.01.017

Hukushima, K., & Nemoto, K. (1996). Exchange Monte Carlo method and application to spin glass simulations. *Journal of the Physical Society of Japan, 65*(6), 1604-1608. doi: 10.1143/JPSJ.65.1604

Ishimaru, A. (1977). Theory and application of wave propagation and scattering in random media. *Proceedings of the IEEE, 65*(7), 1030-1061. doi: 10.1109/proc.1977.10612

Jin, H., & Hanson, G. W. (2006). Infrared and Optical Properties of Carbon Nanotube Dipole Antennas. *Nanotechnology, IEEE Transactions on, 5*(6), 766-775. doi: 10.1109/tnano.2006.883475

Jun, Y., & Choi, K. (2010). Design of patient-specific hip implants based on the 3D geometry of the human femur. *Advances in Engineering Software, 41*(4), 537-547. doi: 10.1016/j.advengsoft.2009.10.016

Jungebluth, P., Alici, E., Baiguera, S., Le Blanc, K., Blomberg, P., Bozóky, B. & Macchiarini, P. (2011). Tracheobronchial transplantation with a stem-cell-seeded bioartificial nanocomposite: a proof-of-concept study. *The Lancet, 378*(9808), 1997-2004. doi: 10.1016/S0140-6736(11)61715-7

Jungebluth, P., & Macchiarini, P. (2014). Airway Transplantation. *Thoracic Surgery Clinics, 24*(1), 97-106.

Kalappa, P., Joong-Hee, L., Rashmi, B. J., Venkatesha, T. V., Pai, K. V., & Wang, X. (2008). Effect of Polyaniline Functionalized Carbon Nanotubes Addition on the Positive Temperature Coefficient Behavior of Carbon Black/High-Density Polyethylene Nanocomposites. *Nanotechnology, IEEE Transactions on, 7*(2), 223-228. doi: 10.1109/tnano.2007.914994

Kanagaraj, S., Varanda, F. R., Zhil'tsova, T. V., Oliveira, M. S. A., & Simões, J. A. O. (2007). Mechanical properties of high density polyethylene/carbon nanotube composites. *Composites Science and Technology, 67*(15–16), 3071-3077. doi: 10.1016/j.compscitech.2007.04.024

Kanzaki, M., Yamato, M., Hatakeyama, H., Kohno, C., Yang, J., Umemoto, T., Onuki, T. (2006). Tissue Engineered Epithelial Cell Sheets for the Creation of a Bioartificial Trachea. *TISSUE ENGINEERING, 12*(5), 10. doi: 10.1089/ten.2006.12.1275.

Kawaguchi, S., Nakamura, T., Shimizu, Y., Masuda, T., Takigawa, T., Liu, Y., Matsumoto, K. (2001). Mechanical properties of artificial tracheas composed of a mesh cylinder and a spiral stent. *Biomaterials*, *22*(23), 3085-3090. doi: 10.1016/S0142-9612(01)00056-4

Kayabasi, O., & Ekici, B. (2008). Probabilistic design of a newly designed cemented hip prosthesis using finite element method. *Materials & Design, 29*(5), 963-971. doi: 10.1016/j.matdes.2007.03.024

Khan, S. U., Li, C. Y., Siddiqui, N. A., & Kim, J.-K. (2011). Vibration damping characteristics of carbon fiber-reinforced composites containing multi-walled carbon nanotubes. *Composites Science and Technology*, *71*(12), 1486-1494. doi: 10.1016/j.compscitech.2011.03.022

Khan, S. U., Pothnis, J. R., & Kim, J.-K. (2013). Effects of carbon nanotube alignment on electrical and mechanical properties of epoxy nanocomposites. *Composites Part A: Applied Science and Manufacturing, 49*(0), 26-34. doi: 10.1016/j.compositesa.2013.01.015

Khare, R. & Bose, S. (2005). Carbon Nanotube Based Composites - A Review. *Journal of Minerals and Materials Characterization and Engineering,* 4(1), pp. 31-46. doi: 10.4236/jmmce.2005.41004.

Kinra, V. K., & ker, E. L. (1983). An experimental investigation of pass bands and stop bands in two periodic particulate composites. *International Journal of Solids and Structures, 19*(5), 393-410. doi: 10.1016/0020-7683(83)90051-3

Kireitseu, M., Hui, D., & Tomlinson, G. (2008). Advanced shock-resistant and vibration damping of nanoparticle-reinforced composite material. *Composites Part B: Engineering, 39*(1), 128-138. doi: 10.1016/j.compositesb.2007.03.004

Kress, P., Schäfer, P., Schwerdtfeger, F. P., & Rösler, S. (2014). Are modern voice prostheses better? A lifetime comparison of 749 voice prostheses. *European Archives of Oto-rhino-laryngology, 271*(1), 133-140. doi: 10.1007/s00405-013-2611-0

Krishnan, A., Dujardin, E., Ebbesen, T. W., Yianilos, P. N., & Treacy, M. M. J. (1998). Young's modulus of single-walled nanotubes. *Physical Review B, 58*(20), 14013-14019.

Kucera, K. A., Doss, A. E., Dunn, S. S., Clemson, L. A., & Zwischenberger, J. B. (2007). Tracheal Replacements: Part 1. *ASAIO Journal, 53*(4), 497-505. doi: 410.1097/MAT.1090b1013e3180616b3180615d.

Kwon, J. Y., & Kim, H. D. (2005). Preparation and properties of acid-treated multiwalled carbon nanotube/waterborne polyurethane nanocomposites. *Journal of Applied Polymer Science, 96*(2), 595-604. doi: 10.1002/app.21436

Lau, C., Cooney, M. J., & Atanassov, P. (2008). Conductive Macroporous Composite Chitosan−Carbon Nanotube Scaffolds. *Langmuir, 24*(13), 7004-7010. doi: 10.1021/la8005597

Lau, D. P., Chng, C. B., & Chui, C. K. (2014). New device for single-stage in-office secondary tracheoesophageal puncture: Animal studies. *Head & Neck*, n/a-n/a. doi: 10.1002/hed.23392

Layman, R., Missoum, S., & Geest, J. V. (2010). Simulation and probabilistic failure prediction of grafts for aortic aneurysm. *Engineering Computations, 27*(1), 84-105. doi: 10.1108/02644401011008531

Laz, P., & Browne, M. (2010). A review of probabilistic analysis in orthopaedic biomechanics. *Proceedings of the Institution of Mechanical Engineers, Part H: Journal of Engineering in Medicine, 224*(8), 927-943. doi: 10.1243/09544119JEIM739

Leardi, R. (2009). Experimental design in chemistry: A tutorial. *Analytica chimica acta, 652*(1), 161-172. doi:10.1016/j.aca.2009.06.015

Leder, S. B., Acton, L. M., Kmiecik, J., Ganz, C., & Blom, E. D. (2005). Voice Restoration With the Advantage Tracheoesophageal Voice Prosthesis. *Otolaryngology -- Head and Neck Surgery, 133*(5), 681-684. doi: 10.1016/j.otohns.2005.08.009

Lee, H. H., Sang Shin, U., Lee, J. H., & Kim, H. W. (2011). Biomedical nanocomposites of poly (lactic acid) and calcium phosphate hybridized with modified carbon nanotubes for hard tissue implants. *Journal of Biomedical Materials Research Part B: Applied Biomaterials, 98*(2), 246-254. doi: 10.1002/jbm.b.31846

Leunisse, C., van Weissenbruch, R., Busscher, H. J., van der Mei, H. C., Dijk, F., & Albers, F. W. J. (2001). Biofilm formation and design features of indwelling silicone rubber tracheoesophageal voice prostheses—an electron microscopical study. *Journal of Biomedical Materials Research, 58*(5), 556-563. doi: 10.1002/jbm.1054

Lewin, J. S., Hutcheson, K. A., Barringer, D. A., Croegaert, L. E., Lisec, A., & Chambers, M. S. (2012). Customization of the voice prosthesis to prevent leakage from

the enlarged tracheoesophageal puncture: Results of a prospective trial. *The Laryngoscope, 122*(8), 1767-1772. doi: 10.1002/lary.23368

Li, W. W., Talcott, K. E., Zhai, A. W., Kruger, E. A., & Li, V. W. (2005). The Role of Therapeutic Angiogenesis in Tissue Repair and Regeneration. *Advances in Skin & Wound Care, 18*(9), 491-500.

Lin, R. M., & Lu, C. (2010). Modeling of interfacial friction damping of carbon nanotube-based nanocomposites. *Mechanical Systems and Signal Processing, 24*(8), 2996-3012. doi: 10.1016/j.ymssp.2010.06.003

Liu, Y., Chakrabartty, S., Gkinosatis, D. S., Mohanty, A. K., & Lajnef, N. (2007). *Multi-walled carbon nanotubes/poly (l-lactide) nanocomposite strain sensor for biomechanical implants.* Paper presented at the Biomedical Circuits and Systems Conference, 2007. BIOCAS 2007. IEEE. doi: 10.1109/BIOCAS.2007.4463323

Lundy, D. S., Landera, M. A., Bremekamp, J., & Weed, D. (2012). Longitudinal Tracheoesophageal Puncture Size Stability. *Otolaryngology -- Head and Neck Surgery, 147*(5), 885-888. doi: 10.1177/0194599812449293

Ma, P.-C., Siddiqui, N. A., Marom, G., & Kim, J.-K. (2010). Dispersion and functionalization of carbon nanotubes for polymer-based nanocomposites: a review.

Composites Part A: Applied Science and Manufacturing, 41(10), 1345-1367. doi:10.1016/j.compositesa.2010.07.003

Macchiarini, P., Jungebluth, P., Go, T., Asnaghi, M. A., Rees, L. E., Cogan, T. A., Birchall, M. A. (2008).Clinical transplantation of a tissue-engineered airway. *The Lancet, 372*(9655), 2023-2030. doi: 10.1016/S0140-6736(08)61598-6

Mao, H., Wang, Y., Yuan, W., & Wong, L. B. (2009). Ciliogenesis in cryopreserved mammalian tracheal epithelial cells cultured at the air–liquid interface. *Cryobiology, 59*(3), 250-257. doi: 10.1016/j.cryobiol.2009.07.012

Markus, M., Böhm, D., & Schmick, M. (1999). Simulation of vessel morphogenesis using cellular automata. *Mathematical Biosciences, 156*(1–2), 191-206. doi: 10.1016/s0025-5564(98)10066-4

Mata, A., Fleischman, A., & Roy, S. (2005). Characterization of Polydimethylsiloxane (PDMS) Properties for Biomedical Micro/Nanosystems. *Biomedical Microdevices, 7*(4), 281-293. doi: 10.1007/s10544-005-6070-2

McDonald, J. B., & Xu, Y. J. (1995). A generalization of the beta distribution with applications. *Journal of Econometrics, 66*(1), 133-152. doi: 10.1016/0304-4076(94)01612-4

Mechel, F. P. (2002). *Formulas of Acoustics*: Springer Verlag.

Mobley, J., Mack, R. A., R., G. J., & Raju, M. P. (2009). Determination of power-law attenuation coefficient and dispersion spectra in multi-wall carbon nanotube composites using Kramers–Kronig relations. *Acoustical Society of America, 126*(1), 6. doi: 10.1121/1.3125323

Mooney, E., Dockery, P., Greiser, U., Murphy, M., & Barron, V. (2008). Carbon Nanotubes and Mesenchymal Stem Cells: Biocompatibility, Proliferation and Differentiation. *Nano Letters, 8*(8), 2137-2143. doi: 10.1021/nl073300o

Moré, J. J. (1978). The Levenberg-Marquardt algorithm: implementation and theory *Numerical analysis* (pp. 105-116): Springer.

Mornex, F., Coquard, R., Danhier, S., Maingon, P., El Husseini, G., & Van Houtte, P. (1998). Role of Radiation Therapy in the Treatment of Primary Tracheal Carcinoma. *International journal of radiation oncology, biology, physics, 41*(2), 299-305. doi: 10.1016/S0360-3016(98)00073-X

Mylavarapu, P., & Woldesenbet, E. (2010). A predictive model for ultrasonic attenuation coefficient in particulate composites. *Composites Part B: Engineering, 41*(1), 42-47. doi: 10.1016/j.compositesb.2009.06.007

Nakamura, T., Sato, T., Araki, M., Ichihara, S., Nakada, A., Yoshitani, M., Hayakawa, K. (2009). In situ tissue engineering for tracheal reconstruction using a luminar remodeling type of artificial trachea. *The Journal of Thoracic and Cardiovascular Surgery, 138*(4), 811-819. doi: 10.1016/j.jtcvs.2008.07.072

Neitzert, H. C., Vertuccio, L., & Sorrentino, A. (2011). Epoxy/MWCNT Composite as Temperature Sensor and Electrical Heating Element. *Nanotechnology, IEEE Transactions on, 10*(4), 688-693. doi: 10.1109/tnano.2010.2068307

Ng, A. H. C., Ng, N. S. P., Zhu, G. H., Lim, L. H. Y., & Venkatraman, S. S. (2012). A fully degradable tracheal stent: In vitro and in vivo characterization of material degradation. *Journal of Biomedical Materials Research Part B: Applied Biomaterials*, *100B*(3), 693-699. doi: 10.1002/jbm.b.32501

Ngo, Q., Yamada, T., Suzuki, M., Ominami, Y., Cassell, A. M., Li, J. & Yang, C. Y. (2007). Structural and Electrical Characterization of Carbon Nanofibers for Interconnect Via Applications. *Nanotechnology, IEEE Transactions on, 6*(6), 688-695. doi: 10.1109/tnano.2007.907400

Nomi, M., Miyake, H., Sugita, Y., Fujisawa, M., & Soker, S. (2006). Role of Growth Factors and Endothelial Cells in Therapeutic Angiogenesis and Tissue Engineering. *Current Stem Cell Research & Therapy, 1*(3), 333-343. doi: 10.2174/157488806778226777

O'Dea, R. D., Osborne, J. M., El Haj, A. J., Byrne, H. M., & Waters, S. L. (2012). The interplay between tissue growth and scaffold degradation in engineered tissue constructs. *Journal of Mathematical Biology*, 1-27. doi: 10.1007/s00285-012-0587-9

Pal, S., Haider, H., Laz, P. J., Knight, L. A., & Rullkoetter, P. J. (2008). Probabilistic computational modeling of total knee replacement wear. *Wear, 264*(7), 701-707. doi: 10.1016/j.wear.2007.06.010

Park, J. H., Jung, J. W., Kang, H.-W., Joo, Y. H., Lee, J.-S., & Cho, D.-W. (2012). Development of a 3D bellows tracheal graft: mechanical behavior analysis, fabrication and an in vivo feasibility study. *Biofabrication, 4*(3), 035004. doi:10.1088/1758-5082/4/3/035004

Paulsen, F. P., Steven, P., Tsokos, M., Jungmann, K., Müller, A., Verse, T., & Pirsig, W. (2002). Upper Airway Epithelial Structural Changes in Obstructive Sleep-disordered Breathing. *American Journal of Respiratory and Critical Care Medicine, 166*(4), 501-509. doi: 10.1164/rccm.2109099

Peltola, S. M., Melchels, F. P. W., Grijpma, D. W., & Kellomäki, M. (2008). A review of rapid prototyping techniques for tissue engineering purposes. *Annals of Medicine, 40*(4), 268-280. doi: doi:10.1080/07853890701881788

Pérez del Palomar, A., Trabelsi, O., Mena, A., López-Villalobos, J. L., Ginel, A., & Doblaré, M. (2010). Patient-specific models of human trachea to predict mechanical consequences of endoprosthesis implantation. *Philosophical Transactions of the Royal Society A: Mathematical, Physical and Engineering Sciences, 368*(1921), 2881-2896. doi: 10.1098/rsta.2010.0092

Plaseied, A., & Fatemi, A. (2006). *Mechanical Properties and Deformation Behavior of a Carbon Nanofiber Polymer Composite Material*. Paper presented at the Proceedings of Multifunctional Nanocomposites, Honolulu, Hawaii. doi: 10.1115/MN2006-17043

Pukelsheim, F. (1994). The three sigma rule. *The American Statistician, 48*(2), 88-91. doi: 10.1080/00031305.1994.10476030

Rains, J. K., Bert, J. L., Roberts, C. R., & Pare, P. D. (1992). Mechanical properties of human tracheal cartilage. *Journal of Applied Physiology, 72*(1), 219-225.

Rajoria, H., & Jalili, N. (2005). Passive vibration damping enhancement using carbon nanotube-epoxy reinforced composites. *Composites Science and Technology, 65*(14), 2079-2093. doi: 10.1016/j.compscitech.2005.05.015

Rekow, D. (1987). Computer-aided design and manufacturing in dentistry: a review of the state of the art. *The Journal of prosthetic dentistry, 58*(4), 512-516. doi: 10.1016/0022-3913(87)90285-X

Robert, C. P., & Casella, G. (1999). *Monte Carlo statistical methods*: Springer.

Rostamiyan, Y., Fereidoon, A., Omrani, A., Ganji, D., Kordani, N., & Sharifi, V. (2011). Experimental and Statistical Study of Nonlinear Effect of Carbon Nanotube on Mechanical Properties of Polypropylene Composites. *parameters, 2*, 1.

Sahithi, K., Swetha, M., Ramasamy, K., Srinivasan, N., & Selvamurugan, N. (2010). Polymeric composites containing carbon nanotubes for bone tissue engineering. *International Journal of Biological Macromolecules, 46*(3), 281-283. doi: 10.1016/j.ijbiomac.2010.01.006

Saito, N., Usui, Y., Aoki, K., Narita, N., Shimizu, M., Hara, K. & Endo, M. (2009). Carbon nanotubes: biomaterial applications. [10.1039/B804822N]. *Chemical Society Reviews, 38*(7), 1897-1903. doi: 10.1039/b804822n

Sanz-Herrera, J. A., Doblaré, M., & García-Aznar, J. M. (2010). Scaffold microarchitecture determines internal bone directional growth structure: A numerical study. *Journal of Biomechanics, 43*(13), 2480-2486. doi: 10.1016/j.jbiomech.2010.05.027

Saringer, W., Nöbauer-Huhmann, I., & Knosp, E. (2002). Cranioplasty with Individual Carbon Fibre Reinforced Polymere (CFRP) Medical Grade Implants Based on

CAD/CAM Technique. *Acta Neurochirurgica, 144*(11), 1193-1203. doi: 10.1007/s00701-002-0995-5

Sarma, P. A., Pidaparti, R. M., & Meiss, R. A. (2003). Anisotropic properties of tracheal smooth muscle tissue. *Journal of Biomedical Materials Research Part A, 65A*(1), 1-8. doi: 10.1002/jbm.a.10355

Savvas, D. N., Papadopoulos, V., & Papadrakakis, M. (2012). The effect of interfacial shear strength on damping behavior of carbon nanotube reinforced composites. *International Journal of Solids and Structures, 49*(26), 3823-3837. doi: 10.1016/j.ijsolstr.2012.08.031

Schneider, F., Draheim, J., Kamberger, R., & Wallrabe, U. (2009). Process and material properties of polydimethylsiloxane (PDMS) for Optical MEMS. *Sensors and Actuators A: Physical, 151*(2), 95-99. doi: 10.1016/j.sna.2009.01.026

Sengers, B. G., Taylor, M., Please, C. P., & Oreffo, R. O. C. (2007). Computational modelling of cell spreading and tissue regeneration in porous scaffolds. *Biomaterials, 28*(10), 1926-1940. doi: 10.1016/j.biomaterials.2006.12.008

Sepulveda, A. T., Guzman de Villoria, R., Viana, J. C., Pontes, A. J., Wardle, B. L., & Rocha, L. A. (2013). Full elastic constitutive relation of non-isotropic aligned-

CNT/PDMS flexible nanocomposites. [10.1039/C3NR00753G]. *Nanoscale, 5*(11), 4847-4854. doi: 10.1039/c3nr00753g

Shanmuganathan, K., Capadona, J. R., Rowan, S. J., & Weder, C. (2010). Biomimetic mechanically adaptive nanocomposites. *Progress in Polymer Science, 35*(1–2), 212-222. doi: 10.1016/j.progpolymsci.2009.10.005

Shi, H., Xu, Z., Qin, X., Zhao, X., & Lu, D. (2005). Experimental Study of Replacing Circumferential Tracheal Defects With New Prosthesis. *The Annals of Thoracic Surgery, 79*(2), 672-676. doi: 10.1016/j.athoracsur.2004.01.013

Shi, X., Sitharaman, B., Pham, Q. P., Liang, F., Wu, K., Edward Billups, W. & Mikos, A. G. (2007). Fabrication of porous ultra-short single-walled carbon nanotube nanocomposite scaffolds for bone tissue engineering. *Biomaterials, 28*(28), 4078-4090. doi: 10.1016/j.biomaterials.2007.05.033

Shimko, V. F., & Claycomb, W. C. (2008). Effect of Mechanical Loading on Three-Dimensional Cultures of Embryonic Stem Cell-Derived Cardiomyocytes *Tissue Engineering, 14*(1), 9. doi: 10.1089/ten.a.2007.0092

Sigma-Aldrich. (2014). Properties and Applications of Carbon Nanofibers (CNFs) Synthesized using Vapor-grown Carbon Fiber (VGCF) Manufacturing Technology.

Carbon Nanofibers, from http://www.sigmaaldrich.com/materials-science/nanomaterials/carbon-nanofibers.html

Simakov, S., Kholodov, A., Kholodov, Y., Nadolskiy, A., & Shushlebin, A. (2006). Computational Study of the Vibrating Disturbances to the Lung Function. In C. A. Motasoares, J. A. C. Martins, H. C. Rodrigues, J. C. Ambrósio, C. A. B. Pina, C. M. Motasoares, E. B. R. Pereira & J. Folgado (Eds.), *III European Conference on Computational Mechanics* (pp. 205-205): Springer Netherlands. doi: 10.1007/1-4020-5370-3_205

Srivastava, D., & Wei, C. (2003). Nanomechanics of carbon nanotubes and composites. *American Society of Mechanical Engineers, 56*(2), 16. doi: 10.1115/1.1538625#

Starly, B., Fang, Z., Sun, W., Shokoufandeh, A., & Regli, W. (2005). Three-Dimensional Reconstruction for Medical-CAD Modeling. *Computer-Aided Design and Applications, 2*(1-4), 431-438. doi: 10.1080/16864360.2005.10738392

Starmer, H. M., Agrawal, N., Koch, W., Richmon, J., Webster, K., & Gourin, C. G. (2011). Does Prosthesis Diameter Matter?: The Relationship Between Voice Prosthesis Diameter and Complications. *Otolaryngology -- Head and Neck Surgery, 144*(5), 740-746. doi: 10.1177/0194599810395362

Sun, W., & Lal, P. (2002). Recent development on computer aided tissue engineering — a review. *Computer Methods and Programs in Biomedicine, 67*(2), 85-103. doi: 10.1016/S0169-2607(01)00116-X

Sun, W., Starly, B., Nam, J., & Darling, A. (2005). Bio-CAD modeling and its applications in computer-aided tissue engineering. *Computer-Aided Design, 37*(11), 1097-1114. doi: 10.1016/j.cad.2005.02.002

Swartz, M. A., Tschumperlin, D. J., Kamm, R. D., & Drazen, J. M. (2001). Mechanical stress is communicated between different cell types to elicit matrix remodeling. *Proceedings of the National Academy of Sciences, 98*(11), 6180-6185. doi: 10.1073/pnas.111133298

Tack, J. W., Verkerke, G. J., Houwen, E. B., Mahieu, H. F., & Schutte, H. K. (2006). Development of a Double-Membrane Sound Generator for Application in a Voice-Producing Element for Laryngectomized Patients. *Annals of Biomedical Engineering, 34*(12), 1896-1907. doi: 10.1007/s10439-006-9196-3

Tada, Y., Takezawa, T., Tani, A., Nakamura, T., & Omori, K. (2012). Collagen vitrigel scaffold for regenerative medicine of the trachea: Experimental study and quantitative evaluation. *Acta Oto-laryngologica, 132*(4), 447-452. doi: doi:10.3109/00016489.2012.654851

Tarnow, V. (1998). Fiber movements and sound attenuation in glass wool. *Journal of Acoustical Society of America, 105*(1), 7. doi: 10.1121/1.424581

Thomson, S. L., Tack, J. W., & Verkerke, G. J. (2007). A numerical study of the flow-induced vibration characteristics of a voice-producing element for laryngectomized patients. *Journal of Biomechanics, 40*(16), 3598-3606. doi: 10.1016/j.jbiomech.2007.06.007

Thostenson, E. T., & Chou, T.-W. (2003). On the elastic properties of carbon nanotube-based composites: modelling and characterization. *Journal of Physics D: Applied Physics, 36*(5), 573. doi: 10.1088/0022-3727/36/5/323

Thostenson, E. T., Ren, Z., & Chou, T.-W. (2001). Advances in the science and technology of carbon nanotubes and their composites: a review. *Composites Science and Technology, 61*(13), 1899-1912. doi: 10.1016/S0266-3538(01)00094-X

Trabelsi, O., del Palomar, A. P., López-villalobos, J. L., Ginel, A., & Doblaré, M. (2010). Experimental characterization and constitutive modeling of the mechanical behavior of the human trachea. *Medical Engineering & Physics, 32*(1), 76-82. doi: 10.1016/j.medengphy.2009.10.010

Tran, P. A., Zhang, L., & Webster, T. J. (2009). Carbon nanofibers and carbon nanotubes in regenerative medicine. *Advanced Drug Delivery Reviews, 61*(12), 1097-1114. doi: 10.1016/j.addr.2009.07.010

Treacy, M. M. J., Ebbesen, T. W., & Gibson, J. M. (1996). Exceptionally high Young's modulus observed for individual carbon nanotubes. *Nature, 381*(6584), 678-680. doi: 10.1038/381678a0

Tsukada, H., Matsuda, S., Inoue, H., Ikada, Y., & Osada, H. (2009). Comparison of bioabsorbable materials for use in artificial tracheal grafts. *Interactive CardioVascular and Thoracic Surgery, 8*(2), 225-229. doi: 10.1510/icvts.2008.186528

Tsukada, H., & Osada, H. (2004). Experimental study of a new tracheal prosthesis: Pored Dacron tube. *The Journal of Thoracic and Cardiovascular Surgery, 127*(3), 877-884. doi: 10.1016/S0022-5223(03)01317-5

Van Den Hoogen, F. J. A., Veenstra, A., Verkerke, G. J., Schutte, H. K., & Manni, J. J. (1997). In Vivo Aerodynamic Characteristics of the Nijdam Voice Prosthesis. *Acta Oto-laryngologica, 117*(6), 897-902. doi: 10.3109/00016489709114221

van Lenthe, G. H., Hagenmüller, H., Bohner, M., Hollister, S. J., Meinel, L., & Müller, R. (2007). Nondestructive micro-computed tomography for biological imaging and

quantification of scaffold–bone interaction in vivo. *Biomaterials, 28*(15), 2479-2490. doi: 10.1016/j.biomaterials.2007.01.017

Verdejo, R., Stämpfli, R., Alvarez-Lainez, M., Mourad, S., Rodriguez-Perez, M. A., Brühwiler, P. A., & Shaffer, M. (2009). Enhanced acoustic damping in flexible polyurethane foams filled with carbon nanotubes. *Composites Science and Technology, 69*(10), 1564-1569. doi: 10.1016/j.compscitech.2008.07.003

Wallace, M. J., Charnsangavej, C., Ogawa, K., Carrasco, C. H., Wright, K. C., McKenna, R., Gianturco, C. (1986). Tracheobronchial tree: expandable metallic stents used in experimental and clinical applications. Work in progress. *Radiology, 158*(2), 309-312. doi: doi:10.1148/radiology.158.2.3941857

Wang, W., Deng, T., & ZHAO, S.-g. (2004). Determination for Material Constants of Rubber Mooney-Rivlin Model [J]. *Special Purpose Rubber Products, 4*, 003.

Wei, C., & Srivastava, D. (2004). Nanomechanics of carbon nanofibers: Structural and elastic properties. *Applied Physics Letters, 85*(12), 2208-2210. doi: 10.1063/1.1792797

Williams, J. H., Lee, S. S., Yuce, H., Engineering, M. I. o. T. D. o. M., Center, L. R., Aeronautics, U. S. N. Branch, T. I. (1983). *Ultrasonic Attenuation of a Void-containing Medium for Very Long Wavelengths*: National Aeronautics and Space Administration, Scientific and Technical Information Branch.

Yamashita, M., Kanemaru, S.-i., Hirano, S., Magrufov, A., Tamaki, H., Tamura, Y., . . . Ito, J. (2007). Tracheal Regeneration After Partial Resection: A Tissue Engineering Approach. *The Laryngoscope, 117*(3), 497-502. doi: 10.1097/MLG.0b013e31802e223d

Yang, J.-H., Jun, T.-G., Sung, K., Choi, J. H., Lee, Y. T., & Park, P. W. (2007). Repair of Long-segment Congenital Tracheal Stenosis. *J Korean Med Sci, 22*(3), 491-496. doi: 10.3346/jkms.2007.22.3.491

Yang, T., Chui, C., Yu, R., Qin, J., & Chang, S. Y. (2011). Quasi-linear viscoelastic modeling of arterial wall for surgical simulation. *International Journal of Computer Assisted Radiology and Surgery, 6*(6), 829-838. doi: 10.1007/s11548-011-0560-x

Ying, C. F., & Truell, R. (1956). Scattering of a Plane Longitudinal Wave by a Spherical Obstacle in an Isotropically Elastic Solid. *Journal of Applied Physics, 27*(9), 1086-1097. doi: 10.1063/1.1722545

Zhan, G.-D., Kuntz, J. D., Wan, J., & Mukherjee, A. K. (2003). Single-wall carbon nanotubes as attractive toughening agents in alumina-based nanocomposites. [10.1038/nmat793]. *Nat Mater, 2*(1), 38-42. doi: 10.1038/nmat793

Zhang, L., & Webster, T. J. (2009). Nanotechnology and nanomaterials: promises for improved tissue regeneration. *Nano Today*, *4*(1), 66-80. doi: 10.1016/j.nantod.2008.10.014

Zhengchun, L., Ci, L., Kar, S., Ajayan, P. M., & Jian-Qiang, L. (2009). Fabrication and Electrical Characterization of Densified Carbon Nanotube Micropillars for IC Interconnection. *Nanotechnology, IEEE Transactions on*, *8*(2), 196-203. doi: 10.1109/tnano.2008.2011774

Zhou, J., Khodakov, D. A., Ellis, A. V., & Voelcker, N. H. (2012). Surface modification for PDMS-based microfluidic devices. *ELECTROPHORESIS*, *33*(1), 89-104. doi: 10.1002/elps.201100482

Zhou, X., Shin, E., Wang, K. W., & Bakis, C. E. (2004). Interfacial damping characteristics of carbon nanotube-based composites. *Composites Science and Technology*,*64*(15), 2425-2437. doi: 10.1016/j.compscitech.2004.06.001

Ziegelaar, B. W., Aigner, J., Staudenmaier, R., Lempart, K., Mack, B., Happ, T., Rotter, N. (2002). The characterisation of human respiratory epithelial cells cultured on resorbable scaffolds: first steps towards a tissue engineered tracheal replacement. *Biomaterials*, *23*(6), 1425-1438. doi: 10.1016/S0142-9612(01)00264-2

PUBLICATIONS

Journal Publications

1) **Chua M**, Chui CK, Chng CB, Lau D (2013). Carbon Nanotube-Based Artificial Tracheal Prosthesis: Carbon nanocomposite implants for patient-specific ENT care. *Nanotechnology Magazine, IEEE, 7*(4), 27-31. doi: 10.1109/mnano.2013.2289691
2) **Chua M**, Chui CK, Teo C (2014). Computer Aided Design and Experiment of a Novel Patient Specific Carbon Nanocomposite Voice Prosthesis. *Computer Aided Design*. doi: 10.1016/j.cad.2014.09.002
3) **Chua M**, Chui CK, Teo C, Lau D (2014). Patient Specific Carbon Nanocomposite Tracheal Prosthesis. *International Journal of Artificial Organs*. doi: 10.5301/ijao.5000374
4) **Chua M**, Chui CK (2015). New Attenuation Predictive Model for Carbon Based Nanocomposites. *Transactions in Nanotechnology, IEEE*. doi: 10.1109/TNANO.2015.2396536
5) **Chua M**, Chui CK (2015). Probabilistic Predictive Modeling of Carbon Nanocomposites for the Computer Aided Design of Medical Implants. *Journal of Mechanical Behavior of Biomedical Materials*. doi: 10.1016/j.jmbbm.2015.01.013

Conferences

1) **Chua M**, Chui CK, Chng C B, Lau D (2013, November). Experiments of carbon nanocomposite implants for patient specific ENT care. In *Nano/Molecular*

Medicine and Engineering (NANOMED), 2013 IEEE 7th International Conference on (pp. 72-76). IEEE. doi: 10.1109/NANOMED.2013.6766318

2) **Chua M**, Chui, CK, Rai B, Lau D (2013, July). Development of a patient specific artificial tracheal prosthesis: Design, mechanical behavior analysis and manufacturing. In *Engineering in Medicine and Biology Society (EMBC), 2013 35th Annual International Conference of the IEEE* (pp. 6236-6239). IEEE. doi: 10.1109/EMBC.2013.6610978
3) **Chua M,** Chui CK (2015). Optimization of Patient Specific Design of Medical Implants for Manufacturing. In *College International Pour La Recherche en Productique (CIRP), 13th Global Conference on Sustainable Manufacturing – Decoupling Growth From Resource Use.* (Paper Accepted for Oral Presentation)

Patent Pending

1) Chui CK, **Chua M**, Lau D, Teo C (2014). Methods and Materials for an Artificial Tracheal Prosthesis and/or Voice Prosthesis. PCT/SG2014/000251. Filed on 30 May, 2014.